The Shape Synthesis of Transmitarray Antenna Elements

By

Abdullah Saad A Aljanah

Thesis submitted in partial fulfillment of the requirements for the
Doctorate in Philosophy degree
in Electrical & Computer Engineering

Ottawa-Carleton Institute for Electrical and Computer Engineering
School of Electrical Engineering and Computer Science

Faculty of Engineering
University of Ottawa

Abstract

Shape synthesis (also called topological synthesis or inverse design in other disciplines) has the potential to provide antenna engineers with a useful addition to their design tools. Transmitarray antennas, which consist of a feed antenna plus a printed planar structure that emulates a lens, are able to provide high directivity antenna performance, and have been the subject of sustained research over the past ten years. The transmitarray lens consists of a lattice of cells, with each cell occupied by an element that includes conductors of specific shape. The feed field incident on each element on the input surface side of the transmitarray is transformed by each element into a field of different amplitude and phase on the output surface side of each element, providing some desired aperture distribution on the output surface. In this thesis we develop a technique, and the overall computational tool to implement it, that fundamentally allows the electromagnetics to dictate how the conducting portions of a 3-layer element must be shaped in order to obtain some specific transmission coefficient. Such shape synthesis of the elements offers the possibility of obtaining elements that have properties not obtainable using conventional elements. These techniques were applied to the shape synthesis of dual-band elements (18 GHz and 24 GHz). A transmitarray using these elements was designed and fabricated, its performance measured and compared to simulated results. An in-depth discussion of the outcome experimentally validates the shape synthesis procedure.

Keywords: transmitarray, elements, 3-layer, shape synthesis

Acknowledgements

All praise, first and foremost, be to Allah our God and Lord of all worlds. I would not have succeeded without God's help and success; he has all the praise and glorification.

I feel gratefulness and gratitude to my supervisor, Dr. Derek McNamara, for his unlimited support and patience with his tangible and moral assistance starting by welcoming me into his research group, passing on his knowledge to me, and supporting me in the many revisions of the writing, formulating and preparation of this thesis document. Derek is not only an advisor, but is my teacher and sponsor in learning, analyzing and dealing with engineering issues.

I present and give my achievement to my great family (my parents, my brothers and my sisters) who I belong to, and who wish the best for me all the time. Moreover, I present this achievement to my small family (my wife and my three kids) who have been patient with me and have filled my life with joy and pleasure. Maha, my darling wife, always unconditionally sacrifices so much for me and our children Raneem, Saad and Jumana. May Allah bless you for your endeavors, Maha.

In addition, I express appreciation to my group members and lab-mates in the Antenna Group at the University of Ottawa (CBY 517) for their beneficial discussions, and interactions for which I am grateful. I take this opportunity to recognise our senior group member Dr. Eqab Almajali, who trained me in CEM simulation tools, and especially supported me when it came to 3D full-wave modelling of the transmitarray

I cannot forget my companion and close brother Abdulmajeed, who support me since I came to Canada for my graduate studies, and helped me adjust to living in Ottawa. Nor do I forget 'buddies' Majed Alowidi, Fahad Alzahrani and Abdullah Alodah, who have been willing at all times to help and assist me with everything.

Finally, my great gratitude is acknowledged to the Saudi Arabian Ministry of Education, represented in Canada by the Saudi Cultural Bureau in Ottawa, for the support and guidance provided to me and my family while we have been in Canada.

TABLE OF CONTENTS

CHAPTER 1

Introduction

CHAPTER 2

Review of Essential Background Concepts & Ideas

CHAPTER 3

Development of the Transmitarray Element Shape Synthesis Tool

CHAPTER 4

The Shape Synthesis of Single-Band 3-Layer-Elements with Full Symmetry

CHAPTER 5

The Shape Synthesis of Dual-Band 3-Layer-elements

CHAPTER 6

Experimental Investigation of the Transmitarray Designed Using Shape-Synthesized Dual-Band Elements

LIST OF FIGURES

LIST OF TABLES

Glossary

Beamforming Network (BFN)	Section 1.1
Radiation Efficiency	Section 1.1
Low Directivity Antenna	Section 1.1
Reflectarray Antenna	Section 1.1
Transmitarray Antenna	Section 1.1
Size Synthesis, Excitation Synthesis and Shape Synthesis	Section 1.2
Floquet Modes	Section 2.2
Passive Element Configuration	Section 2.4
Dual Band Transmitarray	Section 2.4
Moment Method (MM)	Section 2.5
RWG Expansion Functions	Section 2.5
Genetic Algorithm	Section 2.6
Frequency Selective Surface (FSS)	Section 2.7

LIST OF GREEK SYMBOLS

λ_0	Free Space Wavelength
Ψ_{offset}	Arbitrary Phase shift
Ψ_{mn}	Required Transmission Phase Shift for the of the mn-th Element
θ_{edge}	Angle between $\overline{r}_{edge}$ and $\overline{r}_{\mathrm{f}}$
θ_{f}^{mn}	Spherical Angle in the Feed's Coordinate System
Λ_{fill}	Starting Shape Factor
Ψ_{Target}	Targeted Phase Shift of an Element
Ψ_{Actual}	Actual Phase Shift of an Element
$\Delta\Psi_{\mathrm{Tol}}$	Absolute Difference Between Targeted Phase Shift and Actual Phase Shift
ε_r	Relative Permittivity Factor
ξ	Ratio of $E_{\mathrm{cr}}^{\mathrm{out}}$ to $E_{\mathrm{co}}^{\mathrm{out}}$

LIST OF LATIN SYMBOLS

$\overline{R}_{mn}$	Vector from the Feed Phase Center the mn-th Element
k_0	Free Space Phase Constant
$\overline{r}_{mn}$	Location of the mn-th Element in the Lens Surface
$\overline{r}_{\mathrm{f}}$	Position Vector of the Feed
F	Focal Length
$\overline{r}_{edge}$	Vector from the Feed Phase Center to the mn-th Element
D	Circular Transmitarray Diameter
T_{mn}	Transmission Coefficient of the mn-th Element
qf	Feed Pattern Power Factor
qe	Element Pattern Power Factor

dx	Lattice Cell Size in x-Axis
dy	Lattice Cell Size in y-Axis
$d1$	Thickness of the First Spacer
$d2$	Thickness of the Second Spacer
fa	Lower Frequency
fb	Upper Frequency
N_{Δ}	Number of Conductor Triangles in the Mesh
N_{bit}	Number of Binary Bits in the Chromosome
Ne	Number of Required Shaped Elements
$E_{\text{co}}^{\text{in}}$	Incident Co-Polarized Electric field
$E_{\text{co}}^{\text{out}}$	Output Co-Polarized Electric field
$E_{\text{cr}}^{\text{out}}$	Output Cross-Polarized Electric field
S_{21}^{Target}	Targeted |S21| of an Element
S_{21}^{Actual}	Actual S21 Phase Shift of an Element
B_{min}	Minimum Magnitude of S_{21}^{Actual}
F_{obj}	Objective function of The Genetic algorithm
N_{P}	Population Size
B_i	Shunt Susceptance of the i-th layer
$\{\mathcal{U}_e(f_a), \mathcal{U}_e(f_b)\}$	Paired Sets of Transmission Phases required by the e-th Element

CHAPTER 1

Introduction

1.1 ANTENNAS & ANTENNA SHAPE SYNTHESIS

Antennas are needed in any form of wireless communications. One of the pioneers of antenna theory and design wrote [SCHE 52] that the "classification of antennas into mutually exclusive types is impossible, for we can look at the same antenna from different points of view". Indeed, just when you think you have come up with the "best classification" someone is able to point out some flaw. In the end one has to accept the fact that antennas can be grouped in several different ways, by application, by fabrication/construction method, by geometry/structure, by electrical size, by operating principle, by some specific performance measure, and many more. For the purposes of this thesis we will classify antennas according to whether they have low, medium or high directivity. Wireless communications antennas located on mobile devices must have broad radiation patterns and hence low-directivity. They can in principle then be variants of monopole or dipole antennas, microstrip patch radiators, slots and dielectric resonator antennas [VOLA 07], [BALA 08]. In some cases, as for antennas used on wireless basestations (of wireless network cells of different size), the directivity of single radiators such as those just mentioned is not sufficiently high, since radiation patterns with narrower main lobes are needed. In order to realise such high directivity antennas there are two routes that are followed. In one an appropriately shaped reflector (or reflectarray), or some lens arrangement (or transmitarray) is used, fed by one of the above-mentioned low-directivity radiators. Alternatively, several such low-directivity radiators are located in a linear or planar arrangement in space to form an array antenna. Finally, medium directivity[1]antennas are typically horn antennas, which are widely used as feeds for reflector antennas and as antenna measurement standards. A planar array of low-directivity radiators, each excited with the appropriate phase and amplitude using some power-splitting network, normally called the beamforming network (BFN), can provide a pencil beam of high directivity that increases as the number of array radiating elements increases. The BFN network in essence consists of transmission lines that fan out from the

---

[1] Precise numerical values for the ranges of directivities are not stated in any accepted standards, and would therefore be somewhat arbitrary. At some risk, we would venture low directivity being less than 10dBi, medium directivity between 10dBi and 20dBi, and high directivity being greater than 20 dBi.

antenna port to each of the radiating elements, and the array is said to have a constrained feed. This can be costly unless it is possible to use printed BFNs, and indeed these have been widely used in wireless communications. Unfortunately, above 30 GHz or so [LEVI 89] the losses in such printed BFNs are often too high and the radiation efficiency of the overall array antenna becomes too low for its use to be feasible [MAIL 17]. Alternative printed antennas are then desirable. The properties of a conducting (and hence reflecting) surface of paraboloidal shape are such that, when it is illuminated by a low-directivity antenna the reflected field provides one with an electrically large aperture, roughly within the rim of the reflecting surface, over which field has an almost uniform phase. As a result, such reflector antennas [RAO 13] have been a means of realizing high directivities for almost a century. The desire to fabricate antennas using printing methods resulted in the invention of the reflectarray antenna [HUAN 07][SHAK 13]. This is a flat conducting surface, divided into a lattice of cells, each cell occupied by an element. Each element consists of conducting shapes printed on a dielectric substrate that is backed by a conducting ground plane. The features of the conducting shapes of each element are adjusted so that each reflects the incident field from a (low-directivity) feed with a different phase. These reflection phases can be arranged so that the reflectarray surface emulates a solid (non-flat) paraboloidal reflector. It can equally well be considered a space-fed (as opposed to a constrained feed) planar array[2]. One problem from which both classical reflector antennas and reflectarray antennas suffer is that of blockage of the antenna aperture by the feed. Offset arrangements are possible, but more complicated to fabricate. In addition, offset reflectarrays suffer from beam squint with frequency changes. An alternative to classical reflectors is the classical dielectric lens antenna, consisting of a feed and a refracting surface (the lens proper). It does not suffer from aperture blockage because the feed is behind the aperture. But dielectric lenses are heavy and bulky, and so such antennas have not been widely used. The printed version of the lens antenna is the so-called transmitarray antenna [ABDE 17].

In classical antenna design, intuition based on an understanding of physical electromagnetic behaviour is used to select the class and geometrical shape of an antenna to be used for some application, and then specific features of this geometry are adjusted to achieve some desired antenna performance at specific frequencies. We can refer to this as *size synthesis*. This approach to antenna design has had a long history of success, and has led to antennas of the various kinds mentioned above, that have enabled the astounding developments in terrestrial wireless communications,

---

[2] As was noted, any antenna can be classified in more than one way.

satellite communications, radar, and much more. In addition to size synthesis, e*xcitation synthesis* involves the determination of the complex excitations of an array antenna of known radiating elements required to provide some desired radiation pattern performance, and is more commonly called array pattern synthesis [MAIL 17, Chap.3]. Antenna *shape synthesis*[3], on the other hand, is the process of taking a set of desired performance characteristics and using an effective algorithm to actually determine the geometry of an antenna that provides such a performance. The main concern of this thesis is the shape synthesis of transmitarray antenna elements. In order to describe this more precisely it is necessary to provide a brief description of a transmitarray antenna.

1.2 THE TRANSMITARRAY ANTENNA ELEMENT DESIGN PROBLEM

The design of transmitarray antennas has been addressed not only in many journal papers but also in two recent books [ABDE 17], [DUSS 18]. As indicated in Fig.1.1-1, a transmitarray antenna consists of the transmitarray feed and the transmitarray lens (or surface). The transmitarray lens consists of a lattice of cells, with each cell occupied by an element. The feed field incident on each element on the input surface side of the transmitarray is transformed by each element into a field of different amplitude and phase on the output surface side of each element. The transmission properties required of each element is determined according to the amplitude and phase distribution required for the field over the output surface of the transmitarray. The values of certain controllable parameters (eg. conductor dimensions) of each individual element are selected in order to provide the desired transmission properties at that element's location. In all cases up to the present the selection of the values of the element parameters has been done [ABDE 17] using a pre-determined database of transmission coefficients versus the controllable element parameters.

The listing, in Chapter 2, of pertinent existing element types will reveal that all elements used for transmitarray design up to the present time have had conductor shapes pre-selected (based on sound, and often complex, physical arguments), and appropriate sets of feature dimensions that are varied in value to change the element transmission coefficient values. In other words, *size synthesis of transmitarray elements* has been used. In this thesis we will enlist electromagnetic theory itself to shape synthesize transmitarray elements, with a different shape for each required transmission coefficient, instead of using a pre-selected (but differently sized) conductor shape for all elements in a particular transmitarray antenna. In line with the use of the phrase in other antenna contexts,

---

[3] More will be said about this in Section 2.7.

we will call this the *shape synthesis of transmitarray elements*. In the chapters that follow, we will suggest that such shape synthesis offers the possibility of obtaining elements that have properties not obtainable using conventional elements.

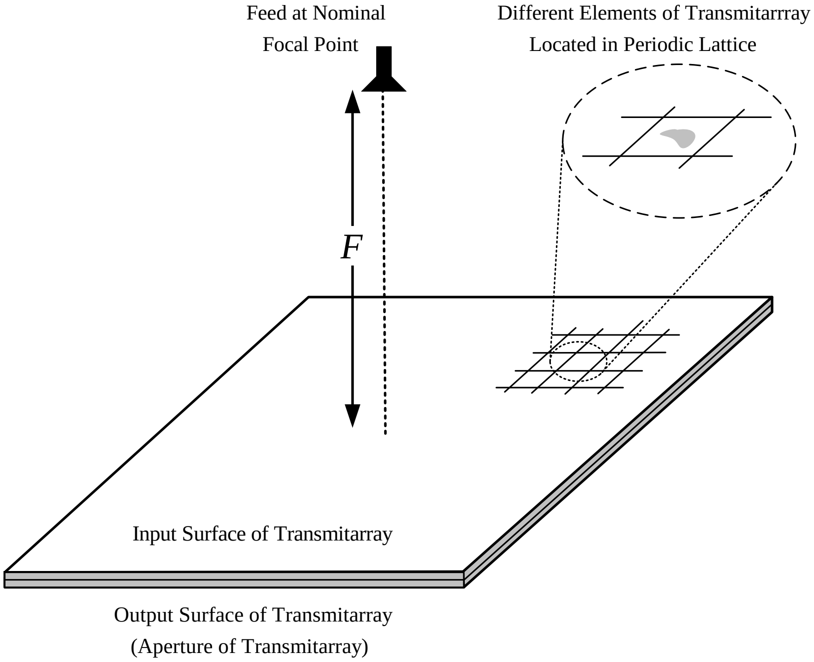

Fig.1.1-1 : Transmitarray antenna configuration.

1.3 OVERVIEW OF THE THESIS AND ITS CONTRIBUTIONS

The research described in this thesis deals with the shape synthesis of multi-layer transmitarray antenna elements. Although the shape synthesis techniques developed here could be used more widely, we will concentrate on 3-layer elements.

Chapter 2 first broadly reviews the subject of transmitarray antennas (which are also referred to as printed lenses, refractarrays or phase shifting surfaces). The descriptions of the topics in the various sections of the chapter are intended merely to provide the background for what is needed in this thesis, and not as a comprehensive introduction to the said topics. Importantly, Section 2.7 provides a look at the progress that has been made in antenna shape synthesis. The principal contributions of the present work are contained in Chapters 3 through 6.

Chapter 3 describes the new shape synthesis tool that has been developed in order to carry out the intended shape synthesis of multi-layer transmitarray elements. Such a tool does not appear to have been available previously, and so is in itself a contribution.

Chapter 4 uses the tool to shape synthesize single-band transmitarray elements covering the entire 360° transmission phase range with a low insertion loss. These shaped elements can do so while maintaining the symmetry needed to “look” the same for either vertical or horizontal polarization (and hence also circular polarization), in other words be polarization insensitive. This has previously not been possible with conventional elements consisting of fewer that four layers.

Chapter 5 uses the new tool to shape synthesize dual-band elements, with widely separated frequencies, that provide different user-specified transmission phase shifts at the two frequencies. The ability to provide transmission phases independently specified for two different frequencies has not yet been achieved by others.

In Chapter 6 the synthesized dual-band elements are used in a specific transmitarray design to experimentally verify the new element shape synthesis procedure that has been devised.

Finally, although the contributions of this thesis are weighed in the concluding sections of each chapter, these are summarized in Chapter 7, and possible future extensions to the present work suggested. It will argue that the work of the thesis contributes to the long-term shape synthesis goals in antenna engineering.

CHAPTER 2

Review of Essential Background Concepts & Ideas

2.1 INTRODUCTION

We are interested in the shape synthesis of transmitarray elements. We wish to place the work of this thesis in context, and hence be able to indicate how it has made a contributions to the field of antenna shape synthesis generally. A review of relevant[4] transmitarray element work and antenna shape synthesis done by others is therefore provided in this chapter. It will also be appropriate to include here certain pieces of technical information that will be needed in later chapters. The sections in the chapters are as follows:

- ■ Section 2.2 –The Constituents of a Transmitarray Antenna
- ■ Section 2.3 – Usual Transmitarray Antenna Design Steps
- ■ Section 2.4 – Existing Transmitarray Element Types
- ■ Section 2.5 – Computation of Individual Element Properties
- ■ Section 2.6 – Optimization Algorithms
- ■ Section 2.7 – Long-Term Shape Synthesis Goals in Engineering
- ■ Section 2.8 – Conclusions

Section 2.2 provides a more detailed view of a transmitarray than that in Section 1.2; this is needed for a proper appreciation of the discussions that follow in later chapters. When discussing the shape synthesis of elements in later chapters, it will often be useful to think in terms of transmitarrays that have their feeds located on-axis. Expressions that will need to be referred to in these later chapters (e.g. to arrive at a typical set of required transmission phases), and are therefore conveniently written down in Section 2.3, will assume such on-axis feeding. However, this does not limit the generality of the element shape synthesis methods developed. A listing of some relevant conventional transmitarray element types is given in Section 2.4, in order that we can easily appreciate the difference between conventional element design and the element shape synthesis done here. During the shaping process the transmission properties of candidate element shapes has to be found repeatedly. The underlying full-wave computational electromagnetics method for doing this is discussed in Section 2.5; this will form one ingredient in the eventual approach used in multi-layer

---

[4] To this thesis.

element shaping. The shaping tool to be developed in the thesis needs to use some optimization algorithm, and so these are briefly put in perspective in Section 2.6. Section 2.7 is important because it places the element shape synthesis of this thesis into the context of what we perceive as the long-term goals of antenna shape synthesis research. Section 2.8 concludes the chapter with a statement on the antenna-related shape synthesis problem that has not been adequately dealt with in the literature, and which forms the subject of this thesis.

2.2 THE CONSTITUENTS OF A TRANSMITARRAY ANTENNA

The essence of the transmitarray antenna is shown in Fig.2.2-1. It is composed of the transmitarray feed plus the transmitarray lens (or surface). Together these make up the transmitarray antenna. The transmitarray lens consists of layers of conducting shapes etched on multiple dielectric substrates separated by dielectric spacers, as illustrated in side view in Fig.2.2-2. The conductor layers are divided into a rectangular lattice of cells, with a conducting shape in each cell. The cell size is kept[5] to less than $\lambda_0 / 2$ to be less susceptable to the incident angle effect [ALMA 11]. We may refer to the first and last layers of the transmitarray lens as the input and the output surfaces, respectively. This assumes we will always consider the transmitarray antenna as if it were being used as a transmitting antenna; reciprocity ensures that there is no loss of generality in doing so. The transmitarray feed (eg. horn or any other appropriate radiator) illuminates the input surface. There is thus an incident field distribution over the input surface that is not uniform in either amplitude or phase. The purpose of the transmitarray structure is to correct this so that the field distribution over the output surface is what we need to provide a particular radiation pattern. The conducting shapes thus vary from cell to cell in order to provide a different transmission coefficient amplitude and phase at each cell to ensure the necessary transformation of the incident field by each cell, so that the field amplitude and phase at the output surface of each cell is what we want it to be.

The output surface (that is, aperture) of a transmitarray antenna is depicted in Fig.2.2-3 for illustration. In practice the aperture would be divided into many more cells. The transmitarray can clearly be thought of as a space-fed planar array of cells, each of size $d_x \times d_y$. The centre of the m-th cell is (x_m, y_m). Each cell acts as a radiating element in the array. If we desire that the antenna have a radiation pattern of some specified shape we can use excitation synthesis to determine what

---

[5] In order to avoid propagating higher-order Floquet modes.

the amplitude and phase must be at each cell, and then determine (using a pre-determined database) the dimensions of the conducting shapes in each cell needed to achieve this for a known feed incident field. The rim of the transmitarray aperture can be of any shape. The case of a circular aperture is illustrated in Fig.2.2-3, the decision on which corner cells to include or exclude from the "parent" rectangular aperture being at the discretion of the transmitarray antenna designer. Such considerations would be little different from those when designing a constrained-fed array with a circular aperture, for example.

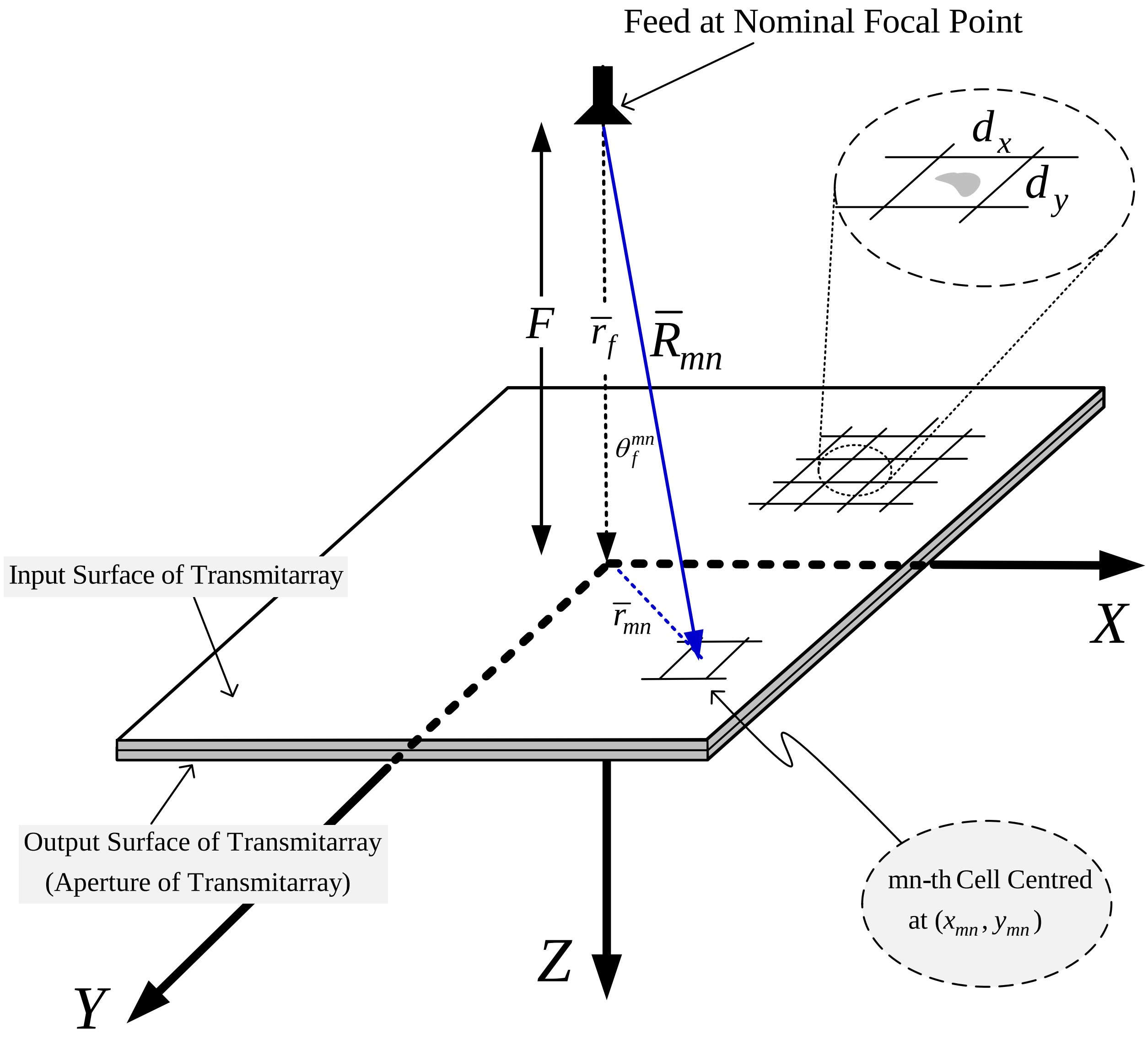

Fig.2.2-1 : Transmitarray configuration.

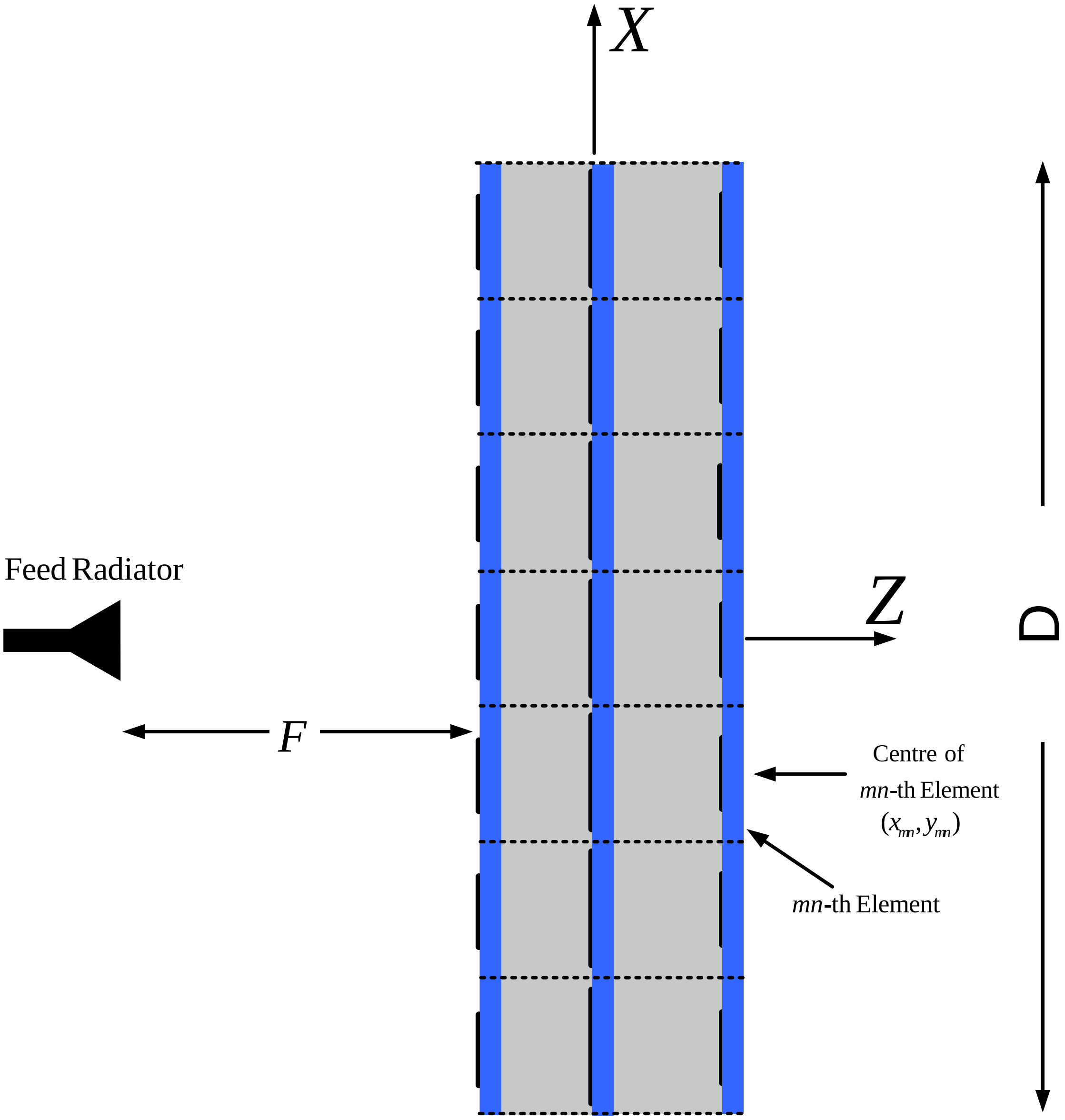

Fig.2.2-2 : Sideview of a typical transmitarray that uses 3-layer elements.

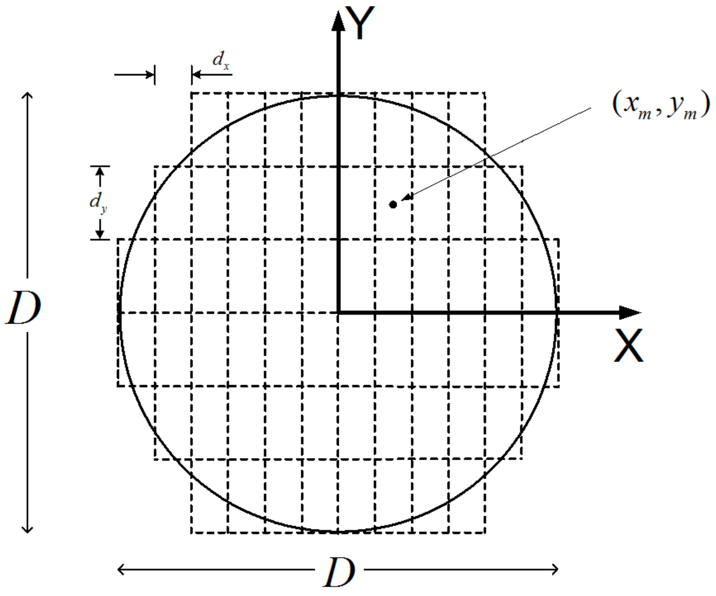

Fig.2.2-3 : Discretized output aperture of the transmitarray antenna.

2.3 USUAL TRANSMITARRAY ANTENNA DESIGN STEPS

A. Broad Steps

In order to determine the transmission coefficient required for each element in the transmitarray some determinations are required:

■ The size and shape of the transmitarray lens aperture has to be chosen, and the location of the feed relative to the transmitarray lens selected (the focal length F of the transmitarray).

■ The lattice size of the transmitarray lens must be chosen, and the aperture shape (eg. circular or rectangular) selected. The number of cells in the transmitarray lens is then known.

■ The phase distribution desired over the output aperture[6] of the transmitarrray lens is then determined, based on the particular final radiation pattern shape needed. In the case of a broadside pencil beams this distribution is uniform.

---

[6] The required output surface phase distribution depends on the particular pattern shape the transmitarray is required to provide. The methods used to determine this are the same as for any planar array antenna [MAIL 17]. Once this is known, the required transmission phases of each of the transmitarray elements can be determined. A recent example is [LORE 18].

■ The different transmission phases required for the elements in each cell must then be calculated, given the known feed field incident on each cell at the input surface of the transmitarray, and the desired phase on the output surface.

■ A set of elements (most often called a database of elements) is required that cover the range of transmission phase values needed. A particular element in the database is selected for each of the cells.

B. Determination of the Required Transmission Coefficient Distribution

The text [ABDE 17] provides a convenient reference for the expressions needed to determine the required transmission coefficient phase of each element. As mentioned in Section 2.1, for present purposes we need only be interested in the case where the feed is on the axis of the transmitarray, as indicated in Figs.2.2-1 and 2.3-1, and the desired pattern is a pencil beam. If one assumes the transmitarray elements are in the far-zone of the feed, then the electromagnetic field incident on each element can be considered to be locally plane, and incident on the particular elements at some angle that can be determined from the transmitarray antenna geometry. The required transmission coefficient phase for the *mn*-th element[7] is [ABDE 17]

$$\Psi_{mn} = k_0 \left\{ \left| \bar{R}_{mn} \right| - \bar{r}_{mn} \cdot \hat{r}_{\mathrm{b}} \right\} + \Psi_{offset} \tag{2.3-1}$$

so that the transmission coefficient can be written $T_{mn} = \left| T_{mn} \right| e^{j\Psi_{mn}}$. Quantity $\bar{r}_{mn}$ is the location of the mn-th element on the transmitarray lens surface, being

$$\bar{r}_{mn} = x_{mn}\hat{x} + y_{mn}\hat{y} \tag{2.3-2}$$

Vector quantity $\bar{R}_{mn}$ is that joining the focal point to the mn-th element, and so for an on-axis feed is

$$\left| \bar{R}_{mn} \right| = \sqrt{x_{mn}^2 + y_{mn}^2 + F^2} \tag{2.3-3}$$

The vector

$$\hat{r}_{\mathrm{b}} = \sin\theta_b \cos\phi_b \hat{x} + \sin\theta_b \sin\phi_b \hat{y} + \cos\theta_b \hat{z} \tag{2.3-4}$$

---

[7] Please see Fig.2.2-1.

is a unit vector in the direction (θ_b, ϕ_b) of the desired pencil beam maximum. The symbol Ψ_{offset} is an arbitrary phase offset, and can be any value by which all the required transmission phases are increased or decreased for a given design[8]. In the case of a pencil beam in the direction broadside to the transmitarray surface we have $(\theta_b, \phi_b) = (0,0)$, so that $\hat{r}_{\mathrm{b}} = \hat{z}$ and $\bar{r}_{mn} \cdot \hat{r}_{\mathrm{b}} = 0$, giving

$$\Psi_{mn} = k_0 \sqrt{x_{mn}^2 + y_{mn}^2 + F^2} + \Psi_{offset} \tag{2.3-5}$$

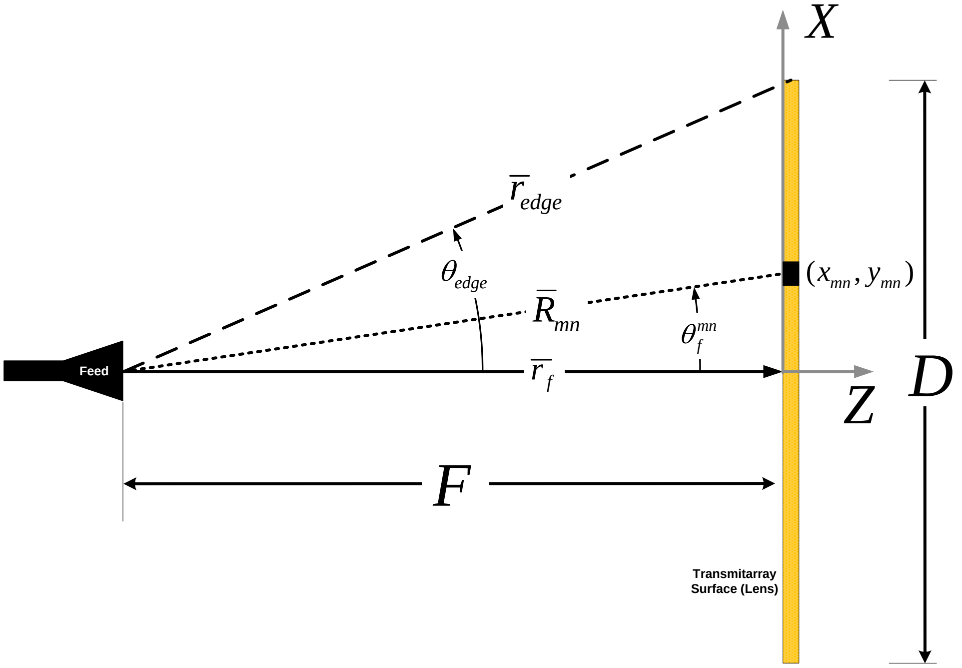

Fig.2.3-1 : Relationship between the feed and the Transmitarray geometry.

Referring to Fig.2.3-1, simple geometry allows us to write

$$\theta_{edge} = \tan^{-1}\left\{\frac{D/2}{F}\right\} = \tan^{-1}\left\{\frac{1}{2(F/D)}\right\} \tag{2.3-6}$$

and

$$\left|\bar{r}_{edge}\right| = \sqrt{(D/2)^2 + F^2} \tag{2.3-7}$$

---

[8] It is only the set of relative phases that matter.

If the feed pattern is represented by the raised cosine form $\cos^{q_\mathrm{f}}(\theta_\mathrm{f}^{mn})$, and the element pattern by $\cos^{q_\mathrm{e}}(\theta)$, then [ABDE 17] the approximate scalar far-zone radiation pattern is[9]

$$F(\theta,\phi)=\sum_{m=1}^{M}\sum_{n=1}^{N}\delta_{mn}\frac{\cos^{q_\mathrm{e}}(\theta)\cos^{q_\mathrm{f}}(\theta_\mathrm{f}^{mn})}{\left|\bar{r}_{mn}-F\,\hat{z}\right|}\left|T_{mn}\right|e^{j\Psi_{mn}}\,e^{-jk\left\{\left|\bar{r}_{mn}-F\hat{z}\right|-x_{mn}\sin\theta\cos\phi-y_{mn}\sin\theta\sin\phi\right\}} \qquad (2.3\text{-}8)$$

This is the pattern of an $M\times N$ element rectangular transmitarray. In order to apply it to one of circular cross-section of diameter D we imagine a parent rectangular transmitarray and simply set $\delta_{mn}=0$ if $\sqrt{x_{mn}^2+y_{mn}^2}>D/2$, the centre of the transmitarray being assumed to be at (0,0).

The complex aperture distribution can be extracted from expression (2.3-8) as

$$a_{mn}=\frac{\cos^{q_\mathrm{f}}(\theta_\mathrm{f}^{mn})}{\left|\bar{r}_{mn}-\bar{r}_\mathrm{f}\right|}\left|T_{mn}\right|e^{j\Psi_{mn}}e^{-jk_o\left|\bar{r}_{mn}-F\hat{z}\right|} \qquad (2.3\text{-}9)$$

and hence the amplitude distribution is

$$\left|a_{mn}\right|=\frac{\left|\cos^{q_\mathrm{f}}(\theta_\mathrm{f}^{mn})\right|}{\left|\bar{r}_{mn}-\bar{r}_\mathrm{f}\right|}\left|T_{mn}\right| \qquad (2.3\text{-}10)$$

Usually we will ideally want $\left|T_{mn}\right|=1$; for practical reasons $\left|T_{mn}\right|\geq -2dB$ is usually accepted. In practice, even if the feed pattern is very broad ($q_\mathrm{f}<1$), the term $\left|\bar{r}_{mn}-\bar{r}_\mathrm{f}\right|^{-1}$ results in what can be called an inherent taper. Expression (2.3-5) will typically demand phase values lying within a full 360° phase range. In practice it can be shown [ABDE 17], at least for pencil beam operation, that some quantization of the output aperture phase distribution can be accommodated, albeit with some loss in aperture efficiency. The resulting transmitarray then requires a discrete set of transmission phases within the 360° phase range, rather than a continuous set. Hence the practice of referring to *n*-bit transmitarrays [ABDE 17]. The approximate radiation pattern prediction model (2.3-8) can be used [ABDE17, pp.13] in obtaining directivity estimates, although these tend to be optimistic.

---

[9] This is an approximate pattern analysis based on treating the transmitarray as a planar array of elements with identical element patterns.

2.4 SOME PERTINENT EXISTING TRANSMITARRAY ELEMENT TYPES

All transmitarray elements reported in the open literature so far have been ones constructed using size synthesis. In order to limit this review to key transmitarray elements which are of the same type as those whose shape synthesis is discussed in this thesis, we consider only passive non-reconfigurable elements that do not require via connections or other circuitry between layers. Table 2.4-1 summarises some transmitarray element types and the reported successful performance of transmitarrays that have used them. These reported designs establish transmitarrays as viable high-directivity antennas.

In comparing the information mentioned in Table 2.4-1, it should be remembered that it is difficult to 'judge' a transmitarray element by observing only its electromagnetic performance over frequency, and care must be taken of the manner an element is "marketed". This is so for a number of reasons, amongst which are:

- One element may be thinner in terms of wavelength than another, and if this is important then the element may appear superior to others.

- One element may have a wider bandwidth than another, but this may be so because it consists of more layers, and so complexity and cost will influence the decision as to which element type to use. Of course, the performance an element type provides depends on how cleverly their potential has been utilized in a given transmitarray design[10]. The eventual bandwidth of the transmitarray (and hence our perception of the bandwidth of the particular element type) depends not only on whether the elements have a "flat" response over frequency. In fact, given the F/D ratio, some prescribed variation of the transmission phase of each element is needed if the phase on the output surface is to be truly uniform. Nevertheless, the use of conventional transmitarray elements has resulted in design successes, such as those summarized in Table 2.4-1.

- One element may be "polarization insensitive", which means it responds in the same way to either of two orthogonal linear polarizations, and hence circular polarization. Another may be polarization sensitive in spite of having fewer layers than another, for example.

One notices in the tabulated references that, in order to improve element performance[11], the element geometries have become increasingly elaborate in shape. For instance, not only the lengths of the arms of a spiral dipole element might be adjusted (as in [ABDE 14]), but the spiral dipole is later made doubly bent and its arm widths different over portions of the element [HSU 18]. Or

---

[10] Once the transmitarray elements are available it does not mean the transmitarray design is done. In this thesis, however, we are primarily interested in the elements themselves.

[11] This has mainly been bandwidth improvements up to now.

different shapes may be used on the element layers (eg. [NEMA 17]). All of this inspired the author of this thesis to wonder whether it would be possible to “let the electromagnetics” tell us what the conductor shapes on the elements layers should be. This is what the thesis explores.

Table 2.4-1 : Summary of Pertinent Transmitarray Element Types.

Reference	Conductor Shape on Element Layers	No. of Layers Used in Reference	Reported Performance of Resulting Reflectarray			
			Max. Aperture Efficiency	**-1dB Bandwidth**	**Aperture Size**	**Additional Comments**
[RYAN 10]	Double Square Loop	4	47%	7.5%	Rectangular $12.6\lambda_o \times 12.6\lambda_o$	Polarization-insensitive
[LIU 15]	Double Split Ring Slot	4	55%	7.4%	Circular Diameter $6.76\lambda_o$	-
[JAZI 16]	Jerusalem Cross	5	34.64 %	10.2%	Rectangular $8\lambda_o \times 8\lambda_o$	Polarization-insensitive
[TIAN 17]	Outer Layers Crossed Slot; Middle Double Square Loop	3	46.5%	16.8%	Circular Diameter $8.8\lambda_o$	Polarization-insensitive
[ABDE 15]	Double Square Loop	4	50% 47%	9.8% 11.7%	Circular Diameter $14.5\lambda_o$	-
[ABDE 14]	Spiral Dipole	3	30%	9%	Circular Diameter $16.2\lambda_o$	-
[RAHM 15]	Square Ring Slots Sandwiching a Coupling Patch	2	38%	5.7%	Rectangular $6\lambda_o \times 6\lambda_o$	-
[NEMA 17] [NEMA 15]	Mixed Shapes (Patch, Square Cross, Meandered Cross)	4	34.9%	18%	Circular Diameter $17.5\lambda_o$	-
[BAGH 17]	Interleaved Loaded Crossed Slot & Loaded Square Loop with Gaps	3	38% [11 GHz] 34.6% [12.5 GHz]	6.8% [11 GHz] 5.4% [12.5 GHz]	Rectangular $7\lambda_o \times 7\lambda_o$ [11 GHz] $8\lambda_o \times 8\lambda_o$ [12.5 GHz]	Dual-Band Dual Linear Polarization & Circular Polarization
[MATO 17]	Loop plus Patch	7	-	-	Rectangular $9.3\lambda_o \times 9.3\lambda_o$ [11 GHz] $13.9\lambda_o \times 13.9\lambda_o$ [12.5 GHz]	Dual-Band
[HSU 18]	Doubly Bent (Spiral) Dipole	4	62%	12.6%	Circular Diameter $8.2\lambda_o$	-
[ERFA 19]	Layered Square Patches Coupled to Two Layered Patches Through Jerusalem Cross Slot	5	32.37%	8.2%	Rectangular $15.6\lambda_o \times 15.6\lambda_o$ [11 GHz]	Polarization-insensitive
[WU 17]	Three Parallel Slots	4	52% [12 GHz] 53% [18 GHz]	-	Rectangular $9.6\lambda_o \times 9.6\lambda_o$ [12 GHz] $14.4\lambda_o \times 14.4\lambda_o$ [18 GHz]	Dual-Band

2.5 COMPUTATION OF INDIVIDUAL ELEMENT PROPERTIES

Although the research in this thesis makes heavy use of computational electromagnetics (CEM) to achieve its goals, it does not do research or development on CEM methods themselves. Instead, it uses the commercially available computational engine FEKO[12]. Nevertheless, some background on the approach used by FEKO is necessary to understand the reason for various decisions taken, and statements made, at various points in the thesis. This section attempts to supply just enough background, and no more. The background material is truly well-known, and adequately described in the textbook literature, amongst which are [PETE 97], [VOLA 12] and [KRIS 16][JOHN 90]. We wish to compute electromagnetic scattering from an infinite planar periodic structure comprised of an infinite number of identical unit cells. Each unit cell consists of vanishingly thin conducting material laid on a dielectric substrate of finite thickness. If the incident field is a plane wave (as is assumed when analysing transmitarray elements) the periodicity of the structure and the characteristics of the incident field allow reduction of the problem to one involving finding the equivalent currents on/in a single unit cell. These are the surface electric conduction currents on the conducting portions of the cell, and equivalent surface electric and magnetic currents that model the substrate material [JAKO 00]. These are the sets of unknowns in the integral equations that constitute a rigorous full-wave electromagnetic model of the unit cell in its infinite periodic environment. These equations are solved numerically using the moment method (MM) for the unknown equivalent currents. A plane wave of specified linear polarization is considered normally incident on the planar periodic structure and constitutes the incident field. The equivalent currents provide the scattered field. These incident and scattered fields are used to determine the complex reflection and transmission coefficients of the incident plane wave, which can be denoted by S_{11} and S_{21} when the wave is incident from side#1 of the structure, and by S_{22} and S_{12} when it is incident from side#2. In other words, a complete 2×2 matrix $[S]$ can be found. These are taken to be the transmission/reflection properties of each element[13]. Such an MM approach can in principle be used to compute the properties of single-layer or multi-layer transmitarray elements with

---

[12] We will in Chapter 3 explain that FEKO on its own does not allow one to perform the shape synthesis of transmitarray elements. It is merely a component of the overall shape synthesis tool whose development is one contribution of this thesis.

[13] In other words, $S_{21} = S_{12}$ (they are equal due to reciprocity) will be conveniently used to refer to the transmission coefficients T_{mn} of elements. Quantities S_{11} and S_{22} then refer to associated reflection coefficients. More will be said about this notation in Section 3.9.

conductors of any shape. We say "in principle" because direct full-wave computation of multi-layer element transmission properties is not feasible when performing shaping, when literally thousands of such simulations are needed. An alternative mixed full-wave/equivalent-circuit approach is proposed in Section 4.2. Also, in the actual transmitarray, an element is not in generally surrounded by other elements identical to it, but we assume the coupling between elements will be much the same.

The MM describes the unknown equivalent current densities in terms of expansion functions. The most widely-used expansion functions[14] are the so-called RWG expansion functions, defined over a triangular mesh. Fig.2.5-1 shows an (albeit simplified) single element layer, in which the element conductor has been meshed into 7 triangles. We note that some triangles have one or more edges in common with an adjacent triangle. There is an RWG expansion function [PETE 97] associated with each such common edge, the latter being shown encircled in red. Current may only flow across such an edge. No expansion functions are associated with unconnected edges of a triangle, and so no current flows across (normal to) such edges. Thus triangle #1 will only have a single RWG function, via its edge that is in common with triangle #2. Triangle #7 has each of its edges in common with another, and so has three RWG functions on it. Triangle #4 has one edge in common with #2, and one with #7, and so has two RWG expansion functions on it. And so on. Although triangles #6 and #8 have a common vertex, with the way RWG expansion functions are defined, there will in the MM formulation (in other words, in the theoretical model) be no current flow through the "vertex-only" connection.

---

[14] The description here is needed to explain some comments made in Section 3.9.5.

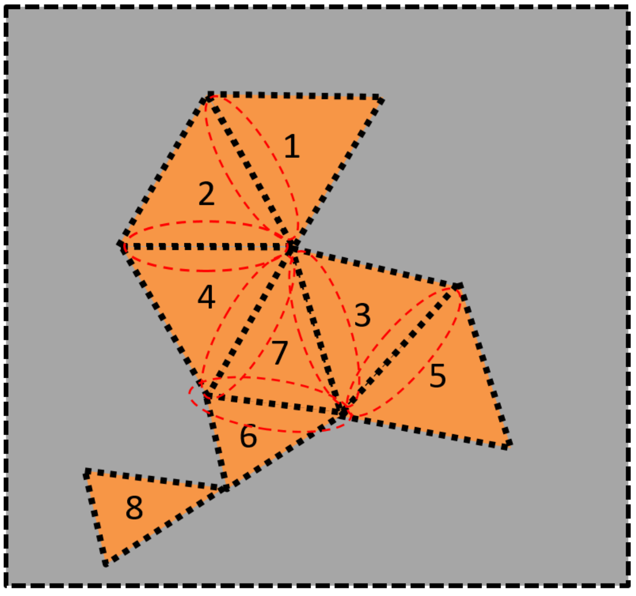

Fig.2.5-1 : Single layer of a transmitarray element (albeit over-simplified) with its conducting portions meshed into triangles. The grey colour is meant to denote the substrate on which the conducting portions are supported; in the CEM analysis its surface will also be meshed but this is not shown.

2.6 OPTIMIZATION ALGORITHMS

In this work we are not making any claim as to having contributed to the details of some new optimization algorithm. The thesis contribution goals have to do solely with the shape synthesis of transmitarray elements, and so we will simply use a particular existing optimization algorithm. It is always good to put one's choices in context though, and so we here very briefly review what optimization algorithms are extant.

Consider a real function $F_{obj}(a_1, a_2, \dots, a_n, \dots, a_N)$ that is dependent on a set of some independent variables $\{a_1, a_2, ..., a_n, ..., a_N\}$, which can be viewed as a point in N-dimensional space. Optimization algorithms are those that attempt to find the value of the N-dimensional point at which F_{obj} is that minimized (or alternatively maximized). There are many different such algorithms, but they can be divided into ones that are gradient based and those that are not.

In elementary calculus one learns how to find the maximum or minimum of a function $F_{obj}(a_1)$ of a single variable a_1 through use of its derivative information. When F_{obj} is a function of many variables the derivative is replaced by the more general gradient concept, and sophisticated ways have been developed of using this to find one's way to the N-dimensional point that minimises F_{obj} . Different gradient-based algorithms steer their route to this point in different ways. If we wish to use such gradient-based algorithms we must of course be able to define and compute the gradients of F_{obj} as the algorithm demands. Tutorial accounts of such algorithms can be found in [BAND 69] and [BAND 88]; these references have not become outdated.

In this thesis we will use one of the so-called evolutionary optimization algorithms, namely the genetic algorithm (GA), that are not gradient based [RAHM 12]. We outline the operation of the GA by describing its essence in connection with the shaping of the conductor in an infinite planar periodic structure. Consider a fictitious cell (eg. one layer of a transmitarray element) in a periodic structure whose planar conducting surface has been divided into a mesh of N_{Δ} triangles[15], as shown in Fig.2.6-1. Each triangle can be filled with conductor, as for all the triangles in Fig.2.6-1(left), or some triangles may be unfilled, as in Fig.2.6-1(right). We can associate a 1 or a 0 with each element, a 1 if it is filled with conductor and a 0 if it is not. In the terminology of the GA, we can define a chromosome that consists of a string of $N_{\text{bit}} = N_{\Delta}$ bits and map each chromosome bit to a different triangle in the meshed geometry. This is illustrated by the binary chromosomes [1 1 1 1 1 1 1] and [0 1 1 1 0 1 1] shown below each of the layouts in Fig.2.6-1. By altering the binary values of each bit a different conducting geometry can be defined. An objective (or fitness) function F_{obj} is defined that is a function of the binary value of each bit constituting the chromosome. Because it is thus a function whose independent variables are the bits in the chromosome, F_{obj} is a function of the shape of the conductor. F_{obj} must somehow translate the desired requirements of the shaping process into a quantitative expression, and so will depend on what it is we actually want to achieve. Computational electromagnetics (CEM) can be used to evaluate the electromagnetic behaviour, and hence an F_{obj}, no matter how it is defined for a specific problem, for each different conductor shape. The binary dependence of the shape makes it tricky to define a gradient even though an appropriate F_{obj} may be "easy" to compute. The fact that GA's do not use gradients of the objective function, has made them suitable in certain antenna shape synthesis problems[16].

---

[15] These need not be triangles. Most authors use rectangles. It will become clear in Chapter 3 why triangles have been used in this thesis.

[16] Albeit not yet done for the shape synthesis of transmitarray elements.

Like all optimization algorithms, the GA needs a starting point. It therefore randomly generates a set of N_P different chromosomes. This is the initial population of conductor shapes, each shape being a member of the population. N_P is called the population size. Once such a population has been created, each member is ranked according to its F_{obj} value. In a structured way, the GA then selects[17] the best members (those with the lowest F_{obj} values) of the population, and discards the others. These "elite" population members are mated[18], and generate offspring that are subsequently integrated into a new population of size N_P. The ranking, selection and mating process is then continually repeated. The goal is that a gradual decrease in the value of F_{obj} will occur as the GA iterates from generation to generation – in other words that the chromosome that gives the minimum F_{obj} will be approached. As expected, the larger the value of N_P the better the chances of F_{obj} actually reaching its physically possible minimum value. If we recall that full-wave CEM analysis is needed each time F_{obj} is evaluated for each population member it is appreciated that there will need to be some trade-off in selecting the value of N_P lest the whole process become inhibitingly computationally time-consuming. It is possible for the GA to stagnate when subsequent generations no longer differ much from previous ones (that is, are not sufficiently 'genetically diverse'). Fortunately, sophisticated mating operations (eg. mutations) have been developed that help prevent this by infusing new genetic material into new generations. Once again, in common with all optimization algorithms, the GA must eventually be halted.

---

[17] Many methods of *selection* have been developed, and are available in the commercial GA software identified in Section 3.4.

[18] Using so-called mating operators that include the operations of crossover, mutation and migration. The relative dominance of the afore-mentioned approaches can also be chosen by the user in the commercial GA software identified in Section 3.4.

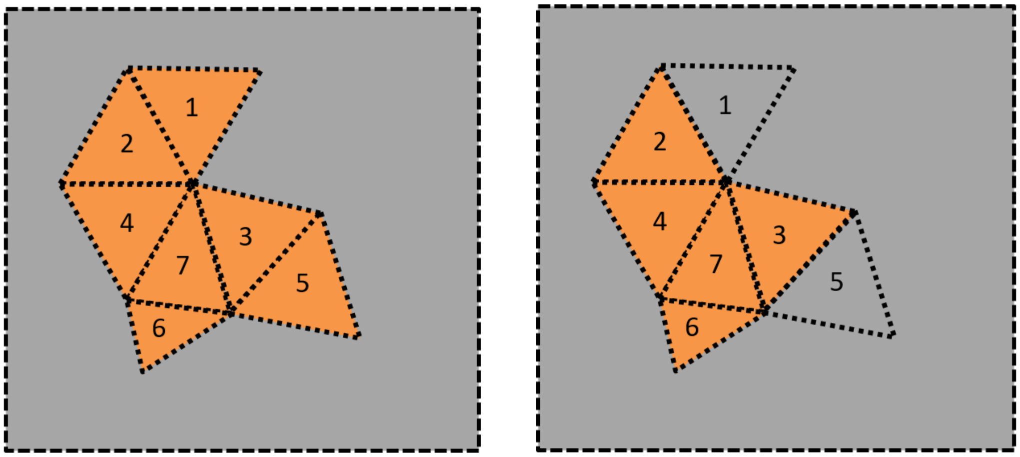

[1 1 1 1 1 1 1]   [0 1 1 1 0 1 1]

Fig.2.6-1 : Single layer transmitarray element (albeit over-simplified) with all its conductor mesh-triangles present (left) and with some of these removed (right), plus the associated chromosome description below each case. The grey colour is meant to denote the substrate on which the conducting portions are supported.

2.7 LONG-TERM SHAPE SYNTHESIS GOALS IN ENGINEERING

We stated in Section 1.1 that by antenna *shape synthesis* we mean the process of taking a set of desired performance characteristics and using an effective algorithm to determine the geometry of the antenna to obtain these characteristics. We contrasted this to the more widely used conventional approach (which we will continue to call *size synthesis*) of selecting the antenna geometry and then adjusting the dimensions of selected geometrical features to obtain some desired performance. In structural engineering, what we will call shape synthesis is usually termed topology optimization/synthesis [ROTZ 14], and seems to have been more widely used in that discipline than antenna engineering. In the photonics area there has recently been increasing interest in shape synthesis approaches, where it is usually referred to as inverse design [MOLE 18]. In the antenna field, shape synthesis research appears to have begun in the mid-1990's. Although it has not been an area in which there has been a copious number of publications, work on antenna shape synthesis has nevertheless been steady.

It is indeed true that the ideal antenna synthesis procedure would allow one to "start with a set of electrical, mechanical, and system specifications that would lead to a particular antenna together with its specific geometry and material specification", but that "this ideal general antenna synthesis method does not exist" [STUT 08]. Current progress on antenna shape synthesis has kept this lofty goal in its long-term vision while tackling less ambitious cases of increasing complexity.

As stated in Section 2.6, in order to use optimization algorithms for the shape synthesis of any antenna (or indeed any device) one must translate the design goals into a quantity that, when minimized, provides an antenna that has the performance we desire. The most straightforward manner to define an objective function in antenna work is to use a combination of the input reflection coefficient, the directivity, radiation efficiency, and so on [STUT 13]. This has been used to shape synthesise low directivity[19] microstrip [JOHN 99a][JOHN 99b][THOR 05], and wire [YAMA 09], antennas, with the conductor layout shaped through the removal or retention of conducting pixels into which the starting shape is divided. This has allowed miniaturization and bandwidth increases of these planar structures. Fully three-dimensional shaping of thin-wire antennas is performed in [ALTS 02][LIND 99][CHOO 05], with some restrictions placed on the allowed occupied volume, for obvious practical reasons. The above references all used the GA as the optimization method. More recently [MIRH 15] used a binary particle swarm optimization algorithm, and [GOUD 17] used binary differential evolution, in such pixelization-based shaping, but for problems already satisfactorily tackled with the GA.

One alternative to the pixelization approach exploits methods used in structural engineering, and is discussed in [HASS 14] and [EREN 11]. It permits extremely fine resolution, as is apparently required in its structural application, and is computationally very intensive. It is not clear whether such resolution is really needed in antenna problems. Another route that does not use pixelization is one using gradient based optimization to shape antennas whose geometry is defined in terms of splines [GRIF 06][TOIV 10][SALU 18]; the spline parameters are adjusted during the optimization process and so shapes the antenna[20]. With the exception of [EREN 11], all the shape synthesis work for conducting surface antennas (as opposed to thin wires) that we have surveyed, such as that reviewed above, has been applied to planar shapes only.

A method for the shape synthesis of single electrically-small antennas, in which the feed location need only be selected after the shaping has been performed, was described in [ETHI 14a]. A related approach was later used in [YANG 19] for MIMO antennas, and has been termed a "shape-first,

---

[19] The shaping of high-directivity reflector antenna surface geometries for directivity maximisation, or to provide contoured beams, has been done for many years [RAO 13, Vol.I] [RAHM 07], and should also be considered to be shape synthesis.

[20] So this might be considered to fall somewhere between size synthesis and shape synthesis.

feed-next" approach by its authors. It relies on a characteristic mode analysis of the structure. This work applies to electrically small or intermediate-size antennas that are "single-mode" in the sense that only one characteristic mode completely describes the antenna's behaviour. If the antenna proper radiates in the presence of other objects (that need not be electrically small) the approach of [ETHI 14a] can still be used [ETHI 12], except that the sub-structure characteristic modes of the antenna proper (with the other objects in place) must be used. The shape-first feed-next approach has more recently been extended to fully 3D conducting surface antennas [ALAK 17][ALAK 18]. The shape synthesis of dielectric resonator antennas has recently been reported [ALRO 20].

Shape synthesis has in fact been done in antenna work related to that of this thesis, namely for the shape synthesis of frequency selective surfaces (FSS)[21] with specific passband or stopband performance in [OHIR 04], and for the shape synthesis of reflectarray elements in [AOKI 11][ETHI 14b]. In the latter reference the elements are shaped in such a way that adjacent reflectarray elements, although not identical, can be selected to have a geometrical similarity that in the end endows the resulting reflectarray with improved aperture efficiency. However, the FSS and reflectarray work just referenced has been done for single-layer elements only. Also, the in-house CEM codes used in the above references have not rigorously accommodated substrate effects, and so the above references have fabricated the elements on very thin substrates that are bonded onto free-space foam. The use of shape synthesis for transmitarray elements has not been reported. Neither has the shape synthesis of elements for multi-layer versions of any of the above devices. We remark that for multilayer work the constraint of having to use very thin substrates would be a limitation. The work in this thesis makes possible the shape synthesis of multi-layer transmitarray elements on substrates of any thickness, by developing[22] a shaping controller that is able to exploit a commercial CEM engine.

A rigorous (albeit over-ambitious and unfeasible) approach to the shape synthesis of a transmitarray antenna would be this : • We specify the element locations, the number of layers in each element, and the thickness of the spacers. • We populate the surface of each element layer with conductor. • We then define an objective function whose minimization would ensure the required

---

[21] A periodic structure of identical elements. This is unlike reflectarrays and transmitarrays that do not have all elements identical, but whose individual element properties are found on a per element basis by assuming each element lies in a periodic structure of identical elements, as noted in Section 2.5 for transmitarray elements. Regular element shapes that have arisen in FSS work have been selected by some authors for use in transmitarrays; but these have not been ones that have been shape synthesized.

[22] In Chapter 3.

transmitarray performance is achieved. • We then use some algorithm to alter the conductor shape on each element layer for each element simultaneously.

Although such an approach might be possible in the far long-term, it will not be so in the short-term. We therefore set our sights on something currently achievable, and that will be applicable to progressively more complex requirements as computational power continues to improve. In spite of the impressive successes achieved by others in transmitarray element selection, and transmitarray design, we foresee future situations where we do not necessarily wish to improve what is possible with existing element designs, but wish to achieve similar performance with less complexity (eg. fewer layers), or achieve some non-standard performance otherwise not available. The need for such trade-offs have been noted by several authors (eg. [JAZI 16]). In order to explain what we mean we will list, for illustration, a few possible scenarios[23] that could be forthcoming:

- A dual-band transmitarray is needed, with one set of prescribed phases for each element at one frequency (say f_a) and another set of prescribed phases at a separated frequency (f_b) for the same elements[24].

- A pencil beam transmitarray is required with a quantised output surface phase distribution, and elements utilising the smallest number of layers to give a specific narrow bandwidth.

- A transmitarray is required, but only for a narrowband application, must also act as a linear-to-circular polarizer, but must use the lowest number of layers possible.

- A transmitarray is required, but only for a narrowband application, must also act as a polarization rotator, but must use the lowest number of layers possible.

- A transmitarray is required, but only for an application with a moderate bandwidth, but the elements must have a specific variation over frequency so as to compensate for the varying phase pattern of the feed, in order to be able to use the smallest number of elements.

The central theme here is to let the electromagnetics “tell us” what the element shapes need to be to obtain some desired performance, and hence achieve the flexibility referred to above to achieve more elaborate goals than might be possible with conventional elements.

---

[23] One never knows ahead of time precisely what sort of requirements and scenarios might arise out of future systems, and so a flexible ability to perform the shape synthesis of transmitarray elements can be argued as being desirable.

[24] For instance a pencil beam (and hence one set of transmission phases) may be required at one frequency, but a shaped beam (and hence a different set of prescribed transmission phases [CRUZ 18]) at the other frequency. Or pencil beams could be desired, but with offset focal points to accommodate separate feeds at the two frequencies.

2.8 CONCLUDING REMARKS

We began this chapter by affirming the interest in this thesis work to be that of shape synthesizing transmitarray elements. Section 2.2 described the constituents of a transmitarray antenna. The steps in the usual transmitarray design process were outlined in Section 2.3, and expressions given for determining what the transmission phase must be for each element in an on-axis fed the transmitarray with a pencil beam radiation pattern. Some existing pertinent transmitarray element types were listed in Section 2.4. The computation of the properties of individual elements, and the assumption of their being located in an infinite periodic structure when doing so, was discussed in Section 2.5. This will allow us to more easily identify how element performance prediction is done in the shape synthesis procedures discussed in the thesis from Chapter 3 onwards. Although optimization algorithms are taken as a given in this thesis, it was worthwhile to summarize in broad terms, in Section 2.6, the way the genetic algorithm will be used in this work. Section 2.7 attempted to show that there has been (perhaps slow) but steady progress in the development of shape synthesis methods in antenna engineering.

One conclusion that can be drawn from Section 2.4 and Section 2.7 is that no shape synthesis procedures for multi-layer transmitarray elements have been reported by others. This will be done here for the first time, in Chapters 4 and 5. Chapter 3, which follows next, develops the new computational tool needed to achieve this. Chapter 6 discusses a transmitarray that was designed to utilize shape-synthesized elements, and then fabricated, to act as a testbed to evaluate the soundness of the shaping procedure developed. Overall conclusions, the contributions of the thesis, and suggestions for possible future work, are the subject of Chapter 7.

CHAPTER 3

Development of the Transmitarray Element Shape Synthesis Tool

3.1 PRELIMINARY REMARKS

In this chapter we describe a computational tool for the shape synthesis of multi-layer transmitarray elements; as far as we are aware this is the first time such a tool has become available. Section 3.2 introduces some terminology needed to ensure there is no ambiguity in the description of the shaping tool. Section 3.3 gives an outline of the full-wave electromagnetic analysis engine that will be used to model element layers[25]; this will include comments on the accuracy of the analysis intended to establish confidence in the modelling. This thesis will use an existing optimization algorithm in the development of the new transmitarray element shape synthesis tool; this is identified in Section 3.4. The machinery of the shape synthesis tool that has been developed in this work is the subject of Sections 3.5, 3.6, 3.7 and 3.8. Section 3.9 will apply the tool to the shape synthesis of 1-layer elements (that is, elements that consist of a single layer). Although such 1-layer elements are usually not sufficient for transmitarray design[26], they have served as a useful vehicle for performing "exercise runs" of the shaping tool and then using this experience to make improvements to the tool. The chapter is concluded in Section 3.7.

3.2 SOME TERMINOLOGY

Some terms need to be defined to facilitate the unambiguous description of the procedure described in this chapter. As stated in Section 1.2 and in greater detail in Section 2.2, a transmitarray antenna consists of a feed radiator and the transmitarray lens. The transmitarray is divided into a lattice of cells, with each cell occupied by an *element*. Typically, an element is comprised of several layers with foam spacers of selected thicknesses separating them; we will refer to N-layer-elements. A layer consists of a selected conducting shape etched onto a thin dielectric substrate. By

---

[25] Precisely what is meant by an element layer will be clear from Section 3.2. The 3-layer elements are modelled using element layers and spacers that are cascaded, and whose combined responses are computed using analytical microwave network analysis methods. We will use the terms "layer" and "element layer" interchangeably.

[26] Although, as conjectured in Section 2.7, situations could arise where this might be sufficient.

sandwiching these layers and spacers we obtain the complete transmitarray N-layer element. This is shown in Fig.3.2-1 as a repetition of Fig.2.2-2 with some extra detail.

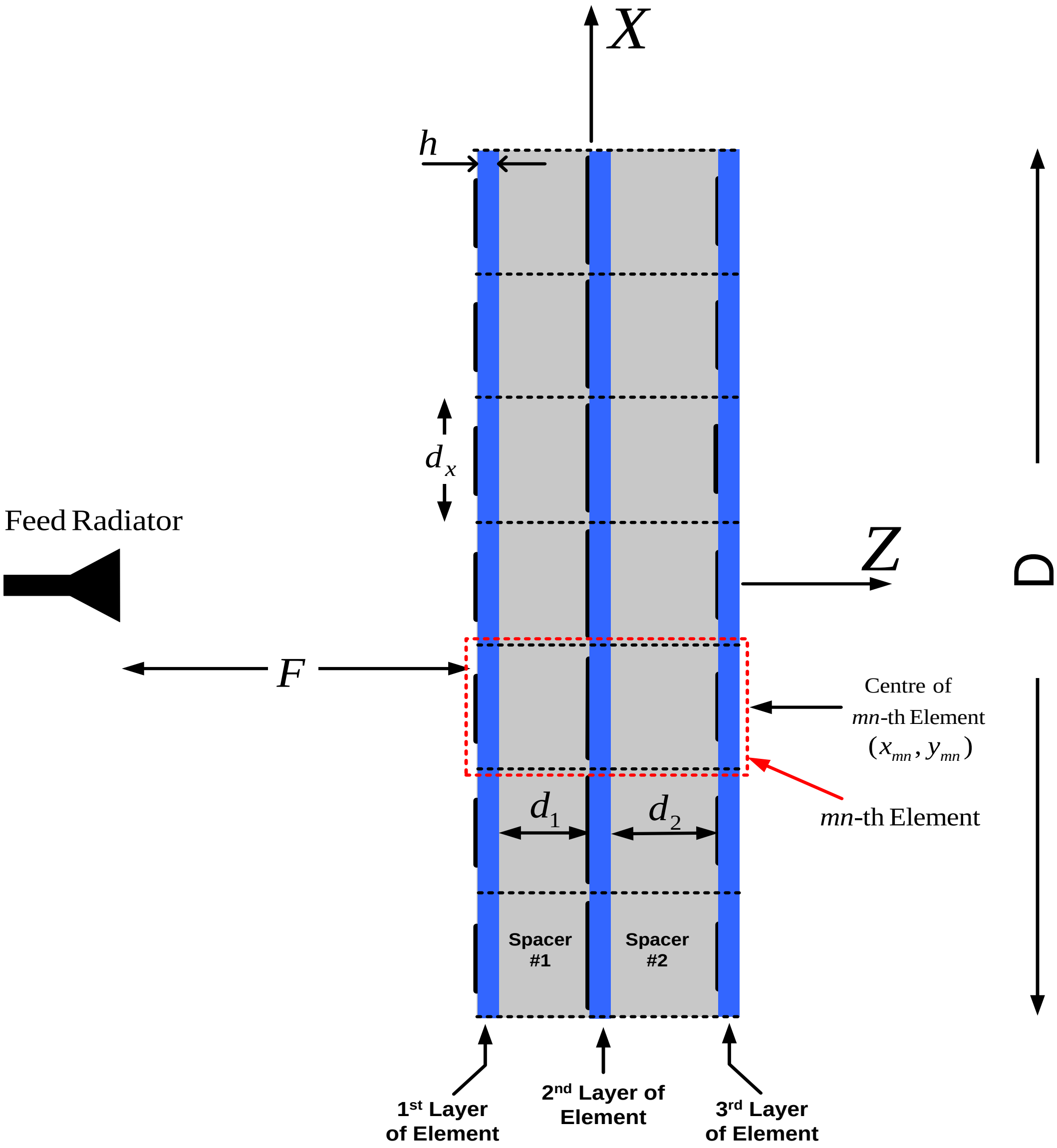

Fig.3.2-1 : Illustration of the geometry of a transmitarray of 3-layer elements.

3.3 IMPLEMENTATION ISSUES : FULL-WAVE ELECTROMAGNETIC SOLVER

3.3.1 Selection of Computational Electromagnetics (CEM) Engine

We have used the code [FEKO] for the full-wave electromagnetic simulation of the *infinite periodic structure* of element layers[27]. The advantage of being able to use a commercial code is that the approach becomes more accessible to others, and one can benefit from on-going upgrades to such codes[28]. FEKO in particular allows the user access to resource files from which complete geometrical details of the triangular pixels can be extracted, and much more[29]. We have implemented the procedure by developing a shape optimization supervision code (that will be referred to as the shaping controller) in MATLAB that is able to communicate with, and interpret, FEKO resource files, as well as run the GA (also available commercially as part of the MATLAB optimization toolbox). The developed shaping controller incorporates a geometry controller to dictate what pixel changes are permitted and what symmetries are to be enforced during shaping. Whenever the GA has, during its many iterations, altered the geometry, the shaping controller makes it possible to send this information back to FEKO as a geometry file, have it generate a new MM-matrix, and perform a full-wave analysis from which the fitness functions (objective functions), that allow the GA to take its next decision, are evaluated. The shaping controller permits the description of fitness functions that are more than merely simple mathematical functions, but ones that inherently contain searching and decision making in their definitions as well; this will be described in later sections.

3.3.2 Confidence in Full-Wave Results

Many authors have correctly warned that inaccurate results, albeit rapidly computed, are of little use. In all the results to be presented in this thesis the MM mesh densities on the conducting portions of element layers, and the dielectric substrate of these layers, is such that a converged result is obtained. This is checked on a problem-by-problem basis, as will be described in Section 3.9.

---

[27] Recall that by “layer” we mean a conducting shape on a substrate.

[28] For instance, between the time this work began, and the time of the writing of the present document, the execution time of a single full-wave analysis run at single frequency has decreased significantly.

[29] This is not the case with other commercial CEM codes we have investigated. They can therefore not be used for the shape synthesis developed here.

To get accurate results the triangular mesh dimensions on the conductor metal face and the dielectric substrate upper and lower surfaces[30] must be very small with respect to the wavelength at the highest frequency of interest. The meshing required is checked for convergence using a set of test runs. This being understood, no further comment is necessary. There should be no overkill in the mesh density, since it must be remembered that full-wave simulations might be performed hundreds of times to shape synthesize a single N-layer transmitarray element. Accurate results that take ridiculously long to run are of little use for present purposes. What is needed are results of sufficient accuracy that run in a reasonable time (or even just slightly longer than a reasonable time!).

3.3.3 Computational Model of a 3-Layer Element

It is in principle possible to compute the transmission properties of a 3-layer element using a full-wave analysis (of the complete layered structure) via the method outlined in Section 2.5, and this has indeed been done by the present author. However, such an approach is not feasible[31] when performing a shape synthesis, when an enormous number of such analyses would be required during the shaping of each element. As already stated in a footnote, an alternative mixed approach is required, as will be discussed in Section 4.2.

3.4 IMPLEMENTATION ISSUES : OPTIMIZATION ALGORITHM

There are many in-house genetic algorithms for optimization. As with the CEM engine selected, and for similar reasons, the approach here has been to select GAs already implemented in commercially available software. The particular “make” of GA we have selected is that available in the MATLAB optimization toolbox. As for the case of our use of the commercially available CEM engine, utilization of the commercially available GA algorithm has allowed the development of a shape synthesis tool that can be accessible to others. It can benefit from the superior numerical/arithmetic practices used in such software, as well as future upgrades.

---

[30] As hinted in Section 3.1, and to be elaborated on in Sections 4.2, only individual element layers undergo full-wave modelling. The response of the N-layer element is obtained using these full-wave results with microwave network analysis to obtain the overall response of an N-layer element.

[31] It is feasible when requiring the performance of a single layer of such a 3-layer element.

The development of optimization algorithms is not considered a contribution of this thesis. The GA and CEM engine are used as building blocks in the actual contribution, namely the development of procedures, and a tool that implements them, for the shape synthesis of transmitarray elements.

Exactly how well a GA performs is application-specific. In the present case the degree of success depends on the settings of the various parameters already mentioned in relation to the GA in Section 2.6. The GA in MATLAB allows one to experiment with these settings, which are tabulated in Appendix A.

3.5 IMPLEMENTATION ISSUES : THE SHAPING CONTROLLER

The shaping controller has been developed in a MATLAB environment. As its name suggests, its task is to link, transfer data between (with many back-and-forth format changes), and pilot the entire shaping process shape synthesis process. It can be described in terms of five essential parts:

- Optimization Algorithm (GA-Algorithm)
- Computational Electromagnetics (CEM) Engine
- Geometry Controller
- Objective Function Construction
- Shaping Process

We have already discussed the first two bullets in Sections 3.3 and 3.4, respectively. The remainder are outlined in what follows.

3.6 GEOMETRY CONTROLLER

3.6.1 Initialization

At the very start of the shaping process the geometry controller is used to:

▲ Define the element cell size (the lattice dimensions of the periodic structure).

▲ Define the starting shape of the conductor.

▲ Specify the relative permittivity and thickness of the substrate.

▲ Specify the polarization of the incoming wave.

▲ Specify what output is desired from the full-wave analysis (usually the two-port scattering parameters that represent the transmission and reflection coefficients of the element unit cell).

▲ Specify the frequency.

▲ Inject a customized mesh[32] into FEKO.

The geometry controller script affords many options. It removes or replaces conducting pixels according to commands coming from the GA, for each population member (that is, specific conductor geometry) in each generation. It does this by interpreting resource files made accessible by FEKO[33], making the changes, and then returning the altered geometry file[34] back to FEKO for the full-wave analyses of the next shaping iteration, in a format that FEKO can interpret. There are equivalent current densities on both the conducting portions of the element and the top/bottom surfaces of the substrate; in all cases only those currents (and hence triangles) associated with the conductors are used in the shaping process. The FEKO geometry file fortunately separates the triangles associated with the conducting portions of the unit cell from those that mesh the dielectric substrate. The first portion of this file is continually automatically altered by the shaping controller whereas the latter is unaltered because the substrate is not being shaped.

3.6.2 Starting Shape

Possible element starting shapes are shown in Fig.3.6-1. We would want to have as much starting conductor present as possible, because this gives the shaping tool more to work with. However, if the starting conductor shape fills the complete unit cell, as in Fig.3.6-1(a), then the shaping process can produce element shapes where there needs to be some conducting contact between adjacent elements. An example is shown in Fig.3.6-2. This might be useful for synthesizing devices in which all elements in any layer are identical, such as circular polarizers and frequency selective surfaces. However, the elements on any layer of a transmitarray, although placed in a periodic lattice, are not in general identical[35]. In order to prevent such elements arising in the shape synthesis process we therefore define a filling factor

---

[32] See Section 3.6.4.

[33] But which most regular users of FEKO would not have to bother with.

[34] Called the **.cfm* file by FEKO.

[35] Although some elements may re-occur.

$$\Lambda_{\mathrm{fill}} = \sqrt{\frac{\text{Area of Starting Shape}}{\text{Area of Unit Cell}}} \tag{3.6-1}$$

If the starting shape has $\Lambda_{\mathrm{fill}} < 1$, as illustrated in Fig.3.6-1 (b) and (c), the resulting shaped elements are prevented from having such conducting contact with adjacent elements. Such an example is that in Fig.3.6-3.

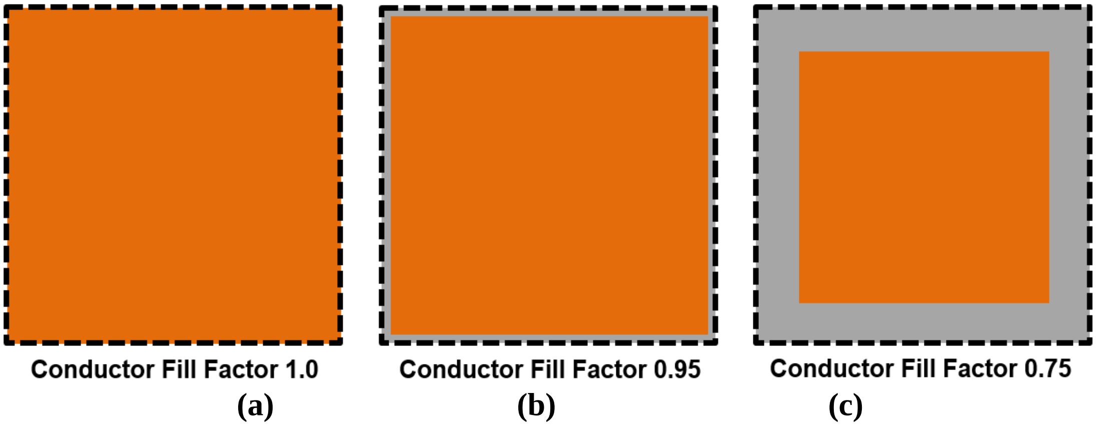

Fig.3.6-1 : Initial starting shapes. The dashed black line is the unit cell boundary.

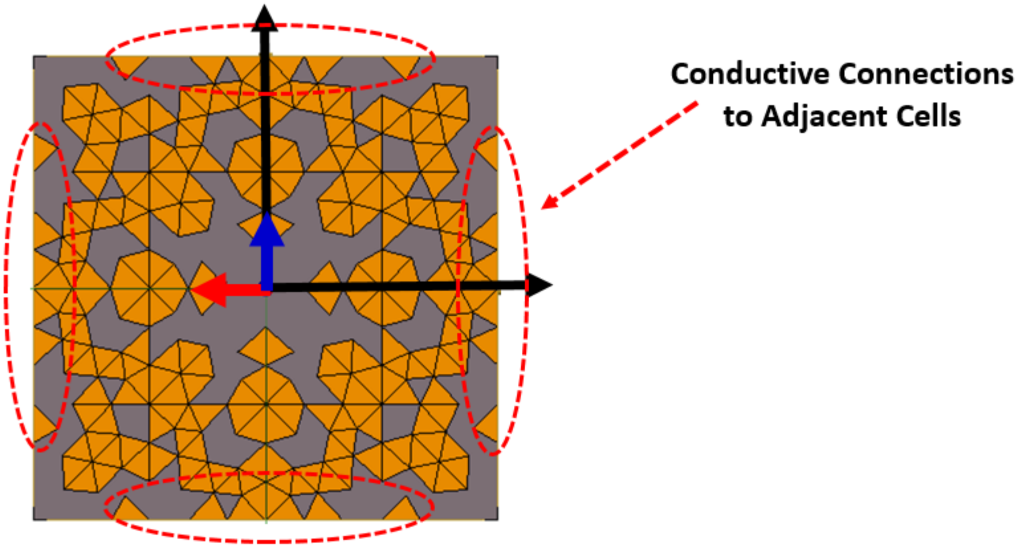

Fig.3.6-2 : Example of a shape-synthesized 1-layer element[36] for which there is conductive contact with adjacent elements.

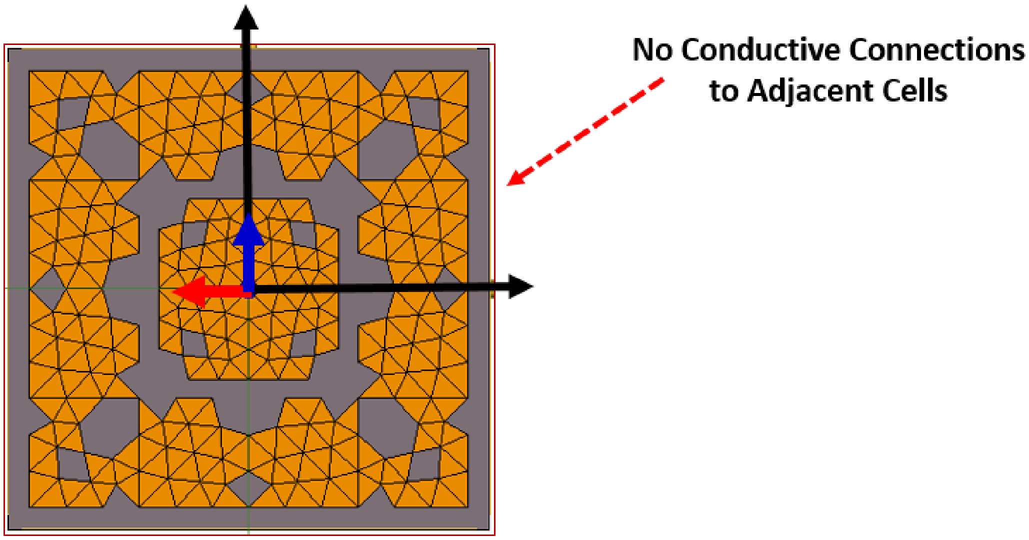

Fig.3.6-3 : Example of a shape-synthesized 1-layer element[37] for which there is not conductive contact with adjacent elements.

---

[36] Extracted from the discussion that will follow in Section 3.9.

[37] Also extracted from the discussion that will follow in Section 3.9.

3.6.3 Symmetry Constraints

The shaping controller is able to impose specific symmetry[38]. constraints during the shaping process. These are the full-symmetry and the rotational-symmetry shown in Fig.3.6-4. Reasons, of an electromagnetic performance nature, for enforcing such symmetries are discussed in Section 3.9, and later in Chapters 4 and 5. The computational consequences of enforcing symmetry are discussed in Section 3.9.2. Of course, one need not require the shaping controller to impose any symmetry at all.

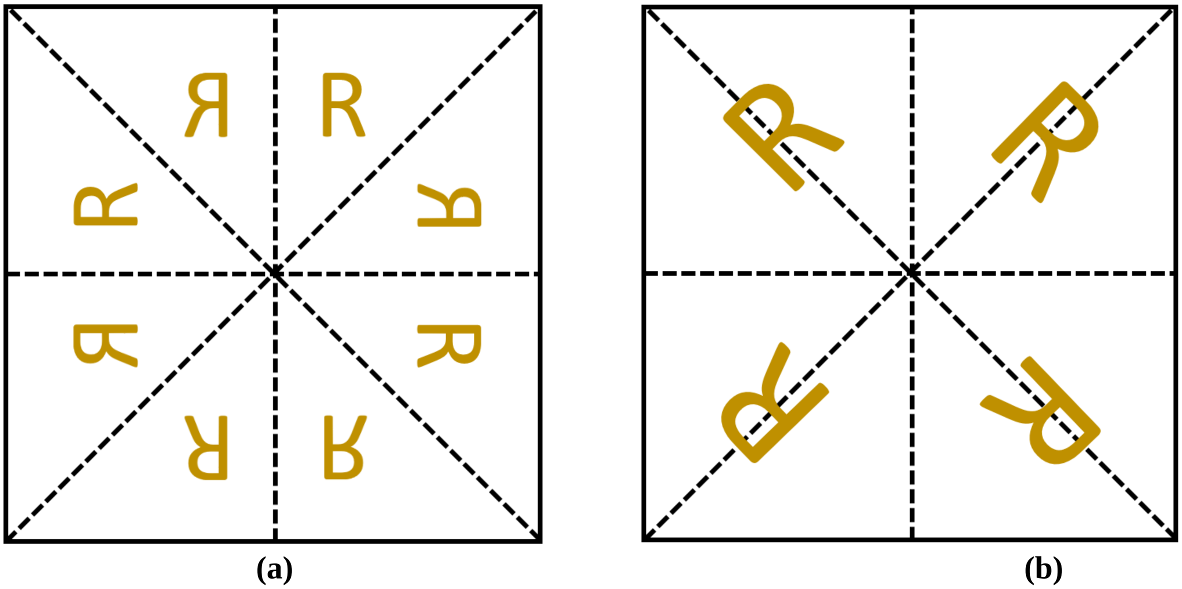

Fig. 3.6-4 : (a). Unit cell with conducting shapes that exhibit full symmetry, and (b). in which they exhibit rotational symmetry. The letter R represents conducting material.

3.6.4 Mesh Control

The starting shape is always a square, and in order to manifest this fact in the geometry the meshing of the starting shape is always done in the same customized way. We initially take $\Lambda_{\text{fill}} = 1$, and mesh the starting square (that now fills the complete cell) into N_{Δ} triangles in a customized

---

[38] We have in fact discovered that there is another way to achieve such symmetry “naturally” without directly enforcing it. If we use one polarization for the incoming field response in the fitness function during one iteration of the GA, and the orthogonal polarization during the next (and so on), the geometry of the element begins to evolve into a shape that takes on full symmetry. Albeit somewhat satisfying, it is a computationally long-winded approach.

manner[39] as follows : The 1st quadrant is meshed into $i = 1, 2, ..., N_\Delta / 4$ triangles, and the three vertex coordinates (x_i, y_i) of each triangle recorded. When doing this meshing for the 1st quadrant we already mesh symmetrically[40] about the diagonal (shown dotted in Fig.3.6-5). In quadrant #2 a set of $N_\Delta / 4$ triangles with vertices $(x_i, -y_i)$ are created by the geometry controller, in quadrant#3 a set with vertices $(-x_i, y_i)$, and in quadrant#4 with vertices $(-x_i, -y_i)$. Such customized meshing control is necessary to ensure it is free of any 'bias' that will prevent some desired symmetry from being precisely obtained. If Λ_{fill} for a starting shape is changed, all vertex coordinates are simply scaled by this factor. This preserves the numbering of all triangles. The final mesh is then injected back into FEKO. Although FEKO renumbers these triangles for computational purposes the shaping controller is not affected by this, as it always keeps its original numbering and related chromosome length.

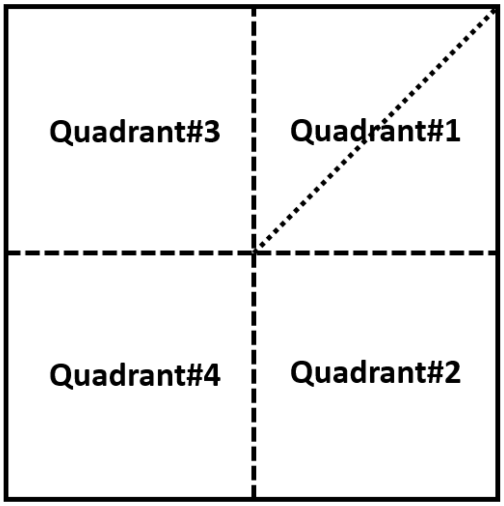

Fig. 3.6-5 : Quadrant numbering in a unit cell.

If a triangle is removed in quadrant#1 during shaping then : (a). 7 others corresponding triangles are removed at appropriate locations in all quadrants if full symmetry has been specified. (b). 3 additional corresponding triangles are removed at appropriate locations in all quadrants if rotational symmetry has been specified. Hence in the case of full symmetry the length of the geometry

---

[39] This is not an existing option in the FEKO code.

[40] This first step can be done directly using the FEKO code. The remainder of the operations are done by scripts developed separate from the FEKO code.

chromosome $[C_{shape}]$ is $N_{\text{bit}} = N_{\Delta}/8$, whereas for rotational symmetry $N_{\text{bit}} = N_{\Delta}/4$. It is worth restating that although FEKO renumbers these triangles for computational purposes the shaping controller is not affected by this, as it always keeps its original numbering and related chromosome length.

3.6.5 Archiving of Element Layers

Each element layer[41] that arises and receives a full-wave analysis is tagged. The full S-matrix of the layer, and its geometry data, is stored, and can be accessed at any later stage by simply specifying the tag. This archive, which grows as the set of transmitarray elements is shape synthesized, will be referred to as the layer collection. Further comments will be made in Section 4.3.2.

3.7 OBJECTIVE FUNCTION CONSTRUCTION

The need for defining an objective function in order to use optimization algorithms for the shape synthesis of transmitarray elements (or indeed any design purpose whatsoever) was given in Section 2.6. The proper choice of this function plays a crucial role in the success of the shaping process. It is best defined on a per problem basis, and so will be detailed when needed.

3.8 THE SHAPING PROCESS

By “shaping process” we mean the recipe that is followed by the shaping controller. In the case of 1-layer elements this recipe can be straightforwardly understood in terms of what will be described in Section 3.9. However, for the 3-layer element of interest in this thesis, the recipe is more complicated, since it is impractical to perform a shape synthesis that uses a full-wave CEM model for all three layer elements simultaneously.

As just commented, the shaping process for 1-layer elements is exercised in Section 3.9 that follows. In Chapter 4, where we shape synthesize single-band 3-layer elements, a different shaping recipe will be detailed. In Chapter 5, where we consider dual-band element shaping we will describe how the latter shaping recipe needs to be further altered (or customized). We mention that the shaping controller could also be used for the shape synthesis of elements in periodic lattices for

---

[41] On its own it may not have a high transmission magnitude because, unless we are shape synthesizing 1-layer elements, it is the performance of the cascaded layers that gives a multi-layer element its performance.

purposes other than transmitarray elements, and then different shaping processes will simply need to be "plugged in" to the shaping controller..

3.9 SHAPE SYNTHESIZING 1-LAYER ELEMENTS WITH FULL SYMMETRY

3.9.1 Preamble

Numerical experiments on the shape synthesis of 1-layer elements provided valuable knowledge on how the shaping tool behaves, and hence how it needed to be altered for improved operation.

3.9.2 Electromagnetic Consequence of the Full Symmetry Constraint

In this case, a conducting object is mirrored in the x-axis, the y-axis and the diagonal axes. We consider a linearly-polarized incident plane wave, with some orientation that we will call $\bar{E}_{\mathrm{co}}^{\mathrm{in}} = \hat{x}\,E_{\mathrm{co}}^{\mathrm{in}}$. In general the output will be the co-polarized field $\bar{E}_{\mathrm{co}}^{\mathrm{out}} = \hat{x}\,E_{\mathrm{co}}^{\mathrm{out}}$ and the cross-polarized field $\bar{E}_{\mathrm{cr}}^{\mathrm{out}} = \hat{y}\,E_{\mathrm{cr}}^{\mathrm{out}}$. In the case of full symmetry one finds that $E_{\mathrm{cr}}^{\mathrm{out}} << E_{\mathrm{co}}^{\mathrm{out}}$, as in a factor[42] less than 10^{-7}. This is true whether $E_{\mathrm{co}}^{\mathrm{in}}$ is x-polarized as described above, or in fact any other orientation is chosen to be the co- and cross-polarized fields. In this full-symmetry case we can write

$$E_{\mathrm{co}}^{\mathrm{out}} = S_{21}\,E_{\mathrm{co}}^{\mathrm{in}} \tag{3.9-1}$$

with S_{21} the element complex transmission coefficient.

---

[42] A number that would in theory be zero.

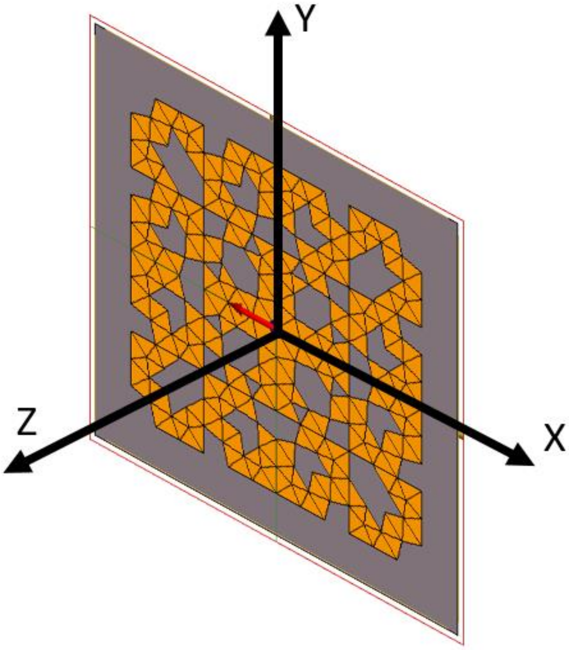

Fig. 3.9-1 : Coordinate system used in the full-wave CEM analysis of a 1-layer element (element layer) unit-cell in an infinite periodic environnement[43].

3.9.3 Convergence Checks[44] of the Computed Parameters

The transmitarray is made of isotropic passive materials only, thus it must be reciprocal. As a result the transmission coefficient of the overall element, irrespective of the number of layers, must be such that[45]

$$S_{12} = S_{21} \tag{3.9-2}$$

During synthesis[46], we will always consider lossless materials, and so we must have

$$|S_{11}|^2 + |S_{21}|^2 = 1 \tag{3.9-3}$$

$$|S_{22}|^2 + |S_{12}|^2 = 1 \tag{3.9-4}$$

---

[43] This in fact shows one of the shapes synthesized in Section 3.9.5, looking like a cross surrounded by a meandering outer loop.

[44] This was referred to in Section 3.3.2.

[45] These quantities have been defined in Section 2.5.

[46] Losses can be included in an analysis once a shape synthesis has been completed, and we wish to appreciate what the effect of small amounts of non-idealness on the part of the conductors, substrates and spacers is.

and

$$S_{11}^{*}S_{12} + S_{21}^{*}S_{22} = 0 \tag{3.9-5}$$

The first two are statements of conservation of power. The third is less easy to interpret on its own, but combined with the first two can be used to show [SAZO 82] that any lossless two-port satisfies the conditions

$$|S_{11}| = |S_{22}| \tag{3.9-6}$$

and

$$\angle S_{11} + \angle S_{22} = \angle S_{21} + \angle S_{12} \pm \pi \tag{3.9-7}$$

Obviously, for the reciprocal two-ports of interest here $\angle S_{21} = \angle S_{12}$, and the latter expression reduces to

$$\angle S_{11} + \angle S_{22} = 2\angle S_{21} \pm \pi \quad \Rightarrow \quad \angle S_{22} = 2\angle S_{21} - \angle S_{11} \pm \pi \tag{3.9-8}$$

In full-wave simulations the field is considered to be incident at Port#1, and so S_{11} and S_{21} are output. Any significant violation of (3.9-3) would be indicative of modelling errors of some sort. In this work, this condition is used by the shaping controller as an automatic check on the computational modelling at all stages, and a flag raised if such modelling error is detected. In multi-layer transmitarray elements we will need to know S_{22} and S_{12} as well. Rather than request the full-wave solution for a field incident at Port#2, we use (3.9-2), (3.9-6) and (3.9-8) to determine S_{22} and S_{12} without any further full-wave simulations. This obviously saves on computation time.

3.9.4 Objective Function Construction

A. Ideal Performance

An ideal element would have $|S_{21}^{\mathrm{Target}}| = 1$, so that the complex value is $S_{21}^{\mathrm{Target}} = e^{j\Psi_{\mathrm{Target}}}$, where $\Psi_{\mathrm{Target}} = \angle S_{21}^{\mathrm{Target}}$ is the desired phase shift. In the case of a lossless element this at once means that

$|S_{11}| = 0$. At each iteration we will find that the actual properties are $S_{21}^{\text{Actual}} = |S_{21}^{\text{Actual}}| e^{j\Psi_{\text{Actual}}}$. We will be satisfied if we are able to achieve.

- $B_{\min} < |S_{21}^{\text{Actual}}| < 1$: This means that the transmission coefficient magnitude need “only” be larger than $B_{\min}$. Typically we want $B_{\min} > 0.8$ (approximately -2.0 dB), but preferably closer to unity (0 dB).
- $|\Psi_{\text{Target}} - \Psi_{\text{Actual}}| \leq \Delta\Psi_{\text{Tol}}$: The largest deviation in the actual transmission phase from the desired value is $\Delta\Psi_{\text{Tol}}$. This value will depend on the particular aperture distribution, by examining the effect of such phase deviations on the final radiation pattern performance of the transmitarray antenna.

B. Objective Function – Type 1

$$F_{\text{obj}} = \begin{cases} C_{\text{large}} >> 1 & \text{if } |S_{21}^{\text{Actual}}| < 0.5 \\ \dfrac{\left|e^{j\Psi_{\text{Target}}} - S_{21}^{\text{Actual}}\right|^m}{|S_{21}^{\text{Actual}}|} \times |\Psi_{\text{Target}} - \Psi_{\text{Actual}}|^n & \text{Otherwise} \end{cases} \tag{3.9-9}$$

The exponents m and n are adjusted according to the rate of convergence observed. It has been found from experience that we usually need $1 \leq m \leq 3$ and $1 \leq n \leq 2$.

C. Objective Function – Type 2

$$F_{\text{obj1}} = \begin{cases} 0 & If \ |\Psi_{\text{Target}} - \Psi_{\text{Actual}}| < \Delta\Psi_{\text{Tol}} \\ |\Psi_{\text{Target}} - \Psi_{\text{Actual}}| & Otherwise \end{cases} \tag{3.9-10}$$

$$F_{\text{obj2}} = \begin{cases} 0 & If \ |S_{21}^{\text{Actual}}| > S_{\min} \\ \left|e^{j\Psi_{\text{Target}}} - S_{21}^{\text{Actual}}\right|^m & Otherwise \end{cases} \tag{3.9-11}$$

$$F_{\text{obj}} = \frac{1}{2}\sqrt{\mathrm{w}_1(F_{\text{obj1}})^2 + \mathrm{w}_2(F_{\text{obj2}})^2} \tag{3.9-12}$$

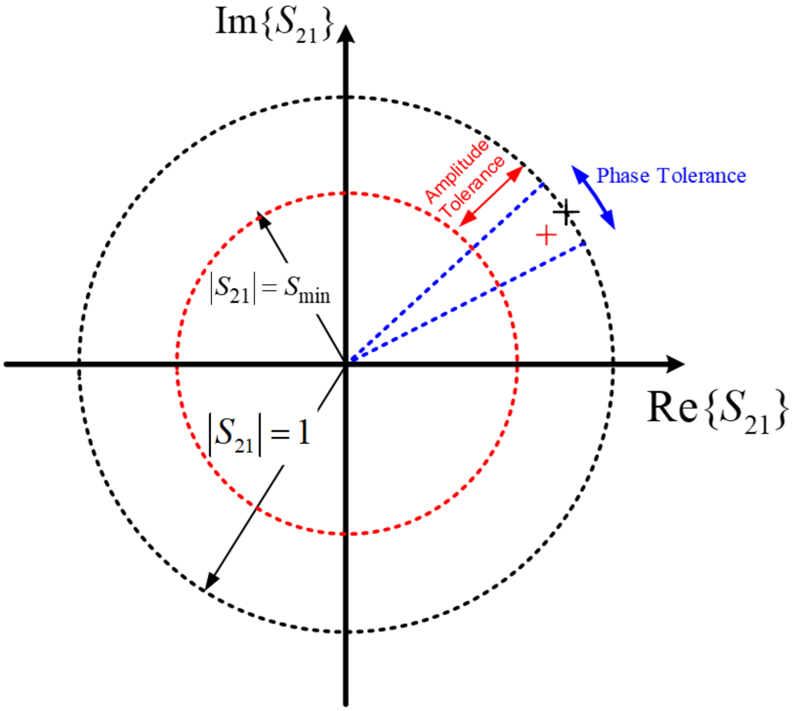

Fig.3.9-2 : Acceptable region around target performance

3.9.5 Two Sample Outcomes of the 1-Layer Element Shape Synthesis Process with Full Symmetry

The first application of the shaping controller tool was for 1-layer elements on substrate of $\varepsilon_r = 2.2$ and thickness 0.508mm, embedded in an infinite periodic structure with a square lattice of cells of fixed size of $\lambda_o / 3$, with $\lambda_o = 12.5mm$ at 24 GHz. The 'Type#1' objective function given in Section 3.9.4 is preferable, in particular with $m = 3$ and $n = 2$ in expression (3.9-9). Examples of two of the shaped element geometries are shown in Fig.3.9-3 and Fig.3.9-4. In both cases $\Lambda_{\text{fill}} < 0.9$.

Both the above figures show the "raw" 1-layer element shapes. In lieu of the comments in Section 2.5, as to how the RWG expansion functions are defined, we refer the reader to the annotated Fig.3.9-5, and offer the following explanation : Fig.3.9-5 repeats that in Fig.3.9-4 but identifies problematic triangles with single vertex-only connections (black circles), and others that are isolated single-triangle "islands" with their only connection to other triangles being via their vertices, or vertex-only connections (red circles). Such connections do not allow current flow for the RWG expansion functions used in the full-wave analysis, and so should not be realized as physical connections in practice. The “vertex breaking technique” identifies the single vertex connections in the MM mesh and generates two new distinct and physically separate vertices. The isolated islands are simply discarded since they would not have had expansion functions (and hence no current density) on them during full-wave simulations. The occurrences of what we have called problematic triangles is not really a deterrent because the fixing noted is easily done, and need at any rate only be done on those elements actually used. Furthermore, the occurrence of such cases are usually fewer than is shown in Fig.3.9-5; we selected this ‘riddled’ case for emphasis of the issue in question.

Before concluding, we note that the fully-symmetric 1-layer elements are not able to offer a full 360° phase range.

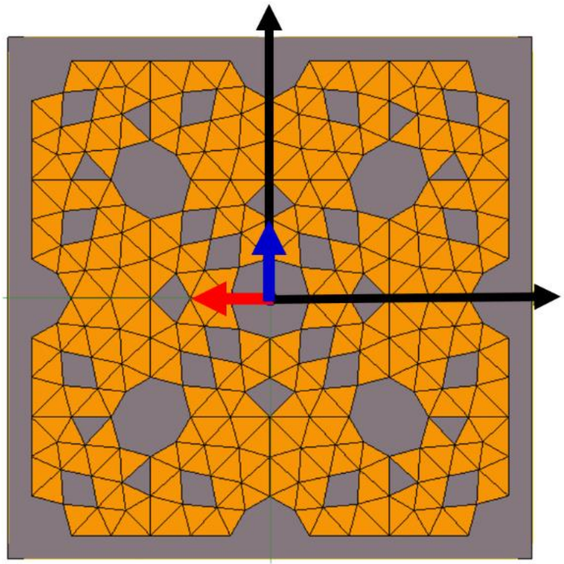

Fig.3.9-3. Example of a synthesized 1-layer element with transmission amplitude of -0.34dB (goal was 0dB) and transmission phase shift of 15.5° (goal was 15°).

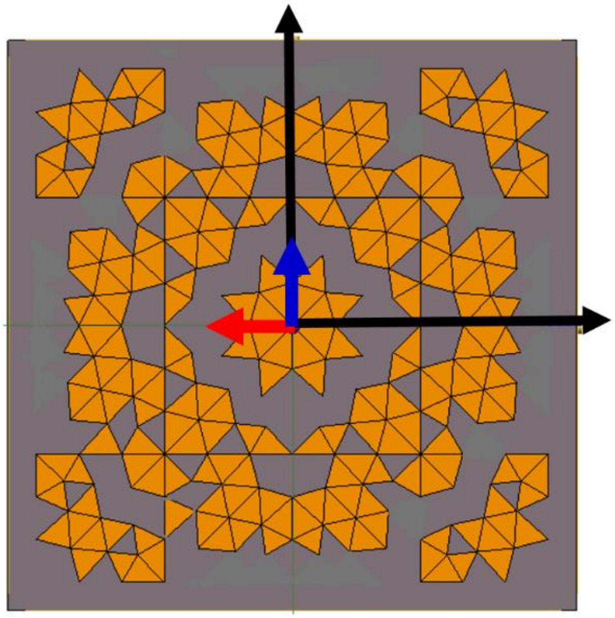

Fig.3.9-4. Example of a synthesized 1-layer element with transmission amplitude of -0.29dB (goal was 0dB) and transmission phase shift of -14.9° (goal was -15°).

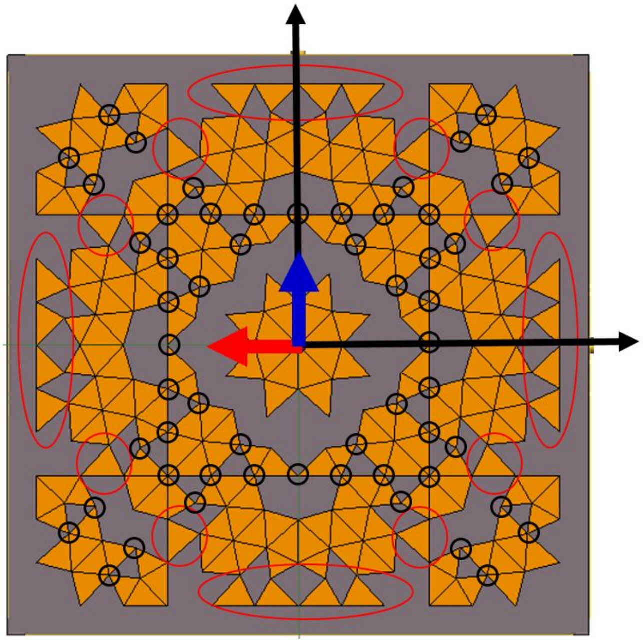

Fig.3.9-5. Repeated diagram of the element in Fig.3.9-4. The triangles encircled in red are those "islands" that would be eliminated prior to fabrication of such an element. Vertex-only connections, encircled in black, would be prized apart by a small amount ("vertex fixing") prior to fabrication, without any triangle removal.

3.10 CONCLUDING REMARKS

Chapter 3 has developed the machinery for a computational electromagnetics-based tool capable of performing the shape synthesis of multi-layer transmitarray elements for the first time. It has been developed in the form of a (relatively complex) controller script that carries out the desired shaping process by successfully manipulating a commercially available CEM engine and a commercially implemented genetic optimization algorithm. The use of a commercially available CEM engine (FEKO), and a commercially available GA algorithm (in MATLAB) means the shape synthesis tool developed can be accessible to others. It benefits from their superior pre- and post-processing capabilities, as it will do from the no doubt improved computational efficiency in their future upgrades. Another very important reason for using a commercial code such as FEKO is that files describing complicated shaped geometries can be exported for fabrication on printed circuit facilities; this is typically not so for in-house codes. This necessity will become especially clear in the experimental work in Chapter 6. However, it will hopefully already have been appreciated that the shaping controller is considerably more than merely "running FEKO". The shaping controller was first exercised on 1-layer elements to verify the correct functioning of all its parts. Even though 1-layer transmitarrays are not usually used, we conjectured in Section 2.7 that, if transmission phase quantization [ABDE 17] is used, there might arise some application where a 1-layer configuration might be an acceptable complexity/cost/performance design trade-off. The ability to actually shape synthesize 1-layer elements would allow one to establish the performance limitations of such elements, and their suitability, when an especially low-complex low-cost solution is perhaps desired.

CHAPTER 4

The Shape Synthesis of Single-Band 3-Layer-Elements with Full Symmetry

4.1 PRELIMINARY REMARKS

In Section 3.9 we used the shaping controller of Chapter 3 for the shape synthesis of the conducting shapes on individual 1-layer elements to provide a given phase shift and high transmission amplitude at a specified frequency. The goal in this chapter is the devising of a shaping process (to be 'plugged into' the shaping controller tool developed in Chapter 3), and the selection of problem-specific objective functions, for the shape synthesis of 3-layer single-band elements. In particular, we discuss 3-layer elements depicted pictorially in Fig.4.1-1, for which the shaping process described in Section 4.3 will assume[47] identical 1st and 3rd layers, and equal spacer thicknesses ($d_1 = d_2 = d$). The mixed full-wave/equivalent-circuit model for predicting a 3-layer element's performance, and reasons for using this model, are the subject of Section 4.2. General observations, and some specific outcomes, following the application of the shape synthesis very many times, are discussed in Section 4.4. Concluding remarks are given in Section 4.5.

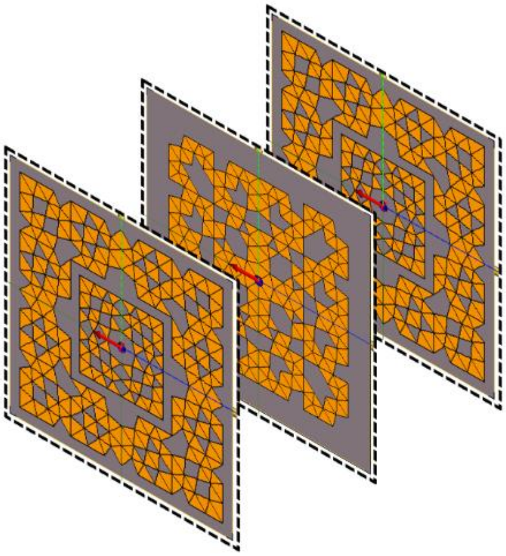

Fig.4.1-1 : Pictorial rendition of an individual 3-layer element. The spacers are not shown, and the spacings between the layers have been exaggerated.

---

[47] This assumption is related to the shaping process (or recipe) that needs to be defined and 'plugged into' the shaping controller that was developed in Chapter 3, and not an inherent limitation of the shaping controller itself.

4.2 MIXED FULL-WAVE / EQUIVALENT-CIRCUIT MODELLING OF 3-LAYER-ELEMENTS WITH FULL SYMMETRY

It is possible to use a full-wave analysis to characterise a complete 3-layer element, and this is feasible if one is performing analysis only. However, as noted earlier, during shaping such analyses need to be repeated an enormously large number of times, and some more computationally efficient approach is desirable for modelling the 3-layer element performance. During the shaping process we will continue to use the full-wave simulation methods with the usual infinite periodic structure assumption for the analysis of the separate single layers that constitute the complete 3-layer element. This full-wave model provides us with the plane wave (lowest-order Floquet mode) scattering matrix [S] of the periodic structure. The 3-layer-element spacers have a thickness d large enough that the higher-order Floquet mode coupling between cascades of such periodic structures can be ignored. The transmission performance of a 3-layer-element is then found by the well-known approach of multiplying the plane-wave ABCD matrices of the layers[48] and the spacers in the correct order, as depicted in Fig.4.2-1. It will be convenient to refer to this as the equivalent circuit model, any ABCD matrix being rigorously interpretable as an equivalent two-port network as shown in Fig.4.2-2.

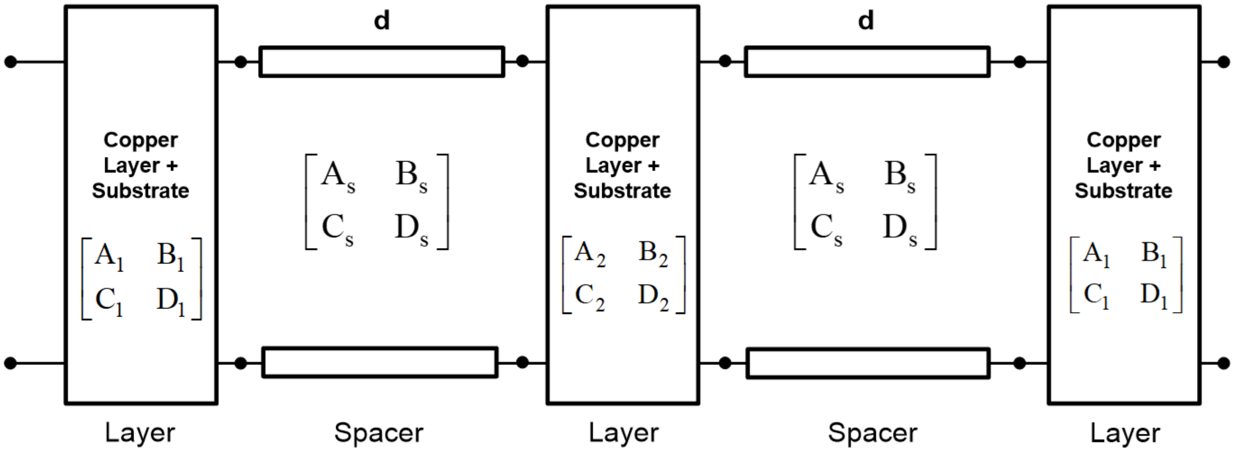

Fig.4.2-1 : Equivalent circuit model of a complete 3-layer element.

Because the substrate (but not the spacers) can be made relatively thin, simply being there in order to enable etching of the three layers, the series components in the T-equivalent circuit have a much

---

[48] Obtained directly from the scattering matrix.

smaller effect[49] than the shunt element. An approximate shunt equivalent circuit[50] for the layer-element is then that shown in Fig.4.2-3. If this holds, then the representation Fig.4.2-1 can be drawn in the simplified equivalent circuit form shown in Fig.4.2-4, with $B_1 = 1/X_{c1}$ and $B_2 = 1/X_{c2}$. It can be shown [SHAL95], [JOYA12] from network analysis that the input reflection of the 3-layer element (represented as in Fig.4.2-4) will be $S_{11} = 0$, and the transmission amplitude $|S_{21}| = 1$, as long as[51]

$$B_2 = \frac{2\left\{-B_1 + B_1 \tan^2(kd) + B_1^2 \tan(kd)\right\}}{B_1^2 \tan^2(kd) + 1 + \tan^2(kd) - 2B_1 \tan(kd)} \tag{4.2-1}$$

where $k = \omega\sqrt{\mu_0\varepsilon_0\varepsilon_r} = 2\pi f\sqrt{\mu_0\varepsilon_0\varepsilon_r}$, quantity ε_r being the relative permittivity of the spacer material (and not the substrate). This fact will be used in the shaping process to be described next in Section 4.3.

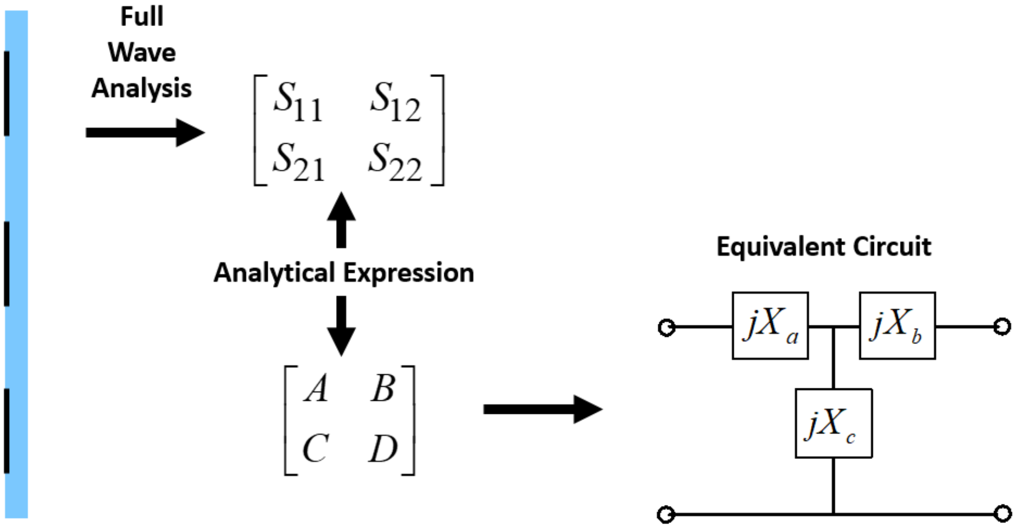

Fig.4.2-2 : Rigorous equivalent circuit for an element layer.

---

[49] Albeit not a negligible one.

[50] Even the thin substrate influences the value of the shunt element, and so needs to be included in the full-wave model, in essence because its presence effects the energy storage due to the evanescent Floquet modes in the vicinity of the conductor.

[51] [NEMA 15] suggests that the best bandwidth performance (theoretically greater than 20%) can be obtained for a 3-layer element when the $|B_i|$ values are less than 1.9.

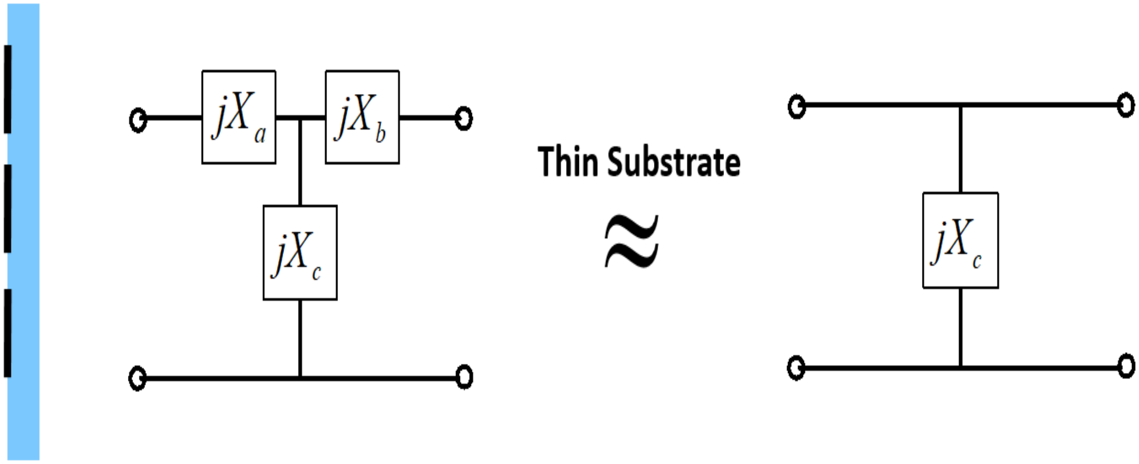

Fig.4.2-3 : Approximate equivalent circuit for an element layer with a very thin substrate.

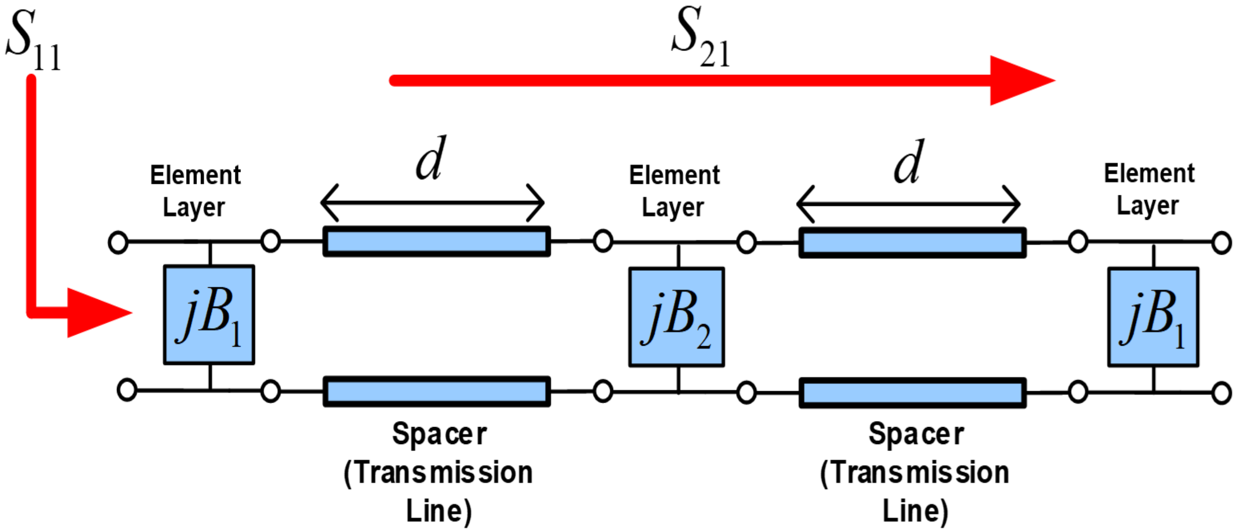

Fig.4.2-4 : Approximate equivalent circuit for a 3-layer element.

4.3 SHAPING PROCESS & OBJECTIVE FUNCTION FOR 3-LAYER ELEMENTS

4.3.1 Outline of the Shaping Process

The flowchart in Fig.4.3-1 shows the shaping process adopted for 3-layer elements. It will be described here. Although we do this in a way that might imply things were done manually, this is not so. It is automated by the shaping controller.

Once a desired phase shift is specified for a particular element the shaping proceeds as follows: The shape synthesis is performed on the 1st layer as in Section 3.9, and of course this means it is simultaneously done on the 3rd layer, since these are identical. At each step in the shaping process the value of B_2 that the 2nd layer must have for the current 3-layer element to have complete transmission can be determined using expression (4.2-1). These are then used, along with the [ABCD] of the 1st and 3rd layers being shaped, and those of the spacers, to determine the actual transmission phase of the current 3-layer element[52]. It is this that is used to evaluate the fitness function at the current iteration in the shaping process of the 3-layer element. Once this *primary shaping stage* has been finalized for the 1st and 3rd layers, the properties that the middle layer must have (on its own) for the 3-layer element to have 0dB transmission is known. A *secondary shaping stage* is then performed (again as for a single layer in Section 3.9) to determine the shape of this 2nd layer, the fitness function being evaluated using the transmission properties of this layer only. The complete 3-layer-element has then been shape synthesized.

The final performance ‘reported’ by the shaping controller for the said 3-layer element is found using the complete [ABCD] matrix[53] of the 2nd layer, and not its approximate shunt equivalent. The B_2 for a perfect match assumes the equivalent circuit of a layer is the latter approximate one. We explained earlier that, due to the presence of the substrate, albeit an electrically thin one, the series elements of the equivalent T-circuit are small but not negligible. Using the shunt-only versus the full T-circuit, the reported $\angle S_{21}$ for the complete 3-layer element might differ by as much as 5° from the originally specified value. This may be acceptable, especially if the transmitarray realization will use aperture quantization[54]. If the deviation is too large, the shaping process can

---

[52] Even though we do not yet know the shape of the 2nd layer that will provide the required B_2 .

[53] In other words the entire T-equivalent circuit.

[54] As mentioned in Section 2.3.

lookup ‘nearby’ B_i values in the layer archive[55] and check whether these provide a $\angle S_{21}$ closer (than 5°) to the desired value. We should state that whenever we refer to some operation as a “check”, it implies that these involve computation times that are negligible compared to a complete shape synthesis of a single layer.

4.3.2 Memory of Element Layers Encountered *En Route*

> “Those who cannot remember the past are condemned to repeat it”.
> George Santayana (1863-1952)

The starting conductor geometry in either the primary or secondary shaping process will undergo shaping through the removal or inclusion of “conducting pixels”. A complete set of shaped 3-layer elements can be obtained[56] in the manner described, as long as the number of iterations (and hence layer full-wave simulations) does not become too burdensome. We wish to assist the shaping controller to obtain solutions in fewer iterations, and to keep the number of required full-wave simulations to a minimum. This can be done in a number of ways. “Leftover” layers discarded by the shaping algorithm while attempting to find an element with a specified transmission phase are catalogued for later possible use. Indeed, each unique layer chromosome encountered has its full-wave response archived as affirmed in Section 3.6.5. If it reappears in some later iteration (eg. when shaping an element for a different transmission phase) its full-wave analysis need not be repeated. Such data is often what is needed for some middle layer, and then the secondary shaping need not be done. Thus, as the database for a particular centre frequency grows the shaping process becomes more computationally efficient by exploiting history.

For instance, consider a case where we find that, for a given $B_1 = B_3$, expression (4.2-1) shows that we need $B_2 = -0.13$, say, for a perfect match. And suppose we have an existing $B_i = -0.17$ shape in the archive. In such cases it is advantageous to use the $B_i = -0.17$ shape as the starting shape for the middle layer and run the shaping from there onwards to obtain a $B_2 = -0.13$.

Indeed, eventually there is such a large collection of B_i values with its associated shape that the shaping controller can be instructed to select each of these as $B_1 = B_3$ and check each of the

---

[55] Discussed in Section 4.3.2 that follows.

[56] As will be noted in Section 4.4.

available B_i values to see if some newly specified $\angle S_{21}$ requirement can be met with $|S_{21}| > -2\text{dB}$ and the resulting 'best' one[57] chosen as the shaped 3-layer element.

4.3.3 Objective Function

The objective functions used are the same as defined in Section 3.9.4, but of course used here for the complete overall 3-layer element. The 'Type#1' given in Section 3.9.4 is preferable, in particular with $m = 3$ and $n = 2$ in expression (3.9-9), as it almost always results in more rapid convergence of the shape synthesis of a specified element. It is noted that, for a specified element transmission phase, slightly different (albeit both successful) shapes are arrived at depending on which of the two types of objective function is used.

---

[57] Most favourable combination of $\angle S_{21}$ and $|S_{21}|$ for the stated specification.

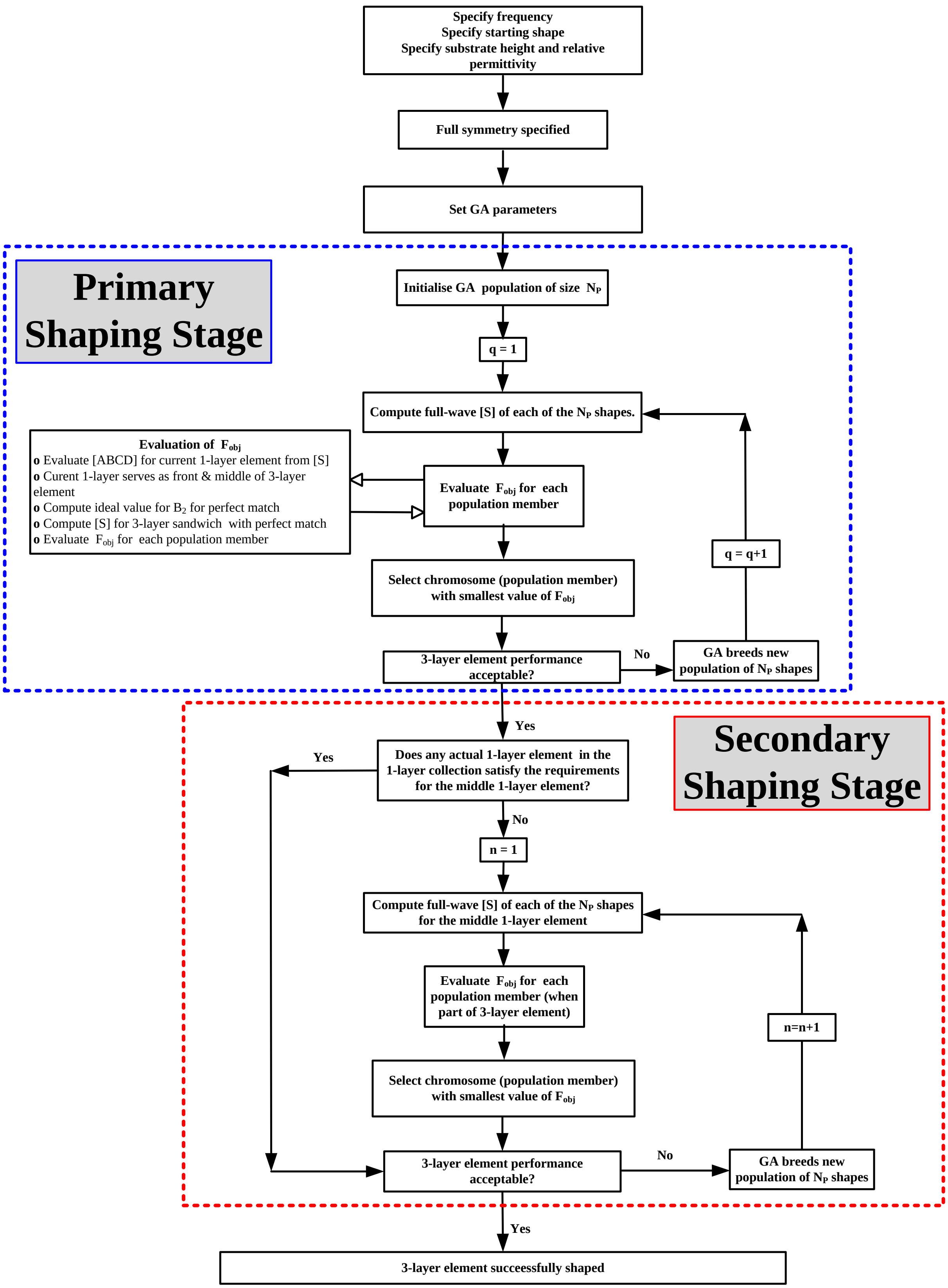

Fig.4.3-1 : Flowchart of the shaping process for a 3-layer element.

4.4 OUTCOMES OF THE SHAPE SYNTHESIS PROCESS

4.4.1 Goals

The objective was to build a database of shaped 3-layer-elements for operation at 24 GHz, and in so doing to simultaneously study the shape synthesis process itself. The substrates of the layers have $\varepsilon_r = 2.2$ and thickness 0.508 mm. At 24GHz, $\lambda_{\text{o}} = 12.5\,\text{mm}$ and $\lambda_{\text{e}} = \lambda_{\text{o}} / \sqrt{\varepsilon_r} \approx 8.4\,\text{mm}$, and so the substrate thickness of $h = 0.508\,\text{mm}$ is $h / \lambda_{\text{e}} = 0.06$ (or $h = \lambda_{\text{e}} / 16$). The cells are in a square lattice of $\lambda_{\text{o}} / 3$ per side. The spacers have thickness $\lambda_{\text{o}} / 4$. A value $N_{\Delta} = 448$ was selected, irrespective of the value of Λ_{fill}. This ensures that, at 24 GHz, the triangles have edge lengths less than $\lambda_{\text{o}} / 35$. Full symmetry was enforced, and hence the shape chromosome length was $N_{bit} = 56$. It is customary in engineering practice to put together a list of "Lessons Learned" after completion of some project. We do so here.

4.4.2 General Observations

We have experimented with square starting shapes with filling factors down to $\Lambda_{\text{fill}} = 0.4$. However, in the latter case, during shaping, the amount of conductor rapidly decreases and approaches the situation of almost no conductor at all, and the shape optimization stagnates. If one uses a square starting shape with $0.6 < \Lambda_{\text{fill}} < 1$ we find that it is possible to end up with a set of matched ($|S_{21}| > -2\,\text{dB}$)[58] 3-layer-elements for any $\angle S_{21}$ one wishes over a full 360° phase range using a reasonable number of generations. This assumes we will accept the desired $\angle S_{21} \pm 3^{\circ}$. With an exceedingly large number of generations one can obtain precisely the $\angle S_{21}$ desired. If we will accept the desired $\angle S_{21} \pm 5^{\circ}$, then in a reasonable number of generations it is possible to obtain $|S_{21}| > -0.5\,\text{dB}$ over a full 360° phase range. One question that we asked ourselves is whether it is possible to use a 3-layer element, consisting of three identical layers, with $|S_{21}| > -2\,\text{dB}$. This is indeed possible, but not over a full 360° phase range. In the journal literature, elements[59] covering the full 360° phase range, and composed of identical layers indeed all have more than 3 layers.

---

[58] But typically, $|S_{21}| >> -1\text{dB}$.

[59] Not shape synthesized ones, but ones with pre-defined shapes, with adjustable features dimensions.

The shaping process does not provide a unique transmitarray element for a given phase shift. Many different shapes (eg. when different F_{obj} types are used) might have exactly the same phase shift at a single frequency; the expectation is that one such element may have a wider bandwidth than another, or have a slightly higher transmission amplitude, for example. A specified $\angle S_{21}$ can be obtained from a 3-layer element comprised of several possible shape combinations, with slight variations in their $|S_{21}|$ values (eg. -0.2dB, -0.4dB or -0.6dB). It is seldom possible to find a result that has $|S_{21}| = 0\,\text{dB}$, which is the perfect match case. The reason is that it is not always possible to find a shape that, when used for the middle layer, has precisely the value of B_2 needed for the perfect match. For example, if $B_2 = 0.2345$ is needed for a perfect match, it might only be possible to find shapes that offer values in the range $B_2 = 0.2345 \pm 1\%$, for instance, resulting in the $|S_{21}|$ values mentioned above, each giving the specified $\angle S_{21}$ within $\pm 3^\circ$. When the value of $|B_2|$ for a perfect match is very small (eg. 0.012), then it is not always possible to find an acceptable shape for this layer from the archived layer collection because even small changes in these small values result in too large a change in S_{21}. It is then necessary to shape synthesize the layer for this required B_2 from scratch. Alternatively, if one is a substantial way into the database generation process, and the layer archive is numerous, one can retain the value of B_2 in the collection closest to the required B_2, and then by direct one-by-one checking use this value in conjunction with all other B_i values (for $B_1 = B_3 = B_i$) and check if there is one that provides the desired $\angle S_{21}$ and $|S_{21}|$. This might even be interpreted as machine learning!

For certain specified transmission phases the shaping process showed slow progress from one iteration to another. This could sometimes be repaired by refining the mesh, which then allows the process to incorporate smaller gaps between parts of the conducting shape. However, while this may help the iteration-to-iteration progress, the computational burden of the repeated full-wave analyses increases and the time to completion of the shaping process does not improve because the shape-chromosome becomes too long. As the database of 3-layer elements built up the intermediate shapes of such elements that were “struggling” to achieve some desired $\angle S_{21}$ were examined. The insight gained suggested an alternative starting shape, namely that shown in Fig.4.4-1. It appeared that this allowed the shaping process to exploit a small gap between the outer and inner portion of the conductor shape (that it appeared to be trying to do) without one having to use extra fine meshing.

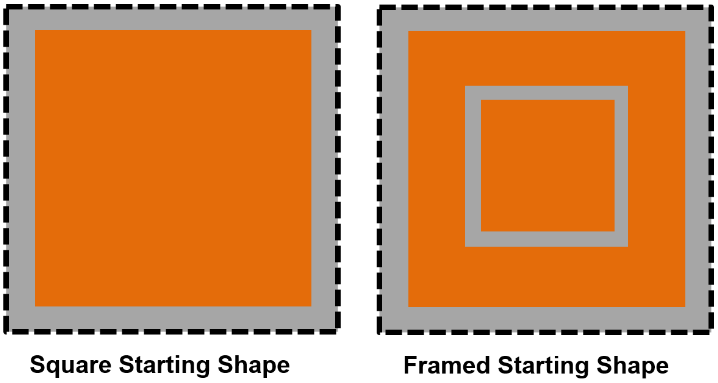

Fig.4.4-1 : Framed (right), as opposed to a square (left), starting shape. The cell boundary is the dashed line, conductors are orange, and the substrate is grey. Gap sizes are shown exaggerated.

4.4.3 Comments on the Shape-Synthesized 3-Layer Single-Band Elements

Fig.4.4-2 sums up the computed performance of some 3-layer shape synthesized single-band elements. The complex transmission coefficients are depicted by an asterisk. This is not the complete database; we have singled out and included certain elements to allow the diagram to facilitate the discussion that follows:

▪ Firstly, it is clear that it is possible to achieve a full 360° phase range with elements whose transmission magnitude is larger than 0.8 (-2dB), indeed closer to 0.9 (-1dB).

▪ Secondly, in the regions surrounded by black dashed lines, we have purposefully included elements that are redundant to emphasise that different element shapes can provide the same transmission phase with only slightly different values of transmission magnitude. Indeed, the fact that the plot is 'thick' over some regions means that these slightly different element shapes in fact provide not only almost identical phases but also magnitudes. Precisely which elements are selected might depend on other considerations, such as etching tolerances for instance.

▪ Thirdly, the blue dashed lines identify some demanded performance regions where the shape synthesis process takes many more iterations to come up with a capable element shape. Fortunately, it does eventually do so, and the small 'gaps' are always eventually filled in to obtain elements with the transmission magnitude greater than the minimum required. This is not always so for conventional fully-symmetrical element shapes if the number of layers is too few.

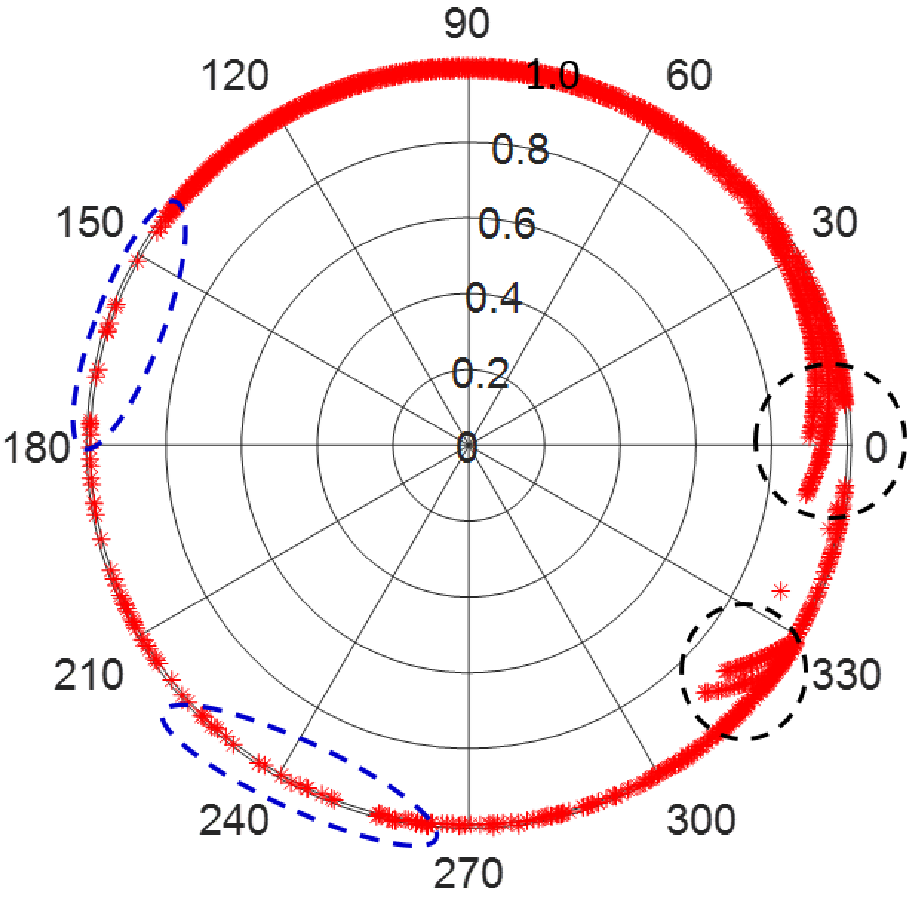

Fig.4.4-2 : Argand diagram (polar plot) of the complex transmission coefficients of selected shape synthesized elements in the database. The radial axis is the transmission coefficient magnitude (not in dB), and the angle shown is the transmission coefficient phase (in degrees).

It is worthwhile to examine the performance of two single-band 3-layer elements versus frequency. These have been purposefully handpicked for exposure here because of the difference in their behaviour over frequency. It must be recalled that the objective function (3.9-9) used in this chapter was evaluated at 24 GHz only; it has no knowledge of how the element is performing on either side of this frequency and would not have made any attempt to enlarge bandwidth during shaping. Thus the first example, whose computed transmission behaviour is that in Fig.4.4-3 and Fig.4.4-4, satisfies the requirements demanded, but has a stop-band just below 24 GHz. The shape-synthesized 3-layer element whose behaviour is given in Fig.4.4-5 and Fig.4.4-6, on the other hand has good transmission amplitude over a much wider band around 24 GHz, as well a transmission phase that changes more slowly with frequency.

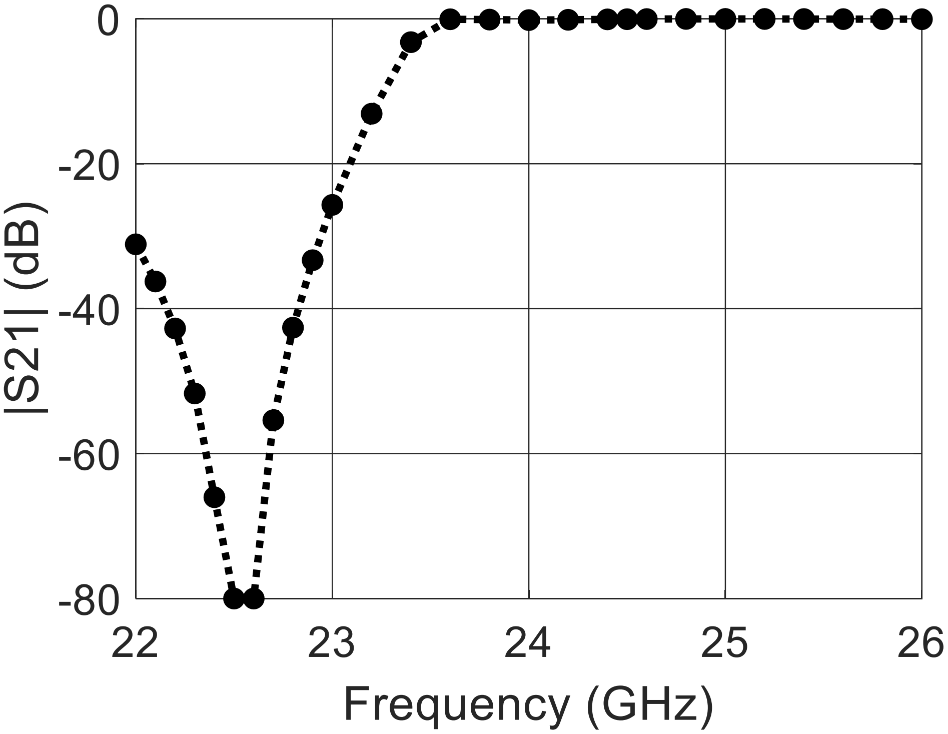

Fig.4.4-3 : Transmission magnitude versus frequency for 1st selected single-band element example, shape-synthesized for a transmission phase of -135° at 24 GHz.

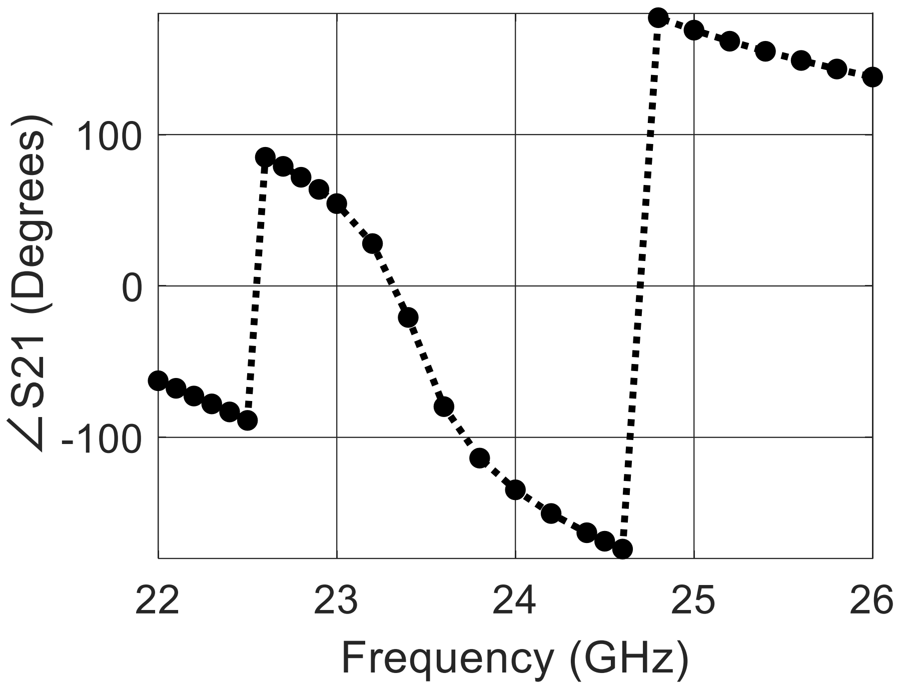

Fig.4.4-4 : Transmission phase versus frequency for 1st selected single-band element example, shape-synthesized for a transmission phase of -135° at 24 GHz.

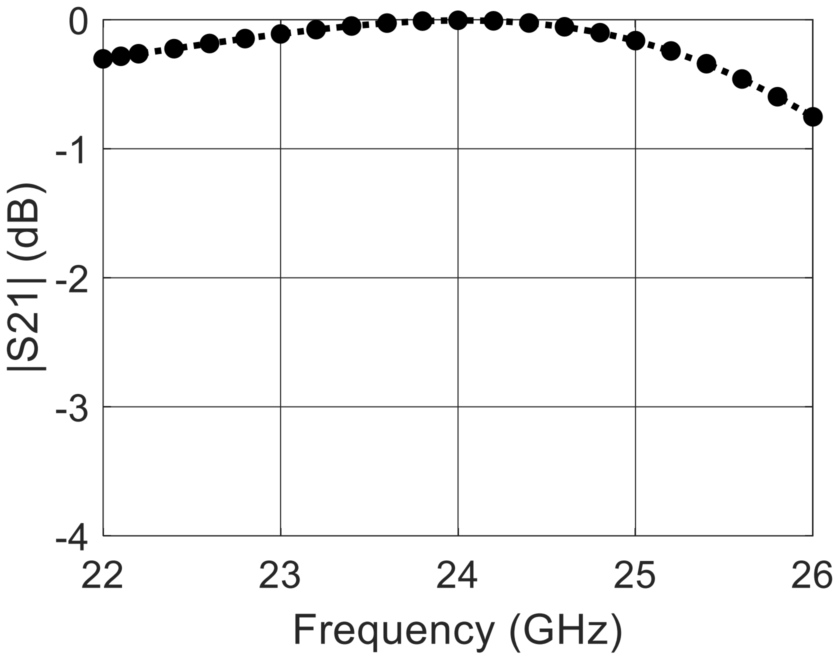

Fig.4.4-5 : Transmission magnitude versus frequency for 2nd selected single-band element example, shape-synthesized for a transmission phase of 90° at 24 GHz.

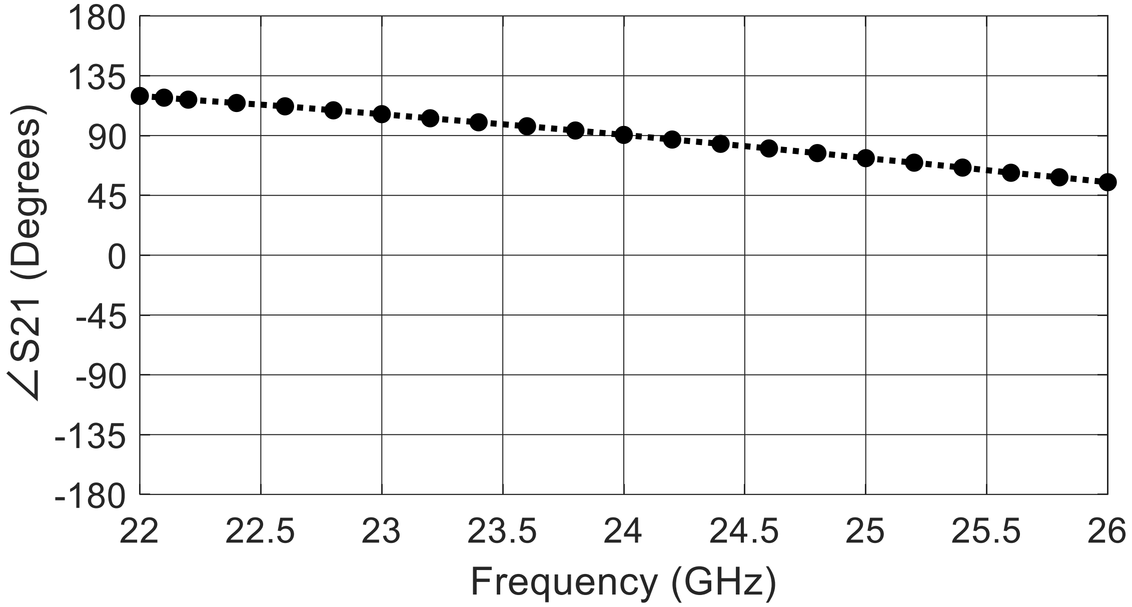

Fig.4.4-6 : Transmission phase versus frequency for 2nd selected single-band element example, shape-synthesized for a transmission phase of 90° at 24 GHz.

Next, Table 4.4-1 shows the conductor geometry on the layers of four other single-band shape synthesized 3-layer transmitarray elements. We show the shapes without the single-vertex connections removed; before actual element fabrication is done these are removed using the "vertex breaking technique" mentioned in Section 3.9.5. It is clear that the shapes are highly complex and cannot be described in terms of a small number of dimensions. Fortunately, as stated in Chapter 3, the fact that the shaping controller has been developed to interpret the commercial CEM engine's resource files means it can exploit all that the latter is able to provide as far as CAD graphical capabilities for picturing the geometry, and the export of CAD files for fabrication purposes, are concerned.

Table 4.4-1 : Selected shape-synthesized 3-layer-elements.

Phase Shifts	Front & Back Layers (Identical)	Middle Layers
Specified 130° Synthesized 130.4°	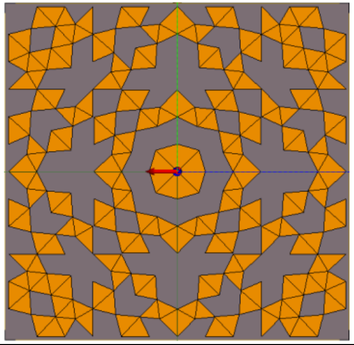	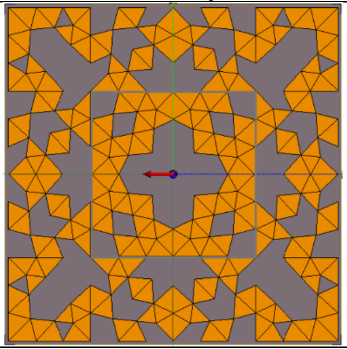
Specified -31° Synthesized -31.12°	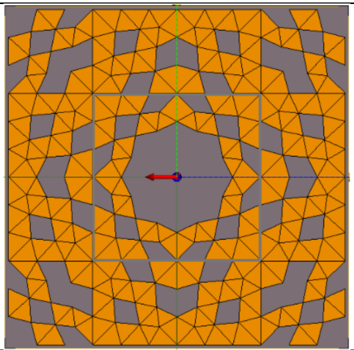	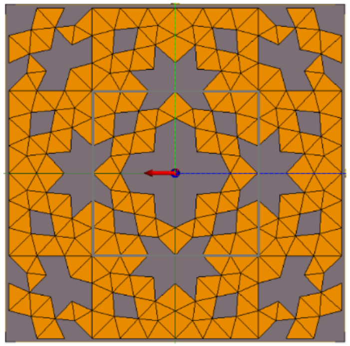
Specified 126° Synthesized 126.2°	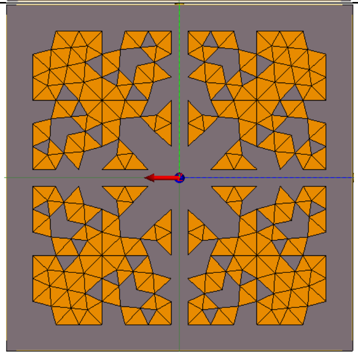	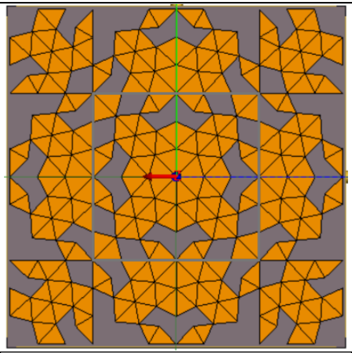
Specified -170° Synthesized -169°	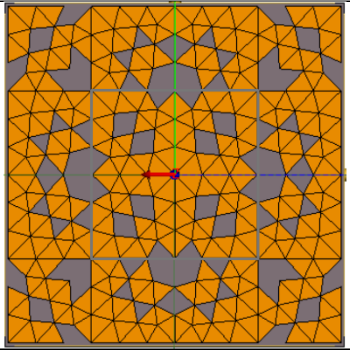	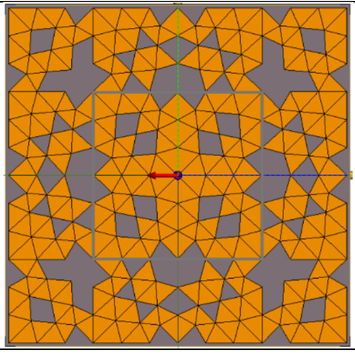

4.5 CONCLUDING REMARKS

The shape synthesis of multi-layer frequency selective surfaces, reflectarray elements or transmitarray elements has not yet been reported in the literature. Full-wave computational considerations discourage an approach where such rigorous analysis is used for the complete structure during shaping. In Section 4.2 we developed a mixed full-wave/equivalent-circuit modelling route that avoids this, and yet effectively ensures that full-wave information on the individual layers is used. This allowed us, in Section 4.3, to devise a customized shaping process and objective function for single-band fully-symmetric 3-layer transmitarray elements that cover a complete 360° transmission phase range. The full symmetry ensures that such elements are usable for both linear polarizations, and hence circular polarization, this being previously available (for the full 360° phase range) only for elements with more than three layers, when conventional (unshaped) elements are used. For instance[60], a double-loop conductor geometry offers the full 360° phase range with $|S_{21}| > -1\,\mathrm{dB}$, but only with 4 layers. The 3-layer spiral dipole conductor geometry provides the full 360° phase range with $|S_{21}| > -4\,\mathrm{dB}$, 320° with $|S_{21}| > -3\,\mathrm{dB}$, and 270° with $|S_{21}| > -1\,\mathrm{dB}$.

The shape synthesis approach could be altered[61], by a change in the definition of the objective functions, to come up with 3-layer elements that have a specific transmission phase variation over a particular frequency band. This would, of course, increase the computational burden as full-wave analyses of the individual layers would be repeatedly needed at several frequencies. By a similar change in the objective function definition, the shaping approach could be used for 3-layer reflectarray elements or frequency selective elements. In other words, the beauty of being able to perform such shape synthesis of multi-layer elements is that very specific requirements can be 'bred' into such elements, as conjectured in Section 2.7.

---

[60] See Table 2.4-1.

[61] In this chapter the objective function involved the performance of the 3-layer element at the centre-frequency only.

CHAPTER 5

The Shape Synthesis of Dual-Band 3-Layer-elements

5.1 PRELIMINARY REMARKS

The long-term goals of antenna shape synthesis generally, were pondered in Section 2.7. We indicated there that this thesis wishes to contribute to these lofty goals by developing a shape synthesis method, and associated tool, for transmitarray antenna elements. We needed an approach that is actually feasible in practice. The first step was the development, in Chapter 3, of the complex computational electromagnetics-based shaping controller tool capable of performing the shape synthesis of transmitarray elements. Such a facility had not been previously available. It was developed in such a way that different applications could be handled by simply writing customized "plug-ins" that define the problem-specific shaping process and objective functions. Using this tool, Chapter 4 demonstrated, for the first time, the shape synthesis of single-band 3-layer transmitarray elements. Previously, 3-layer elements capable of providing a full 360° phase range, and capable of accepting either principal linear polarization (and as a consequence circular polarization too), were not available. In the speculation on possible future requirements in Section 2.7, one example mentioned was a set of dual-band transmitarray elements capable of providing completely different prescribed transmission phases at the two different frequencies. In this chapter we therefore investigate the possibility of shape synthesizing such elements using a 3-layer configuration. The customized shaping process and objective function plug-ins for the shaping controller, needed to achieve this, are described in Section 5.2. The outcomes of the shape synthesis process are discussed in Section 5.3. The chapter is concluded by Section 5.4.

5.2 CUSTOMIZED INSERTS FOR THE SHAPING CONTROLLER

5.2.1 Customization of Two Plugins for the Shaping Controller

The assumption is that we have transmitarray designs[62] that each require N_e different elements, with each of the N_e elements in a specific design requiring different independently prescribed transmission phases at f_a and at f_b. We will refer to $\{\mathcal{U}_e(f_a), \mathcal{U}_e(f_b)\}$ as the paired sets of transmission phases required by the *e*-th element for the particular transmitarray design.

The shaping controller developed in Chapter 3 can carry out the shaping of dual-band[63] elements but, as noted in Section 3.7 and 3.8, a problem-specific objective function and customized shaping process need to be specified for such a new goal. Typically these are set up, then a few trial runs performed, and the shaping process and objective function refined using this experience. The descriptions in the two sub-sections that follow refer to this refined version. It is based on exercising the shaping process with different sets $\{\mathcal{U}_e(f_a)\}$ and $\{\mathcal{U}_e(f_b)\}$, and then structuring the common observations[64].

5.2.2 Objective Functions for Dual-Band Shape Synthesis

In the interests of clarity we will label the objective functions consecutive with those defined in Section 3.9.4; thus the two we will list below are Type 3 and Type 4. Many of the symbols used for the single-band case in Chapter 4 are re-used here.

A. Objective Function – Type 3

At some frequency f_p we define

$$F_{\text{obj1}}(f_p) = \begin{cases} 0 & \textit{If } \left|\Psi_{\text{Target}}(f_p) - \Psi_{\text{Actual}}(f_p)\right| < \Delta\Psi_{\text{Tol}}(f_p) \\ \left|\Psi_{\text{Target}}(f_p) - \Psi_{\text{Actual}}(f_p)\right| & \textit{Otherwise} \end{cases} \tag{5.2-1}$$

---

[62] By this we mean the process of Section 2.3 has been completed, whereby we know what the transmission phase of each element must be.

[63] The two frequencies will be denoted by lower band frequency f_a and upper band frequency f_b.

[64] The numerical experiments were done using $f_a = 18\,\text{GHz}$ and $f_b = 24\,\text{GHz}$, with various sets of different required transmission phases.

$$F_{\mathrm{obj2}}(f_p) = \begin{cases} 0 & If\ \left|S_{21}^{\mathrm{Actual}}(f_p)\right| > S_{\min}(f_p) \\ \left|e^{j\Psi_{\mathrm{Target}}(f_p)} - S_{21}^{\mathrm{Actual}}(f_p)\right|^m & Otherwise \end{cases} \tag{5.2-2}$$

and the overall objective function as

$$F_{\mathrm{obj}} = \frac{1}{4}\sqrt{\mathrm{w}_1\{F_{\mathrm{obj1}}(f_a)\}^2 + \mathrm{w}_2\{F_{\mathrm{obj2}}(f_a)\}^2 + \mathrm{w}_3\{F_{\mathrm{obj1}}(f_b)\}^2 + \mathrm{w}_4\{F_{\mathrm{obj2}}(f_b)\}^2} \tag{5.2-3}$$

B. Objective Function – Type 4

$$F_{\mathrm{sub}}(f_p) = \begin{cases} C_{\mathrm{large}} >> 1 & \text{if } \left|S_{21}^{\mathrm{Actual}}(f_p)\right| < 0.5 \\ \dfrac{\left|e^{j\Psi_{\mathrm{Target}}(f_p)} - S_{21}^{\mathrm{Actual}}(f_p)\right|^m}{\left|S_{21}^{\mathrm{Actual}}(f_p)\right|} \times \left|\Psi_{\mathrm{Target}}(f_p) - \Psi_{\mathrm{Actual}}(f_p)\right|^n & \text{Otherwise} \end{cases} \tag{5.2-4}$$

and the overall objective function is

$$F_{\mathrm{obj}} = \frac{1}{4}\sqrt{\mathrm{w}_1\{F_{\mathrm{sub}}(f_1)\}^2 + \mathrm{w}_2\{F_{\mathrm{sub}}(f_2)\}^2} \tag{5.2-5}$$

The case of elements with rotational symmetry will (in Section 5.2.3) be seen to be necessary. In such a case, for input $E_{\mathrm{co}}^{\mathrm{in}}$, one finds[65] that the relative magnitudes of $E_{\mathrm{co}}^{\mathrm{out}}$ and $E_{\mathrm{cr}}^{\mathrm{out}}$ depends on the particular element geometry. If a rotationally symmetric element is to be used and we wish to have $E_{\mathrm{cr}}^{\mathrm{out}} < \xi E_{\mathrm{co}}^{\mathrm{out}}$, where $0 \le \xi \le 1$ is some specified factor, then such a constraint has to be incorporated in the objective function during shaping. The reason is that some rotationally symmetric shapes satisfy this requirement whereas others do not. This shows an advantage of the shape synthesis approach developed in this thesis. In the dual-band element shape synthesis we have

---

[65] In contrast to what was found for fully symmetric elements in Section 3.9.2.

used we set $\xi = 0.1$, and if $\left|E_{\text{cr}}^{\text{out}}\right| / \left|E_{\text{co}}^{\text{out}}\right|$ exceeds this, we set F_{obj} equal to a large value so that such shapes are rejected.

5.2.3 Shaping Process for Dual-Band Shape Synthesis

The intention for the dual-band case had been to use the “perfect match approach” with full element symmetry, similar to what was done in the single-band element shaping process of Section 4.3.1. In other words : ■ *Primary Shaping Stage* **:** Identical front and back layers are assumed. We specify the desired $\angle S_{21}(f_a)$ and $\angle S_{21}(f_b)$, and then run the shaping controller to the end of this primary stage, where we have these values accompanied by sufficiently high $\left|S_{21}(f_a)\right|$ and $\left|S_{21}(f_b)\right|$ values. This means we have the actual conductor shapes on the 1st and 3rd layers that provide $B_1(f_a) = B_3(f_a)$ and $B_1(f_b) = B_3(f_b)$, but we know only the ideal $B_2(f_a)$ and $B_2(f_b)$ needed[66] and not yet the conductor shapes that will give us the latter quantities. ■ *Secondary Shaping Stage* : We then shape synthesize the 2nd (middle) layer to obtain one that provides the required $B_2(f_a)$ and $B_2(f_b)$.

One finds that, even at the primary stage, when one *assumes the theoretically perfect values* for $B_2(f_a)$ and $B_2(f_b)$ exist, it is still possible to achieve[67] roughly only 70% of the required $\{\mathcal{U}_e(f_a), \mathcal{U}_e(f_b)\}$ phases at *both* f_a *and* f_b. In other words, it is possible to achieve the complete set $\mathcal{U}_e(f_b)$, say, but not all of the associated set $\mathcal{U}_e(f_a)$ as well, without unacceptably low transmission magnitude at the latter frequency, and vice versa. The further the f_a and f_b are apart the more difficult this issue becomes. If one next proceeds to actually determine the conductor shapes that will provide the required $B_2(f_a)$ and $B_2(f_b)$ for a perfect match[68], it is found that it is possible to achieve only about 40% of the required $\{\mathcal{U}_e(f_a), \mathcal{U}_e(f_b)\}$ as completely shaped elements. Closer investigation revealed that, for the dual-band case, the situation sometimes arises

---

[66] Using expression (4.2-1).

[67] Of course, by “achieve” we mean the required transmission phase values, and a transmission magnitude larger than -2dB.

[68] At those values of $\angle S_{21}(f_a)$ and $\angle S_{21}(f_b)$ actually found possible using the ideal values of these quantities.

where the ideal $B_2(f_a)$ and $B_2(f_b)$ are such that $B_2(f_b) > B_2(f_a)$, whereas shapes with full symmetry generally exhibit $B_i(f_a) < B_i(f_b)$. The number of degrees of freedom available was therefore increased by using elements with rotational symmetry[69] for which it is possible to find elements with $B_i(f_a) > B_i(f_b)$ as well. If we consider the set of all possible conductor shapes, then those that possess geometrical rotational symmetry form a subset of this, whereas those that have geometrical full symmetry are a subset of the latter. Although use of elements with such rotational symmetry is found to greatly increase the number of completely realized[70] 3-layer elements with dual-band performance, this is still only possible for about 80% of the required $\{\mathcal{U}_e(f_a), \mathcal{U}_e(f_b)\}$.

Two routes allowed this unsatisfactory state of affairs to be circumvented: (a). Firstly, it was important to remember that having no conductor in a layer also provides a shunt susceptance B_i; (b). Secondly, it was recognized that it was necessary to unfetter the shaping controller even further by adopting an alternative to the perfect match approach, but of course while still retaining structure in the dual-band element shaping process. With reference to Table 5.2-1, we see that configuration#1 is the only one we have been considering thus far. Fortunately, by the time the shaping controller has reached the point where the "80% roadblock" mentioned at the end of the previous paragraph, the single-layer collection[71] that has been archived *en route* is quite vast, and rapid checks of the alternative combinations shown in Table 5.2-1 soon produce the elements need to complete the required dual-band element set $\{\mathcal{U}_e(f_a), \mathcal{U}_e(f_b)\}$. Machine learning has been defined as an application of artificial intelligence that provides systems the ability to automatically learn from experience without being explicitly programmed; in a sense this is what is being done here as the layer collection is added to each time a new shape synthesis is performed.

Fig.5.2-1 provides the flow chart of the refined dual-band shaping process. Fig.5.2-2 simply plots the $\{\mathcal{U}_e(f_a), \mathcal{U}_e(f_b)\}$ pairs from the shape synthesis experiments (mentioned at the end of Section 5.2.1) performed on different sets of prescribed transmission phase pairs. This is intended to indicate that one can obtain whatever sets of transmission phase pairs one wishes in a 'dial-up' fashion.

---

[69] We note that some elements have one of their layers that is fully symmetrical, but not all three of their layers.

[70] Those for which the actual conductor shapes are know for all three layers.

[71] Whose idea was previously referred to in Section 3.6.5 and Section 4.3.1.

Table 5.2-1 : Alternative Dual-Band Element Configurations

Index of Configuration	Configuration
1	$B_1 \Leftrightarrow B_2 \Leftrightarrow B_1$
2	$B_1 \Leftrightarrow B_1 \Leftrightarrow B_1$
3	$B_1 \Leftrightarrow B_1 \Leftrightarrow B_3$
4	$B_1 \Leftrightarrow B_3 \Leftrightarrow B_3$
5	$B_1 \Leftrightarrow B_2 \Leftrightarrow B_3$

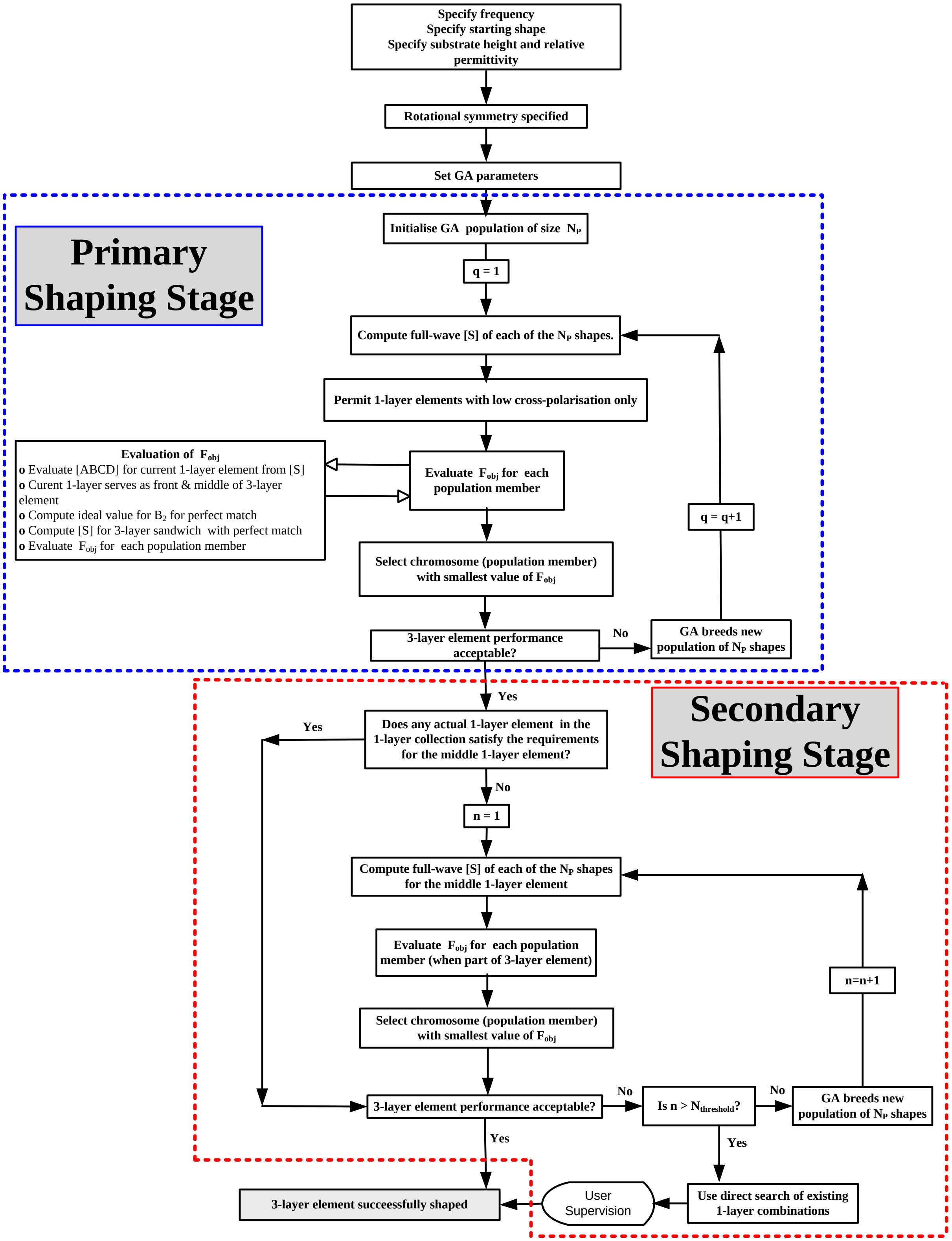

Fig.5.2-1 : Flowchart of the refined shaping process for dual-band elements.

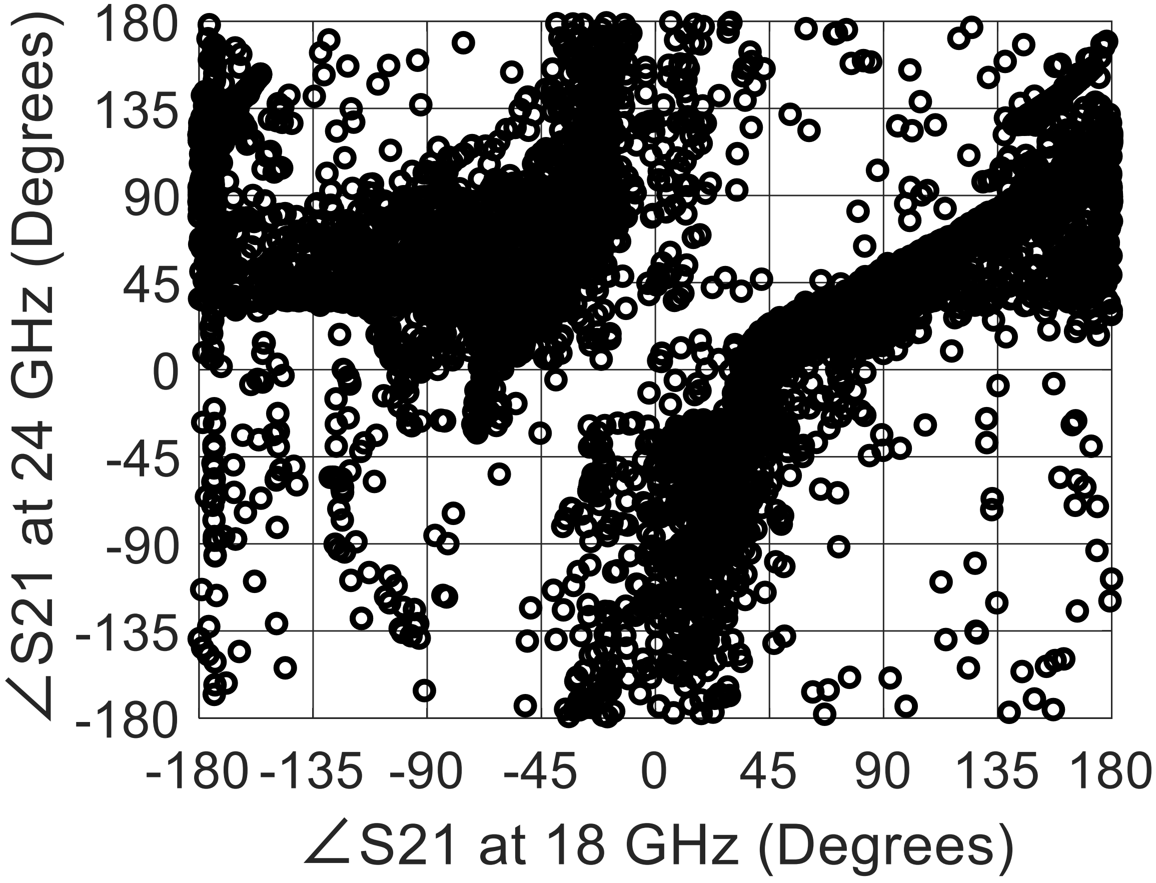

Fig.5.2-2 : Aggregate of computed $\{\mathcal{U}_e(f_a), \mathcal{U}_e(f_b)\}$ pairs for the different various dual-band transmission pair sets mentioned in Section 5.2.1. These were all for $f_a = 18\,\text{GHz}$ and $f_b = 24\,\text{GHz}$.

5.3 OUTCOMES OF AN EXAMPLE DUAL-BAND ELEMENT SYNTHESIS

5.3.1 Goals

The objective was demonstrate use of the customized shaping-process/objective-function "plug-ins" from Section 5.2 to build a database of shaped 3-layer-elements for operation at $f_a = 18\,\text{GHz}$ and $f_b = 24\,\text{GHz}$. The layer substrates have $\varepsilon_r = 2.2$ and thickness $h = 0.508\text{mm (20 mils)}$. The lattice is square, with cell sizes $d_x = d_y = 4.2\,\text{mm}$ per side. The thickness of each spacer separating the three layers is $d_1 = d_2 = 3.125\,\text{mm}$. At 24 GHz this means $d_1 = d_2 = 0.25\lambda_o$ and $d_x = d_y = \lambda_o / 3$, whereas at 18 GHz we have $d_1 = d_2 = 0.1875\lambda_o$ and $d_x = d_y = \lambda_o / 4$. A value $N_\Delta = 448$ was selected, irrespective of the value of Λ_{fill}. This ensures that, at 24 GHz, the triangles have edge lengths less than $\lambda_o / 35$, and at 18 GHz even a smaller fraction of the wavelength. Rotational symmetry was enforced[72], and hence the shape chromosome length was $N_{bit} = 112$. With $N_\Delta = 448$ there are roughly 1300 expansion functions.

In order to select a specific set of transmission phase pairs at the two frequencies, the phases were determined for a transmitarray with a quantized[73] 2-bit aperture phase distribution[74] over an aperture of diameter $D = 187.5\,\text{mm}$, to have a pencil beam at the each of the two frequencies. However, we purposefully selected different nominal focal lengths, $F_{18} = 143.25\,\text{mm}$ (and hence $F_{18} / D = 0.764$) and $F_{24} = 168.19\,\text{mm}$ (and hence $F_{24} / D = 0.897$) respectively, in an effort to ensure some independence between the paired sets $\{\mathcal{U}(18)\}$ and $\{\mathcal{U}(24)\}$. The result is a transmitarray design requiring $N_e = 14$ dual-band elements. The total number of elements within the circular aperture is 1509.

The ‘Type#4’ objective function given by expression (5.2-4), along with the condition on the cross-polarization describe din the paragraph following that expression, was used, with $m = 3$ and $n = 2$. Initial trial runs revealed that weights $\text{w}_1 = \text{w}_2 = 1$ are suitable.

5.3.2 Comments on the Computed 3-Layer Dual-Band Element Properties

There is little sense in cataloguing all the elements. Instead we have selected two examples, requiring transmission phases[75] $(-90^\circ, +90^\circ)$ and $(+90^\circ, -90^\circ)$, respectively. Fig.5.3-1 and Fig.5.3-2 reveal an element that is almost transparent over the complete frequency range between 18 GHz and 24 GHz. Fig.5.3-3 and Fig.5.3-4 show the transmission performance for the second example. It is immediately clear that it is a completely different type of element than the first example. It has achieved (within the allowed tolerance) the required transmission phase that we demanded at each

---

[72] For reasons given in Section 5.2.2.
[73] As mentioned in Section 2.4.
[74] That is quadrantally symmetric.
[75] The first number in the brackets is the transmission phase required at 18GHz, and the second that at 24GHz.

of the two frequencies. However, between the 18 GHz and 24 GHz points it has a very low transmission magnitude – indeed it becomes reflective. It has not even attempted to oblige us with a high transmission magnitude at the in-between frequencies because we have defined F_{obj} only at $f_a = 18GHz$ and $f_a = 24GHz$. The objective function only "sees" what we allow it to. The shape synthesis allows elements to be crafted for dual-band operation in which for which independently prescribed transmission phases are achieved at two separated frequencies.

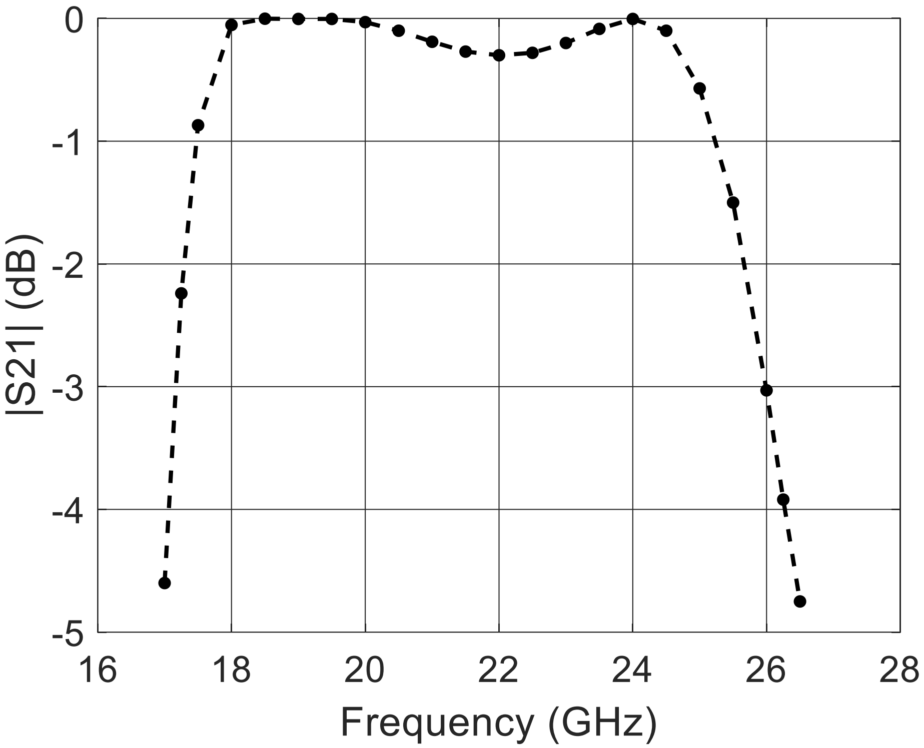

Fig.5.3-1 : Transmission magnitude versus frequency for 1st dual-band element example.

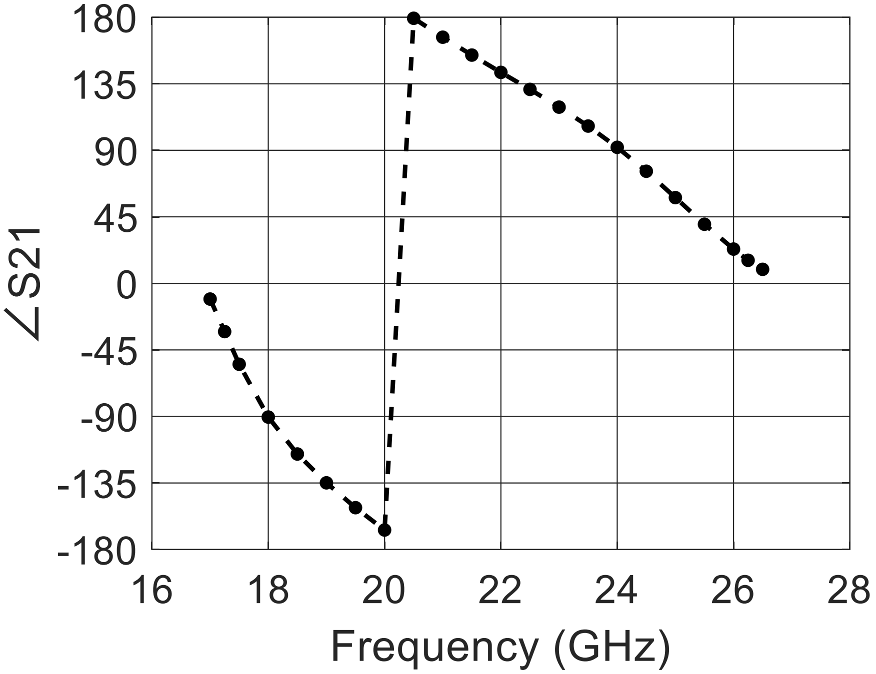

Fig.5.3-2 : Transmission phase versus frequency for 1st dual-band element example.

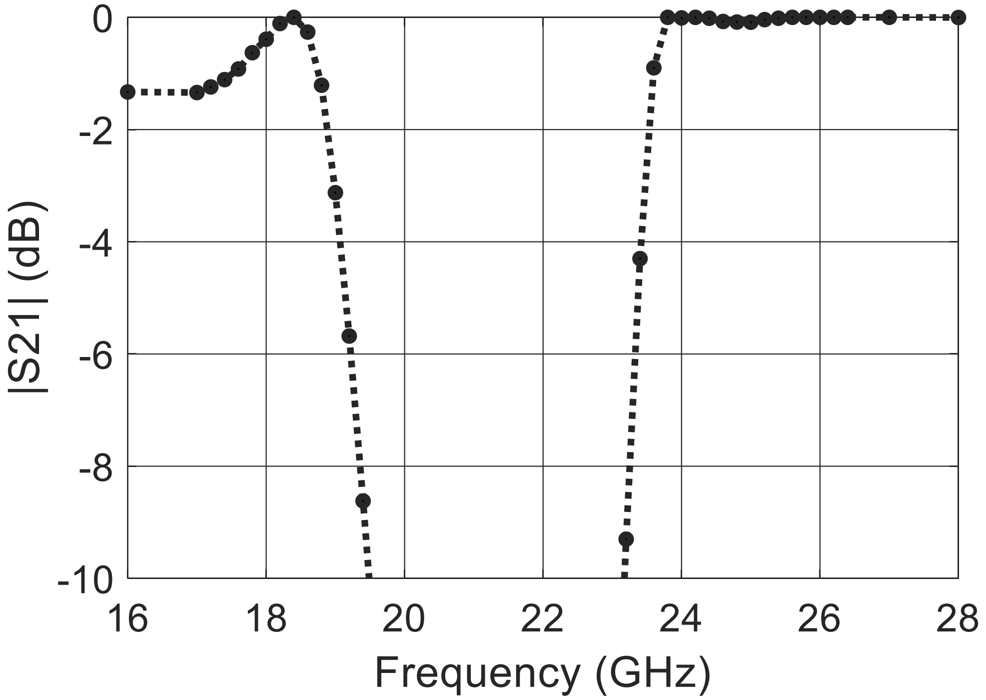

Fig.5.3-3 : Transmission magnitude versus frequency for 2nd dual-band element example.

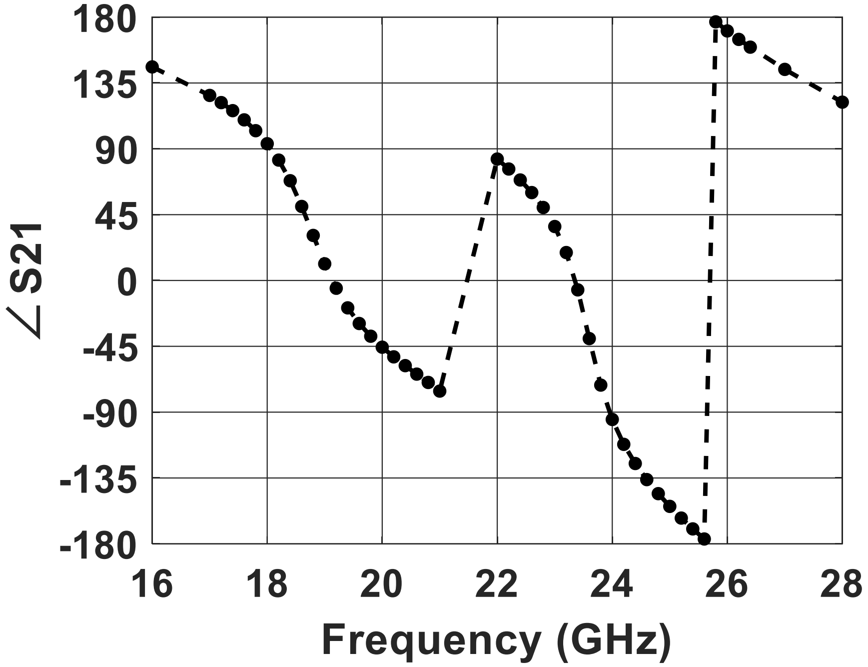

Fig.5.3-4 : Transmission phase versus frequency for 2nd dual-band element example.

5.3.3 Examination of the Shapes of Some Layers

It is instructive to examine the shapes[76] of some of the element layers in the context of conventional elements that have been reported in the literature. Fig.5.3-5 and Fig.5.3-6 show the shapes of selected layers of some 3-layer elements[77]. Fig.5.3-5(a) is fully symmetrical even though only rotational symmetry was demanded. Fig.5.3-5(c) reminds one of the Malta-cross shape used by other authors, except that the arms are not joined at the centre of the element. Fig.5.3-6(c) is virtually a patch shape [GAGN 13], except for shaping along its periphery. Fig.5.3-6(f) is like a square loop [RYAN 10], again with some 'tuning' introduced by the shaping process. The remainder of the elements shown are reminiscent of the spiral dipole [ABDE 14] and doubly bent spiral dipole [HSU 18], but with perturbations of the arms of such elements, and loading at the ends of these arms. Those authors found that that particular rotationally symmetric shape (i.e. spiral dipole) produced low cross-polarization. As mentioned in Section 5.2.2, this is not so with all

---

[76] We note that they are quite different from the single-band examples shown in Table 4.4-1; it should be recalled that in the single-band shape synthesis full symmetry was enforced (but of course need not have been).

[77] These are in fact magnified photos of layers of fabricated dual-band elements that are further discussed in Chapter 6. The shaping controller is able to display such element shapes by exploiting the graphics capability of the CEM engine.

rotationally symmetric shapes. The shape synthesis process has in essence “discovered” what is important in a rotationally symmetric layer to ensure this, and has then perturbed the basic shape to achieve the phases demanded at the two separate frequencies. Fig.5.3-6(g) and (h), which each show two adjacent elements, have been shown to illustrate that not all elements occupy the same portion of a unit cell.

5.4 CONCLUDING REMARKS

In order to exercise the shape synthesis approach for cases more general than that in Chapter 4 we here used it to obtain 3-layer elements that provide independent sets of transmission phases at two separated frequencies. Obtaining such dual-band transmitarray elements with independently specified transmission phases has not been possible without performing a shape synthesis. It was discovered that full sets of dual-band transmission phase pairs is not always possible if full-symmetry is demanded of the elements. This requirement was relaxed to that of rotational symmetry. The latter elements can generate cross-polarized fields that are unacceptably high, but it was demonstrated that by incorporating a polarization check in the objective function such geometries can be excluded. Thus the dual-band 3-layer transmitarray elements could be synthesized by customizing the shaping process and objective function as new “plug-ins” to the shaping controller.

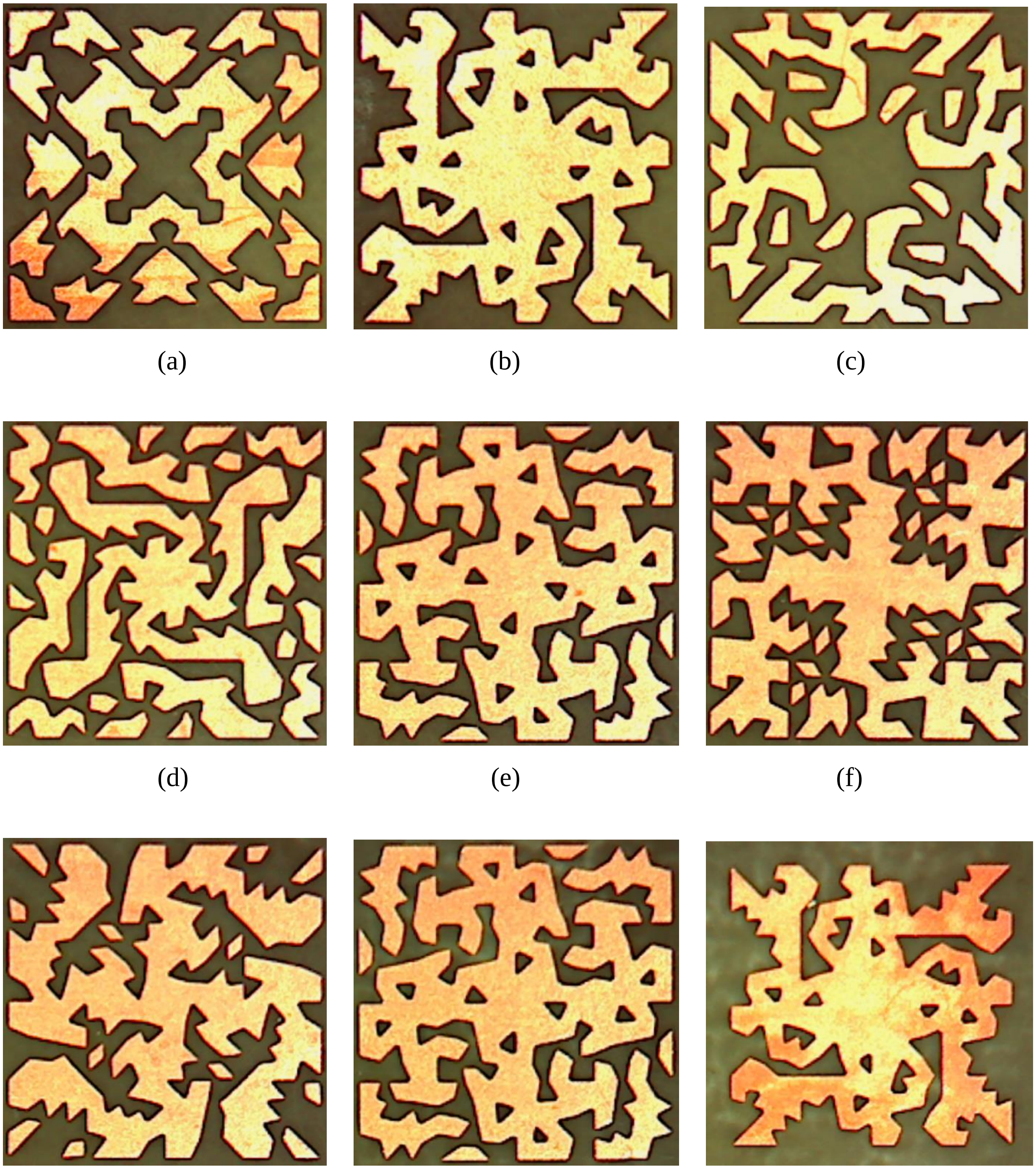

(a) (b) (c)

(d) (e) (f)

(g) (h) (i)

Fig.5.3-5 : Magnified Images of Selected Dual-Band 3-Layer Element Layers.

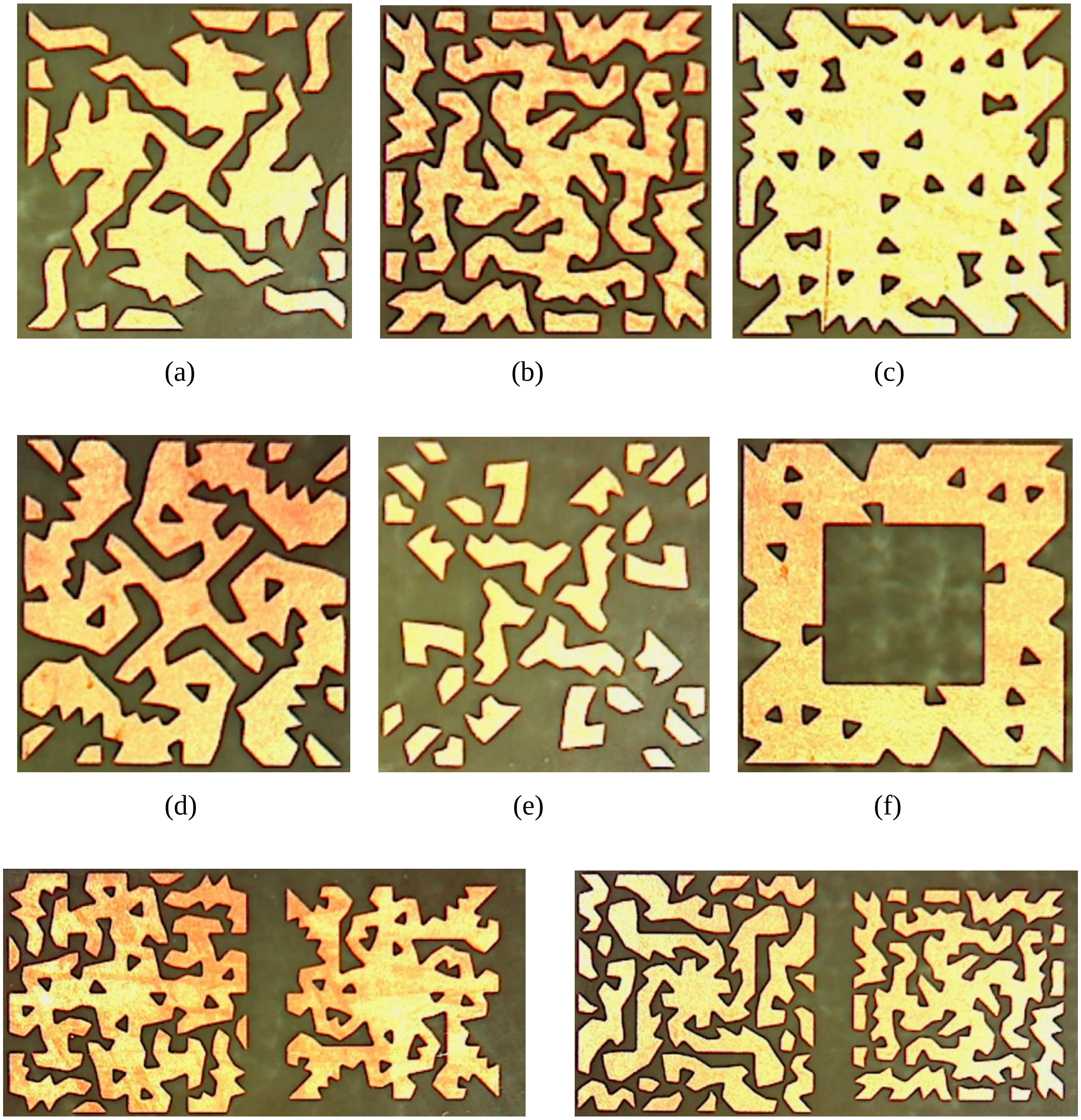

(a) (b) (c)

(d) (e) (f)

(g) (h)

Fig.5.3-6 : Additional Magnified Images of Selected Dual-Band 3-Layer Element Layers.

CHAPTER 6

Experimental Investigation of the Transmitarray Designed Using Shape-Synthesized Dual-Band Elements

6.1 PRELIMINARY REMARKS

The transmitarray realization discussed here is merely a means to an end - its purpose is to allow us to demonstrate experimentally that the development of the element shape synthesis approach and associated shaping tools, which was the goal of this thesis, has been achieved. Section 6.2 furnishes the structural geometry of the particular design, for which the required element transmission phase pairs for the dual-band frequencies can be determined as indicated in Section 2.4. Dual-band 3-layer elements with these transmission phases have already been determined in Section 5.3. Some technical details of the fabrication and assembly process are supplied in Section 6.3. The detailed experimental investigation is described in Section 6.4. The chapter is concluded by Section 6.5.

6.2 DUAL-BAND TRANSMITARRAY DESIGN

We wished to experimentally investigate the effectiveness of the shape synthesis procedure in achieving the correct transmission phases, and how they worked *in situ*, in the presence of the fabrication/assembly imperfections that inevitably arise. We therefore implemented the case discussed in Section 5.3. The gaol was not the development of some “best so far” transmitarray, but rather the realization of some transmitarray to allow experimental validation of the element shape synthesis process. With reference to Fig.6.2-1, the values of the subtended angles are $\theta_e = 33^\circ$ for a feed located at focal point F_{18} and $\theta_e = 29^\circ$ for a feed located at focal point F_{24}. A portion of the top layer of the elements over one quadrant of the transmitarray is shown in Fig.6.2-2; some of these element shapes have already been shown in Fig.5.3-5 and Fig.5.3-6.

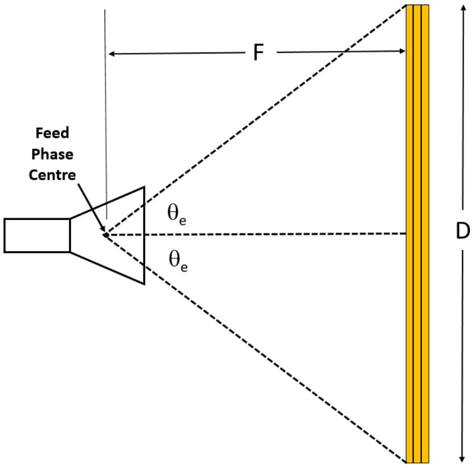

Fig.6.2-1 : Geometry of the selected transmitarray design. The feed horn and transmitarray are not drawn to scale.

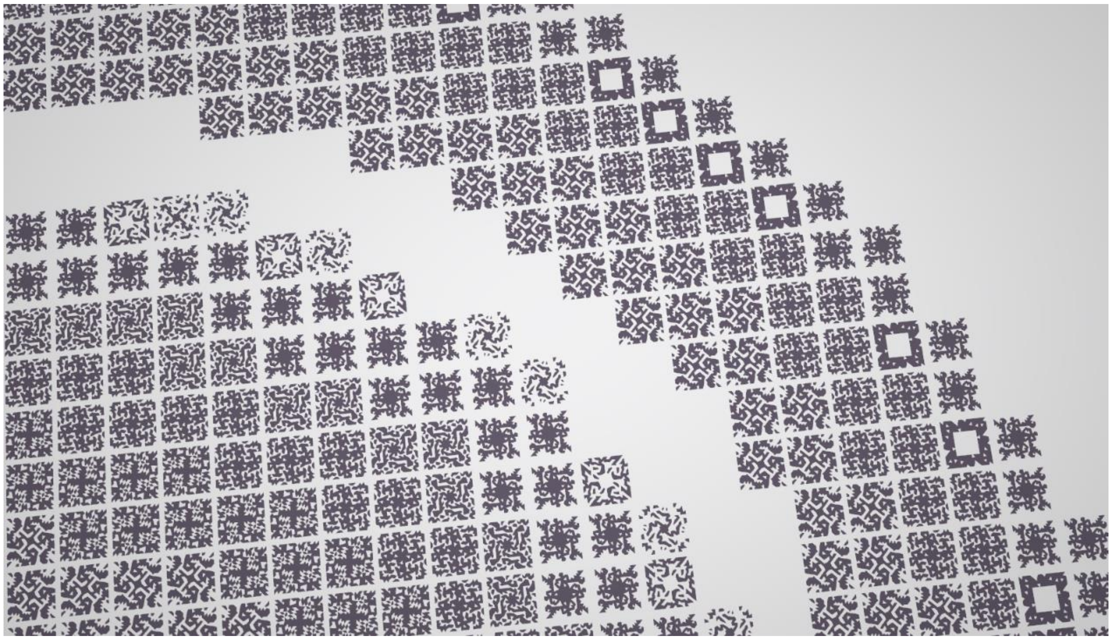

Fig.6.2-2 : Portion of one of the layers of the designed transmitarray, displayed using graphics accessed by the shaping controller. Details can be perceived by zooming in to the diagram[78].

---

[78] Referring back to the discussion in Section 5.3.3, where similarity of the shaped elements to more conventional shapes was discussed. Zooming in on the electronic copy of this figure gives a clearer picture of the element details; photos of the actual etched element layers are provided in Appendix D.

6.3 DUAL-BAND TRANSMITARRAY FABRICATION & ASSEMBLY

The substrate is Rogers RT/duroid 5880, which has $\varepsilon_r = 2.2$, $0.0004 < \tan\delta < 0.0009$, and $h = 0.508\text{mm (20 mils)}$. The spacer material is ROHACELL® HF, whose properties are tabulated in Appendix C; all spacers are of thickness 3.1mm. The constituent parts of the transmitarray are shown in Fig.6.3-1. The shaping controller used the graphics/drafting capabilities of the CEM engine to capture the geometry of each of the three constituent layers for every 3-layer element required in the transmitarray, and generate a layout file[79] of each layer of the complete transmitarray in a format compatible with the fabrication process[80]. The three fabricated constituent layers are shown in Appendix C. Four 1.65mm diameter holes were drilled in each layer board while the board was still in the same fixture as that with respect to which the etching process is controlled, as depicted[81] in Fig.6.3-2. This meant that the holes were accurately referenced to the centre of the circular region containing the conducting elements, to which the conducting elements themselves were referenced. During assembly of the 3-layer transmitarray structure alignment pins were passed though these holes from layer to layer (and of course through the Rohacell spacers) to ensure that there is the correct cell-alignment from layer to layer. In addition, the whole transmitarray structure fitted snugly into a dielectric frame of the same outer dimensions as the rectangular-shaped transmitarray structure. This is evident from Fig.6.3-3. In order to minimise bowing of the transmitarray layers, rigid planar free-space foam layers were placed flush with the input and output faces of the transmitarray. These are not shown in Fig.6.3-3 since they obscure the actual transmitarray (albeit only optically). The transmitarray mounting (that includes the frame) allows the height, and axial movement, of the feed to be adjusted. This ensured that the feed is centred on the transmitarray, and also allowed its axial position to be adjusted so that the correct location of its phase centre could be ensured at both 18 GHz and 24 GHz.

As is evident from Fig.6.3-3, the feed horn is a pyramidal horn that flares from WR42 rectangular waveguide ; its details are provided in Appendix B. For the subtended angles quoted in Section 6.2 this implies feed pattern edge tapers of -10dB and -11dB at 18 GHz and 24 GHz, respectively. The

---

[79] In this case in *Gerber* format.

[80] This was done by at a commercial facility, *Metaplast Circuits*, that uses laser exposure of the substrates under control of the *Gerber* format CAD file, followed by chemical etching.

[81] The elements all fit within the circle of diameter $D = 187.5\,\text{mm}$, but the substrate is rectangular in shape, of size $220\,\text{mm} \times 220\,\text{mm}$.

horn patterns are, for the purposes of the approximate pattern analysis approach described in Section 2.5, therefore modelled by $q_f = 6$ at 18 GHz, and $q_f = 10$ at 24 GHz.

The coaxial to waveguide adapter[82] is an HP K281C with a nominal input reflection coefficient of less than -29 dB over the 18 – 26.5 GHz band when connected to a matched load.

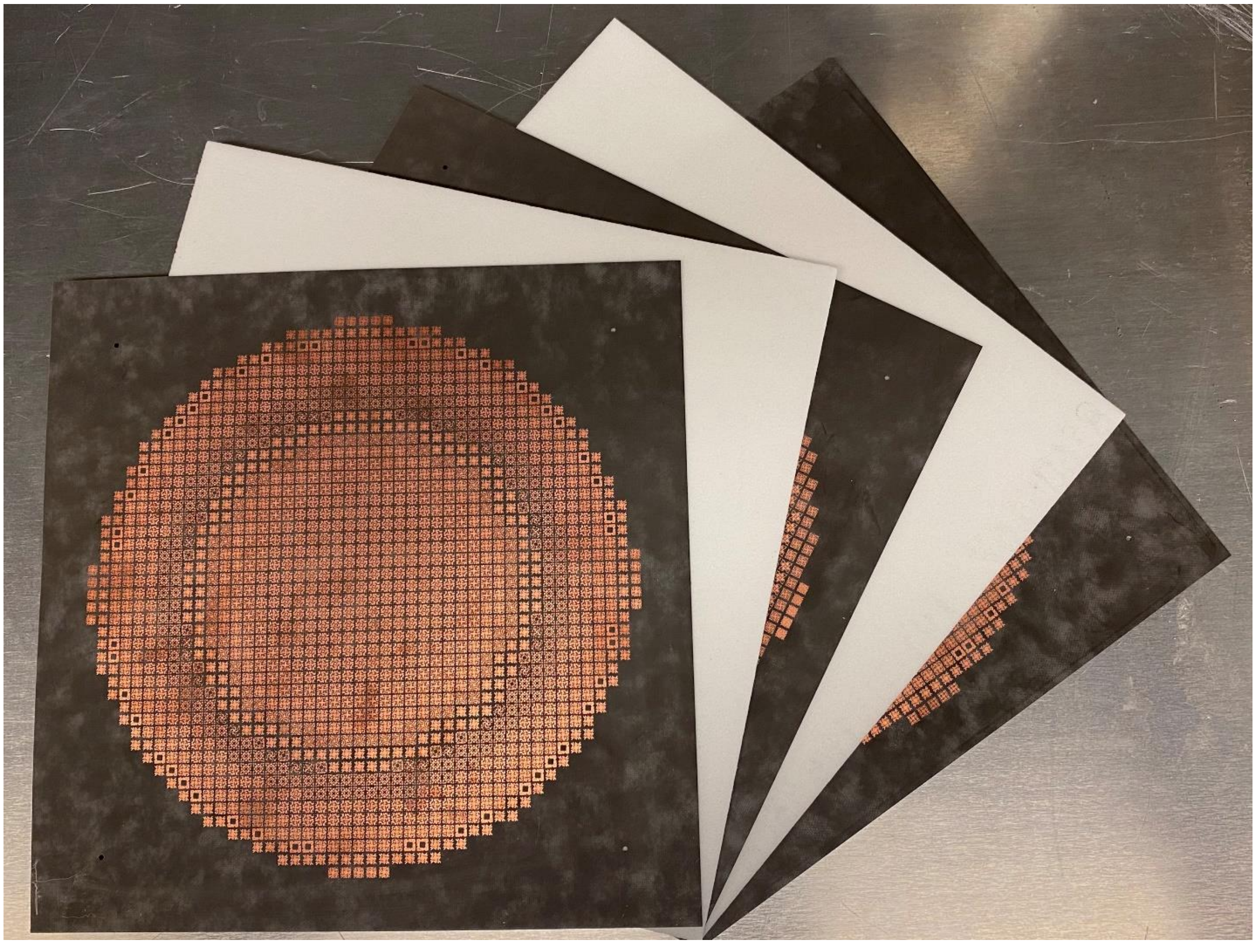

Fig.6.3-1 : Layers and spacers of the 3-layer transmitarray.

---

[82] Also evident in Fig.6.3-3.

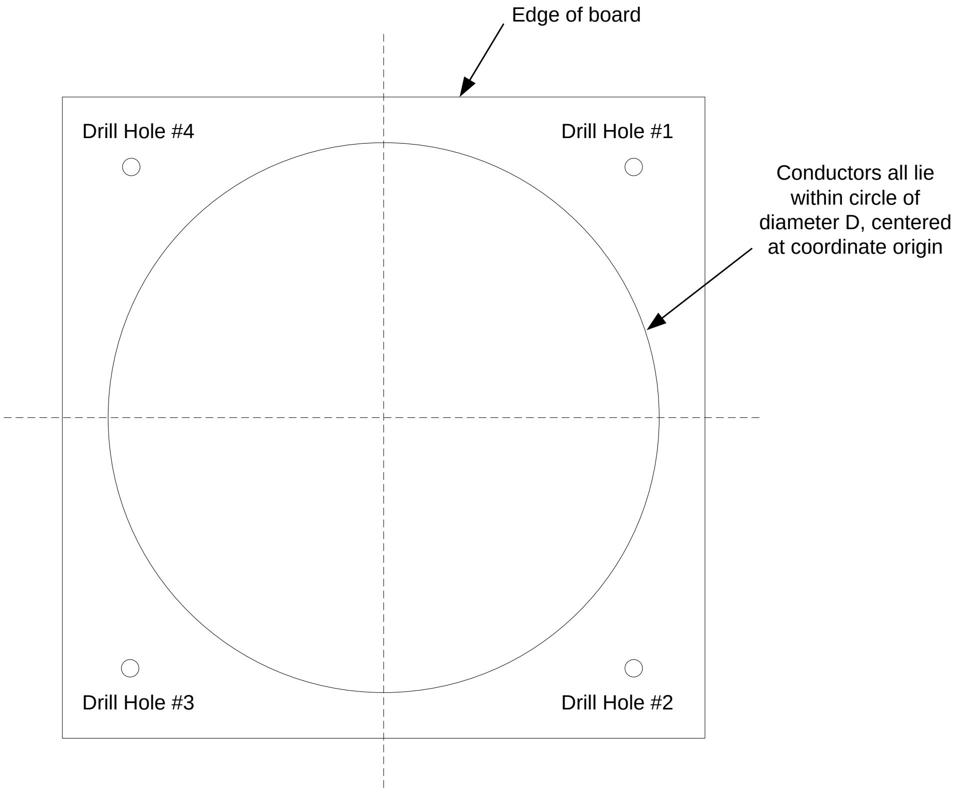

Fig.6.3-2 : Diagram for layout of the transmitarray layers.

Apart from the tolerances on the conductor dimensions and gaps, slight misalignment of the three layers, and small errors in the location of the feed, there are the thicknesses d_1 and d_2 of the foam spacers, as well as the precise value of ε_r, whose departure from their values assumed during the element shaping process could cause the measured performance to differ from that predicted. Consultation of Table C-1 in Appendix C reveals that the Rohacell HF foam has $1.041 < \varepsilon_r < 1.067$. Also, the there is a +/- 0.2mm thickness tolerance[83]. Several of the shape synthesized dual-band 3-layer elements were therefore subjected to a Monte Carlo analysis as follows : A random number generator was used (based on a uniform distribution function) to generate random values of d_1, d_2 and ε_r within the bounds $(3.125 - 0.2)\text{mm} \le d_i \le (3.125 + 0.2)\text{mm}$ and $1.041 < \varepsilon_r < 1.067$. The transmission coefficient magnitudes and phases $|S_{21}|$ and $\angle S_{21}$ of the 3-layer elements are

---

[83] Private Communication, Mr. R. Averill, Evonik Foams, Inc., 2019.

computed for the selected dual-band elements for each set of random values, at 18GHz and 24 GHz. The changes in the latter quantities were not significant.

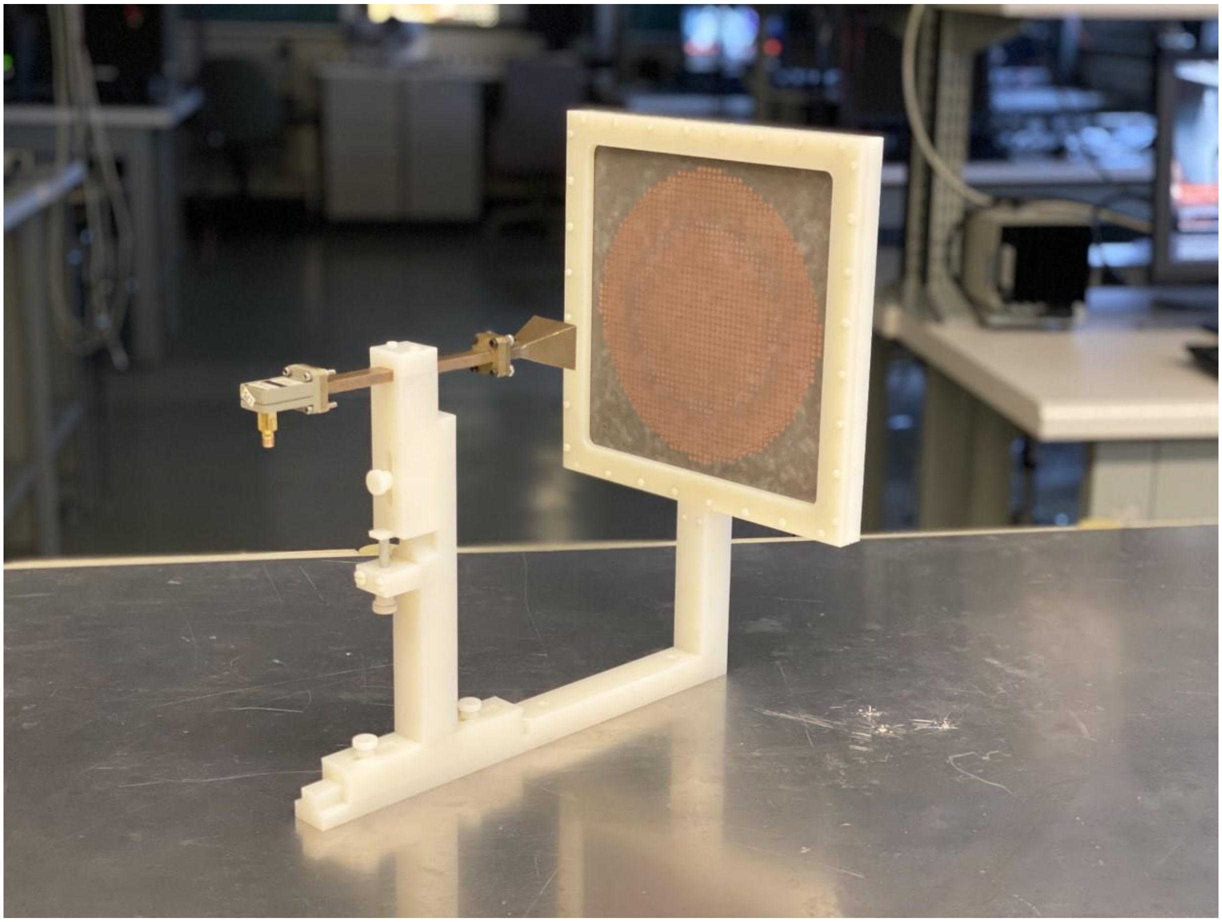

Fig.6.3-3 : Assembled transmitarray in mounting freame.

6.4 EXPERIMENTAL INVESTIGATION OF THE RADIATION PATTERNS

6.4.1 Initial Observations

The measured gain[84] of the transmitarray is plotted in Fig.6.4-1, and is found to be peaked around 17.4 GHz and 23.2GHz, indicating a frequency shift of about 3%. These gain values will be discussed later in Section 6.4.6.

---

[84] The peak gain values of the transmitarray were measured via the substitution method [PARI 14], using NSI-MI standard gain horns.

In what follows, we will several times refer to computed patterns. Unless stated to the contrary, these are found using the approximate analysis embodied in expression (2.4-8). Due to the observed frequency shift, we will usually compare computed patterns at 18 GHz and 24 GHz to measured patterns at 17.4 GHz and 23.3 GHz, respectively. We will refer to these as the 17.4/18 GHz and 23.2/24 GHz patterns, respectively.

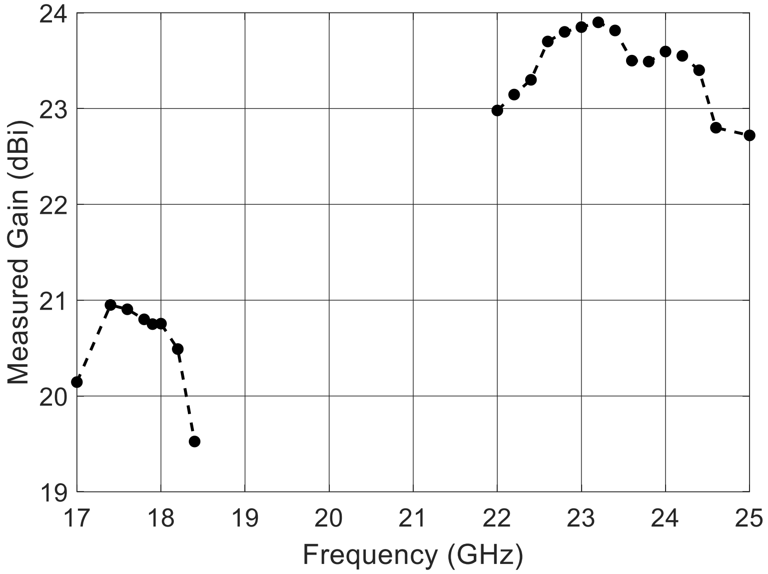

Fig.6.4-1 : Measured gain values of the 3-layer transmitarray.

6.4.2 Measured Radiation Patterns

Initially we will discuss the radiation patterns at the above-mentioned two design frequencies. Fig.6.4-2 shows the computed and measured H-plane radiation patterns at 17.4/18 GHz. These are with the feed phase centre located at the point we have called F_{18}. A similar comparison is shown in Fig.6.4-3 at 23.2/24 GHz, for the feed phase centre located at F_{24}. Several comments are in order:

■ The cross-polarized levels are low. This supports the fact that during the shaping of the elements with rotational symmetry, those with unacceptable cross-polarized output were successfully filtered out[85].

---

[85] As noted in Section 5.2.2.

■ The general form[86] of the measured main lobes of the patterns are different at the two dual-band frequencies, and are what was expected from the predictions. The predicted pattern at the lower frequency has sharply defined first-sidelobes, whereas that at the higher frequency has 'shoulders'.

■ The measured sidelobe levels of the 17.4 GHz pattern are around -12.5dB, much higher than expected. The beamwidth is narrower than expected. Similar comments as to sidelobe levels apply to the measured pattern at 23.2 GHz. The reasons for the discrepancies between the computed and measured patterns must next be carefully examined.

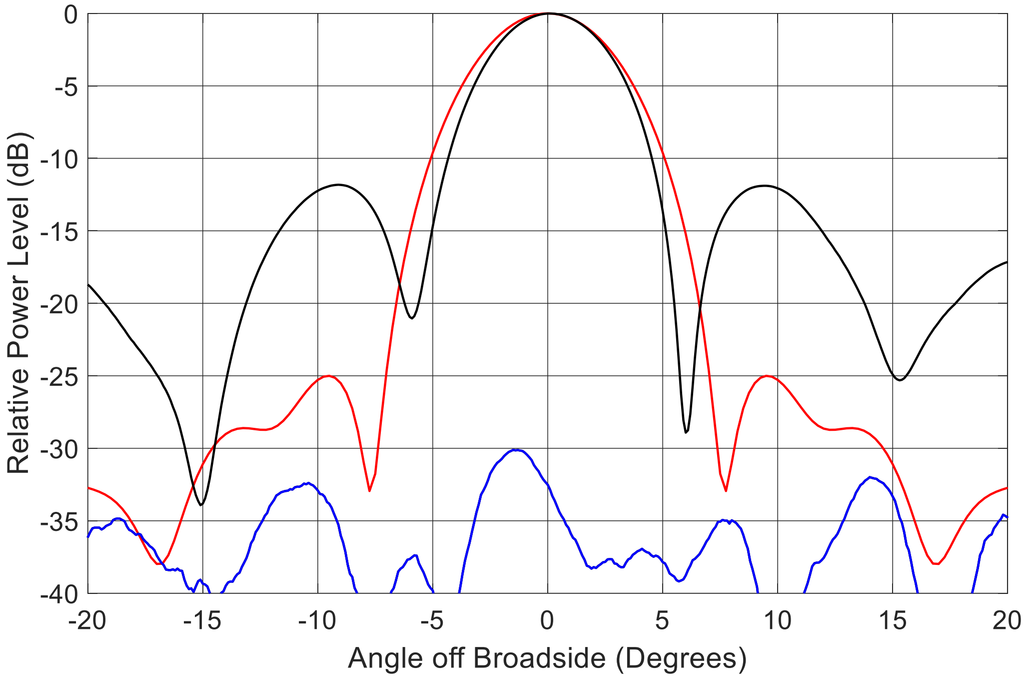

Fig.6.4-2 : Computed (red) and measured (black) H-plane ($\phi = 0^\circ$) co-polar radiation patterns, and measured (blue) cross-polar pattern at the lower frequency. Measured patterns are at 17.4 GHz and computed patterns at 18 GHz.

---

[86] The sidelobe level discrepancies will be discussed shortly.

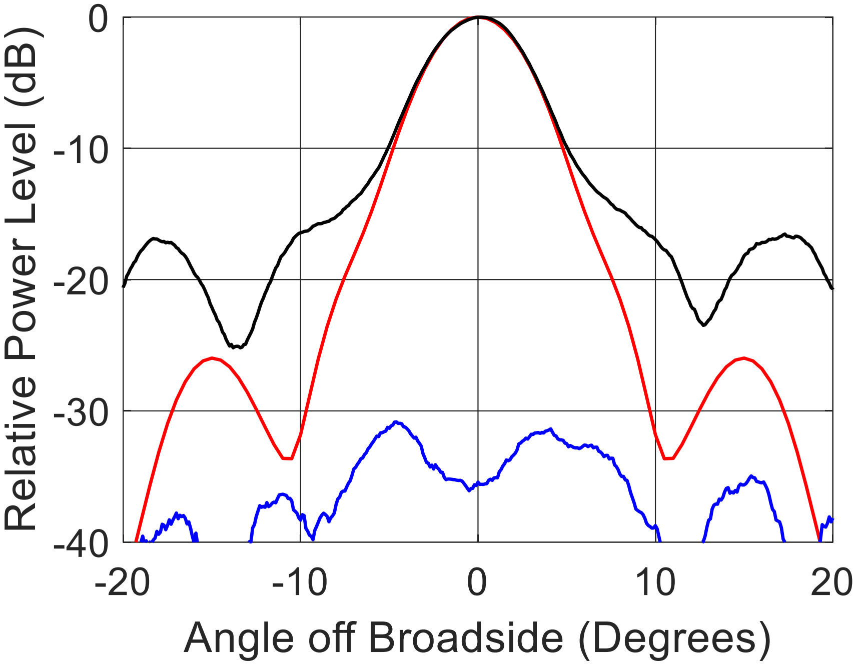

Fig.6.4-3 : Computed (red) and measured (black) co-polarized H-plane ($\phi = 0^\circ$) co-polar radiation patterns, and measured (blue) cross-polar pattern at the higher frequency. Measured patterns are at 23.2GHz and computed patterns at at 24 GHz.

6.4.3 Diagnosis of Reasons for the Radiation Pattern Discrepancies

Aperture antenna theory [STUT 13] informs us that the situation in Fig.6.4-2, namely a higher sidelobe level and narrower beamwidth than we were expecting, can occur if the amplitude distribution over an aperture is uniform. In the present situation this is unlikely the reason, because even if the feed pattern were very broad, there is the inherent taper mentioned in Section 2.4.

It is known that a non-uniform amplitude distribution that has edge-brightening[87] is subject to such sidelobe level increases, along with a narrowing of the main lobe (the latter being apparent from Fig.6.4-2). In the case of a reflectarray, aperture blockage by the feed could be suspected. In the present transmitarray case there is no such blockage. Any unwanted variation of the amplitude distribution over the aperture must be due to back-reflections from the elements due to incorrect transmission amplitudes of these elements, as well as incorrect transmission phases. This in turn would mean that the backlobe of the transmitarray would be high. Fig.6.4-4 shows the measured[88] complete 360° H-plane pattern at 17.4 GHz, and Fig.6.4-5 that at 23.2 GHz. It is clear that there are

---

[87] One for which the amplitude distribution is higher at the edges of the aperture than at the centre, as noted in [MAIL 94] in the context of Dolph-Chebyshev array distriburtions.

[88] The computed curves shown in red, in these figures, will be discussed shortly.

indeed very high backlobes. It would appear that the transmission magnitudes of the shaped elements are not as expected. Similar observations can be made for the backlobe at 23.2 GHz, as shown in Fig.6.4-5. Reasons for this will be investigated further in what follows.

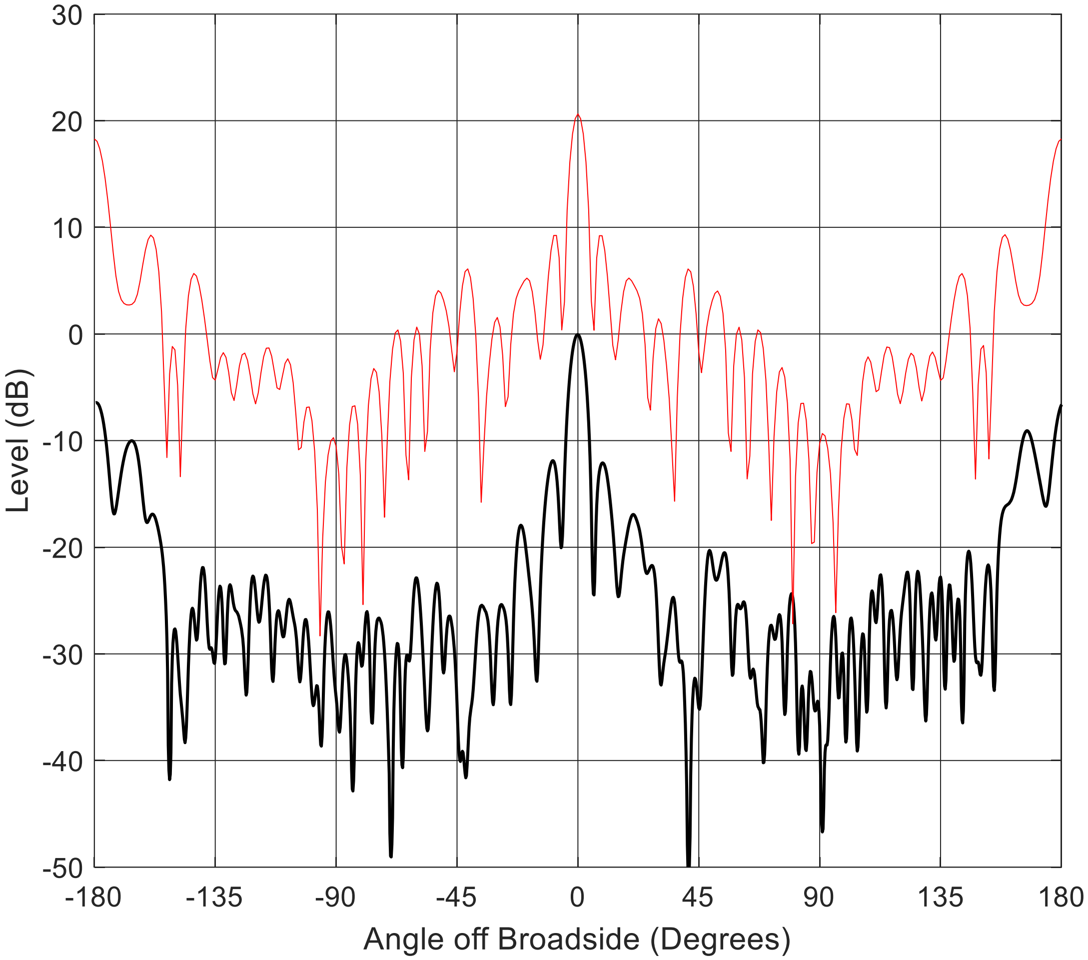

Fig.6.4-4 : Measured (black) normalized H-plane co-polar radiation pattern (in dB) over a full 360° cut, at 17.4 GHz. The gain pattern (in dBi) computed using 3D HFSS model is shown in red, with its peak 20.8 dBi.

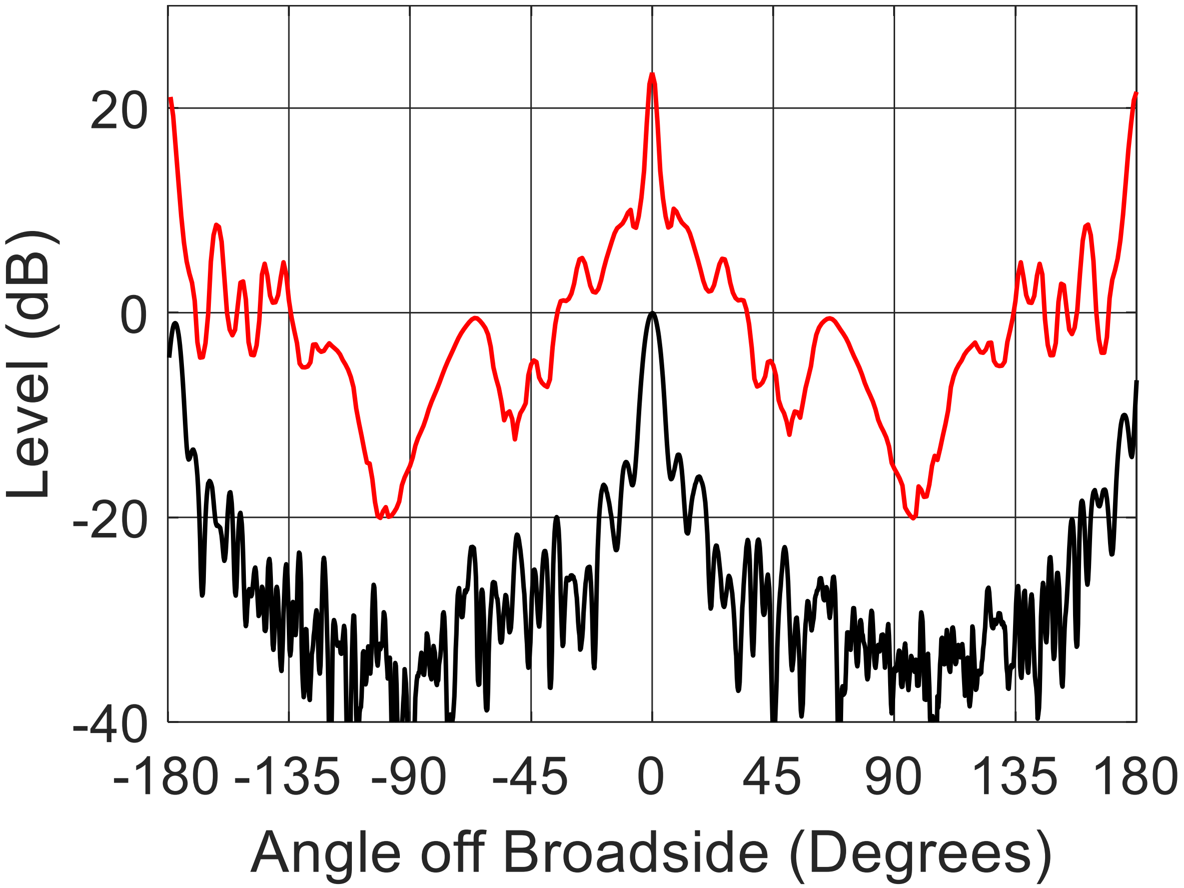

Fig.6.4-5: Measured (black) normalized H-plane co-polar radiation pattern (in dB) over a full 360° cut, at 23.2 GHz. The gain pattern (in dBi) computed using 3D HFSS model is shown in red, with its peak 23.6 dBi.

Before proceeding we briefly note that the placing of absorber over the frame[89] supporting the transmitarray did not remove the backlobes. Also, the backlobe level was observed at all frequencies in the vicinity of 17.4 GHz and 23.2 GHz , and found to vary only slightly. In other words it does not occur only at some isolated frequency and not at others. The feed antenna pattern was also measured with the frame present but the transmitarray absent; backlobes do not occur. Thus the backlobes are indeed due to the transmitarray elements themselves.

The geometry files of each transmitarray layer, generated using the shaping controller for transmitarray fabrication purposes, were employed to set up a complete 3D model of the

---

[89] The rectangular supporting frame in Fig.6.3-3.

transmitarray in the commercial computational electromagnetics code HFSS[90]. The 3D full-wave gain[91] pattern performance obtained in this way is shown as the red curves in Fig.6.4-4 and Fig.6.4-5. The backlobes[92] are immediately observed, conforming the suspicions that these are due to the misbehaviour of the elements themselves.

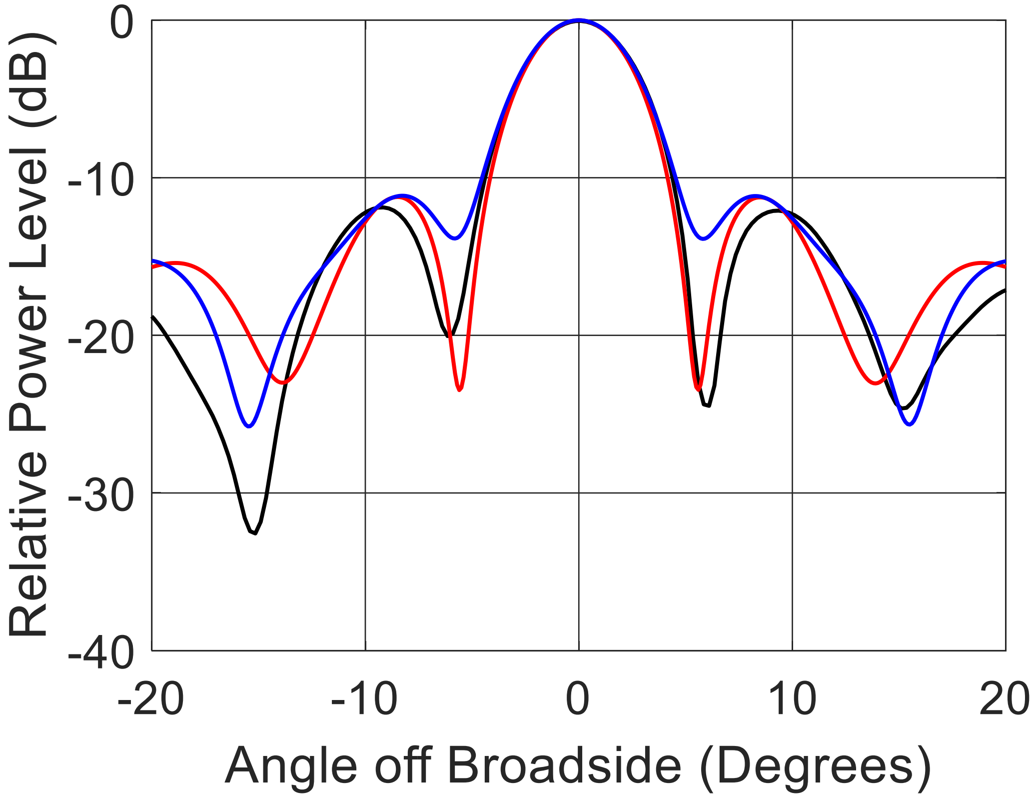

Fig.6.4-6 : Computed H-plane (red) and E-plane (blue) radiation patterns from the full-wave 3D model of the complete 3-layer transmitarray plus feed, using HFSS. The measured H-plane radiation pattern is shown in black. All patterns at 17.4 GHz.

Fig.6.4-6, a close-up of a portion of Fig.6.4-4 around the main lobe, reveals that good agreement between the 3D full-wave simulation and the measurements; similar remarks can be made for the higher frequency. Thus, disappointing as the resultant patterns are from a transmitarray antenna point of view, this agreement confirms that the transmitarray has been correctly fabricated, and the

---

[90] Some specifics of the model are provided in Appendix E.

[91] Losses have been included in the 3D HFSS model.

[92] The directivity computed using this full-wave 3D model will be considered in Section 6.4.6.

pattern measurements reliable. The prediction of the individual element properties during shaping are to blame.

6.4.4 Investigation of the Predicted Transmitarray Element Properties

The task at hand was to determine the reason the 3-layer shaped element properties were apparently not their predicted values.

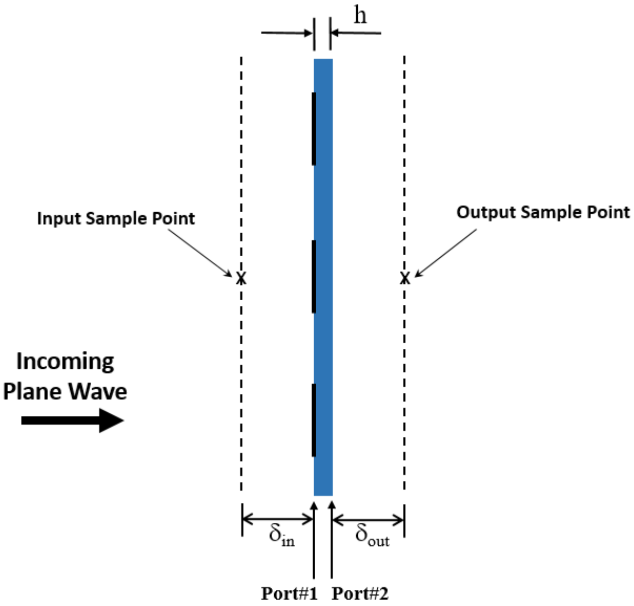

Fig.6.4-7 : Diagram of a single periodic structure layer of identical cells. The distances δ_{in} and δ_{out} are shown exaggerated.

We refer to Fig.6.4-7. It was found that the CEM engine always references[93] the phase of the reflection and transmission coefficients to Port#1, whereas in order to apply the mixed full-wave/equivalent circuit modelling of a 3-layer element as in Section 4.2, the phase of the transmission coefficient must be referenced to Port#2. In other words, the scattering parameters need to be defined in terms of the plane wave fields as

$$S_{11} = \frac{E_{\text{co}}^{\text{total}}(Port\,\#1) - E_{\text{co}}^{\text{incident}}(Port\,\#1)}{E_{\text{co}}^{\text{incident}}(Port\,\#1)} \tag{6.4-1}$$

And

---

[93] And this is not easily altered.

$$S_{21} = \frac{E_{\text{co}}^{\text{total}}(Port\,\#2)}{E_{\text{co}}^{\text{incident}}(Port\,\#1)} \tag{6.4-2}$$

The ABCD matrices to be used in the mixed full-wave/equivalent-circuit matrix of Section 4.2 to determine the 3-layer element properties must be found from the plane wave S-parameters as defined in (6.4-1) and (6.4-2). This appears only possible using the CEM engine if the plane wave fields appearing in the above expressions are extracted[94] and then the said expressions simply evaluated.

If there are no conducting shapes on the substrate then the field quantities in (6.4-1) and (6.4-2) can be evaluated for the infinite 'periodic' structure right at Port#1 and Port#2 ; we can use $\delta_{\text{in}} = \delta_{\text{out}} = 0$. Results for such a case have been checked against the analytical results for plane wave scattering from an infinitely large dielectric layer of finite thickness and found to be correct.

However, as in most cases, when there are conducting shapes present in each cell of the periodic structure, the fields at Port#1 and Port#2 are not the pure plane wave fields whose transmission and reflection coefficients we desire. They contain evanescent higher-order Floquet mode field components. For instance, in the full-wave analysis used here, the incident plane wave field is x-polarized. However, in the vicinity of the layer there are y- and z-components[95], the z-component being normal to the layer. But these full-wave computations also confirm that higher-order fields rapidly decrease in amplitude with distance from the layer. Some of the y-component (the cross-polarized component) survives on either side of the layer as a plane wave field, but it is[96] three orders of magnitude lower than the cross-polarized one for reasons given in Section 3.9.2 and Section 5.2.2. Therefore, instead of using (6.4-1) and (6.4-2) directly, one needs to extract from the single-layer full-wave solution the fields at the locations (to the left and right of the two ports) indicated in

$$S_{11} = \frac{E_{\text{co}}^{\text{total}}(Port\,\#1-\delta_{in}) - E_{\text{co}}^{\text{incident}}(Port\,\#1-\delta_{in})}{E_{\text{co}}^{\text{incident}}(Port\,\#1-\delta_{in})} \tag{6.4-3}$$

and

$$S_{21} = \frac{E_{\text{co}}^{\text{total}}(Port\,\#2+\delta_{out})}{E_{\text{co}}^{\text{incident}}(Port\,\#1-\delta_{in})} \tag{6.4-4}$$

---

[94] This is fortunately possible without effort.

[95] The coordinate system follows that shown in Fig.3.9-1.

[96] For the conductor shapes in use here.

The distances δ_{in} and δ_{out} are selected so that the fields sampled are the remnant propagating plane wave fields only[97]. The S-parameters are computed as in (6.4-3) and (6.4-4), and their the reference planes are moved to the Port#1 and Port#2 locations using multiplicative phase factors $e^{j2k_0\delta_{\text{in}}}$ and $e^{jk_0\delta_{\text{in}}}e^{jk_0\delta_{\text{out}}}$, respectively, as in [POZA 12, Sect.5.4].

This corrected approach to extracting the single-layer scattering parameters, and hence ABCD matrices, was used to re-calculate the complex transmission coefficients of a selection of the dual-band shape synthesized elements. These were compared to full-wave results for the complete selected 3-layer elements, obtained using the CEM engine. The latter used the same concept embedded in (6.4-3) and (6.4-4), but for the 3-layer arrangement results as depicted in Fig.6.4-8. The sets of results were almost indistinguishable. Unfortunately the corrected transmission amplitudes of some of the centrally-located elements were much lower (< -6dB) than previously (but incorrectly) predicted while they were being shaped; the result is more reflection and hence higher backlobes. Thus the shape synthesis approach is accurate, and the mixed full-wave/equivalent-circuit 3-layer prediction used during the shaping process redeemed.

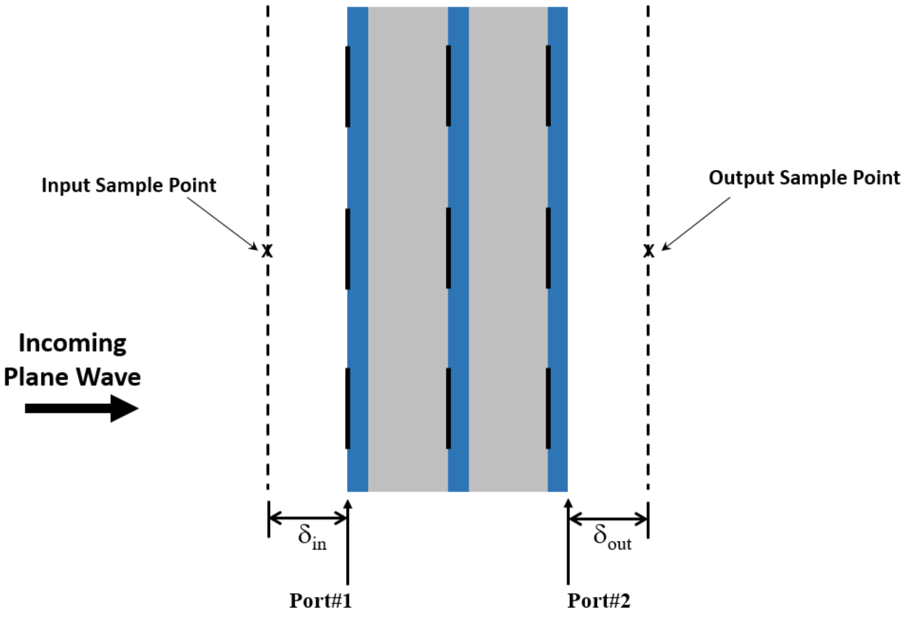

Fig.6.4-8 : Diagram of a 3-layer periodic structure identical elements. The distances δ_{in} and δ_{out} are shown exaggerated.

---

[97] No higher-order Floquet mode fields.

6.4.5 Computed Radiation Patterns Using Adjusted Transmission Amplitudes and Phases

The re-computed transmission properties from Section 6.4.4 for each element used in the fabricated transmitarrray were next used in the approximate radiation pattern analysis expression (2.4-8). The results are now 're-compared' to the measured patterns[98] in Fig.6.4-9 and Fig.6.4-10. We do not expect the computed patterns to have the same level of agreement as that with those obtained via the full-wave HFSS model in Fig.6.4-6, for instance, because the computed patterns shown are those found via the approximate method. The observation from these two figures is as follows : Using the corrected transmission coefficients found using the full-wave/equivalent-circuit approach (needed in the shaping process[99]), we would have expected the higher sidelobes and narrower beamwidths found in Section 6.4.2. These elements would not have been considered acceptable.

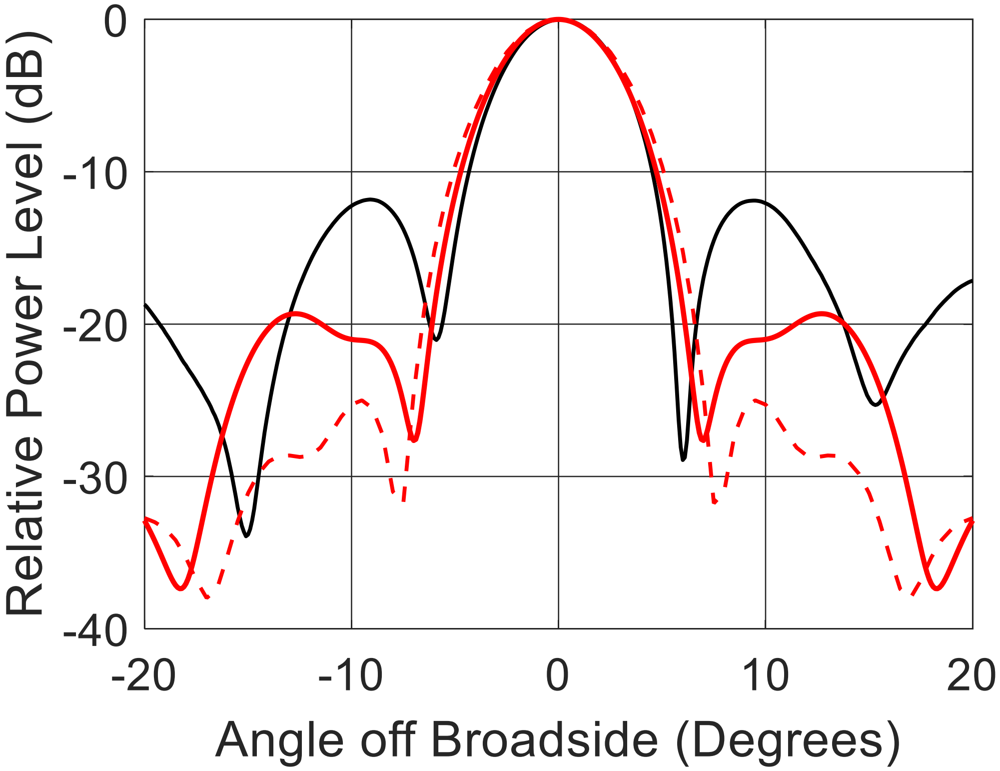

Fig.6.4-9 : Re-computed (solid red) and measured (black) H-plane ($\phi = 0^{\circ}$) co-polar radiation patterns, at 17.4 GHz. The dashed red line is the computed pattern shown in Fig.6.4-2.

---

[98] We write 're-compared' because a similar comparison was done earlier in Fig.6.4-2 and Fig.6.4-3. We do not expect the computed patterns to have the same level of agreement as that with the computed ones (obtained via the full-wave HFSS model) in Fig.6.4-6, for instances, because the patterns here are those found via the approximate method.

[99] Section 4.2.

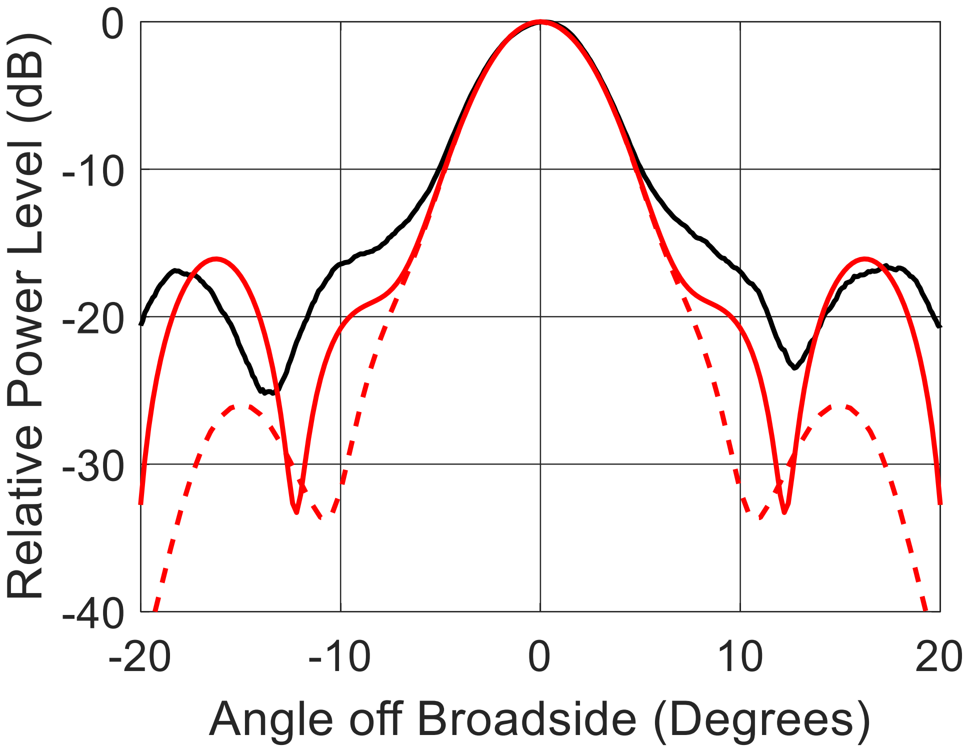

Fig.6.4-10: Re-computed (red) and measured (black) H-plane ($\phi = 0^\circ$) co-polar radiation patterns, at 24 GHz. The dashed red line is the computed pattern shown in Fig.6.4-3.

6.4.6 Reconsideration of the Measured and Computed Gain

We next return to the issue of the measured gain[100] of the transmitarray shown in Fig.6.4-1. The measured gain is much lower than expected; the reason is the incorrect element transmission coefficient values discussed earlier. In order to gauge (albeit approximately) the effect of the high backlobes on the directivity, we obtained an estimate of the directivity by assuming we have the patterns of Figs.6.4-4 and 6.4-5 in all pattern cuts[101]. We then use these to compute an estimated

---

[100] It has been pointed out to us that it is fortuitous that a far-field test range was used. If the gain of an AUT is measured on a planar near-field (PNF) test range, the assumption is that all significant energy is actually captured by the PNF scanner, and other radiation is ignored. If back radiation is very small this is not a problem, and the measured AUT gain errs only slightly on the high side. However, if an AUT (perhaps unsuspectingly) actually has high backlobe radiation that is ignored (because it is not expected) the error in the measured AUT gain can be high (and the gain actually significantly lower than measured).

[101] The patterns are similar in the E-plane, and the reason we are doing this calculation is only to seek information on the difference in directivity with and without the backlobes.

directivity as outlined in Appendix F. The result is shown as Item #2 in Table 6.4-1. If we use this directivity, and the measured gain, we can obtain rough estimates of the radiation efficiency as 80% and 87% in the lower and upper frequency bands, respectively. Shape-synthesized elements are apparently not more lossy than conventional elements.

If the same approximate directivity calculation (using the measured pattern data) is repeated with the pattern values in the back hemisphere (with its large backlobe) set to zero, the estimated directivities for Item#2 increase by almost 3dB in each case.

The gain measured (Item#1), and that computed using the 3D full-wave model (Item#3), are within 0.3 dB of each other. This is extra reassurance as to the consistency of the arguments we have used here in Section 6.4 to establish reasons for the differences between the expected and observed performance of the test transmitarray. It might appear unusual that the gains computed using the 3D full-wave model are slightly lower than the measured gains. However, it should be remembered that the uncertainty in the measured gain is at best ± 0.5dB.

Next, the directivity using the approximate pattern analysis with the originally intended transmission coefficients from the theoretical design in Section 6.2, that gave the computed patterns in Fig.6.4-2 and Fig.6.4-3, are listed as Item#4. Although imprecise, we estimate the potential aperture efficiency as follows : We assume that, had the backlobes not been present, the measured realized gain would be the actual values in Item#1 with 3dB added. Since over the 18 – 24 GHz range the input reflection coefficient measured at the feed port is on the order of -12 dB, the mismatch factor can be as much as 0.5 dB. We add this 0.5dB, plus the 3dB referred to in the previous sentence, to obtain the adjusted measured gain (as opposed to realized gain) values in Item#5. We use the data in Item#4 and Item#5 to roughly estimate the aperture efficiencies to be better than 30% and 47% at the lower and upper frequencies, respectively. We say ‘better than’ because the incorrect transmission phases did not only cause the backlobe due to lower transmission magntiudes for some elements, but also incorrect transmission phases. We conclude that the sort of aperture efficiencies obtainable from transmitarrays that use shape-synthesized elements are of the same order as those often reported by others that use conventional elements in some cases.

Table 6.4-1 : Various Measured and Computed Gain/Directivity Values.

Item	Quantity	Value (Frequency)	Value (Frequency)
1	Measured Realized Gain (From Fig.6.4-1)	20.95 dBi (17.4 GHz)	23.9 dBi (23.2 GHz)
2	Directivity Computed from Measured H-Plane Pattern (Assuming Rotationally Symmetric Patterns)	22.1 dBi (17.4 GHz)	24.5 dBi (23.2 GHz)
3	Computed Gain (3D HFSS Full-Wave Analysis)	20.8 dBi (17.4 GHz)	23.6 dBi (23.2 GHz)
4	Computed Directivity (Approximate Analysis) Using the Intended Transmission Coefficients	29.63 dBi (18 GHz)	30.68 dBi (24 GHz)
5	Adjusted Measured Gain = Measured Realized Gain + Mismatch Loss (0.5dB) + 3dB (Accounting for High Backlobe)	23.95 dBi (17.4 GHz)	26.9 dBi (23.2 GHz)

6.5 CONCLUDING REMARKS

This chapter began with the intention of experimentally demonstrating that the shape synthesized elements provide the promised performance. In order to do this a specific dual-band transmitarray was designed[102], fabricated and measured solely for the purpose of serving as a tesbed. Different focal lengths were purposefully selected to instill some independence between the transmission phase sets at the two frequencies. The details of the experimental transmitarray were provided in Section 6.3.

The measured gain was observed, in Section 6.4.1, to be lower than expected. In Section 6.4.2 the measured radiation patterns revealed that one reason for this was the unexpectedly high backlobes, which were accompanied by near-in sidelobes that were also higher than expected from the approximate pattern analysis. In order to establish whether the cause was fabrication-related, a 3D full-wave model of the complete transmitarray antenna was used to compute the gain and patterns. This, along with various patterns of the feed measured in the mounting frame with the transmitarray absent, confirmed that the fabricated transmitarray structure (i.e. the detailed element geometries), as laid out, was in fact performing as expected from the 3D full-wave analysis. The fabrication and assembly was not to blame for the poor performance. Additional investigations of the computations used in the shape synthesis process identified an incorrect interpretation of the reference planes used by the CEM engine in the full-wave analysis of each layer of the 3-layer elements as the problem

---

[102] As summarised in Section 6.2.

issue. This caused the transmission coefficients predicted during shaping to be in error. When the mixed full-wave/equivalent-circuit model for the 3-layer elements is repaired, and the correct transmission coefficients for the realized elements re-computed, the disappointing behaviour becomes the expected one. This allowed the conclusion to be reached that the shape synthesis procedure itself is not in error. In other words, we can conclude that we indeed have a sound shape synthesis procedure for 3-layer transmitarray elements that has not yet been reported by others.

CHAPTER 7
General Conclusions

The principal original contributions to the overall subject of transmitarray element shape synthesis that have been presented in this thesis are as follows :

- Transmitarray elements have been shape synthesized for the first time. In particular, the shape-synthesis of multi-layer elements is now possible.
- As a result, one is now able to obtain transmitarray element sets that can operate at two widely-spaced frequencies, with sets of imposed transmission phase pairs specified at the two frequencies. It is no longer necessary to use prescribed shapes and then try to do as well as one can by adjusting their feature dimensions to get the best transmission phase compromise at the two operating frequencies.
- Even for single-band applications, it is now possible (using 3-layer elements) to obtain a complete 360° transmission phase range, with high transmission amplitudes, from elements that are symmetrical in a way that they respond the same way to two orthogonal linear polarizations, and hence also to circular polarization. This was not previously possible.
- The validity of the shaping ideas has been demonstrated experimentally.
- Although the development of the transmitarray element shaping tool was in essence a means to an end, it represents a contribution of value. The shaping controller has been developed in MATLAB, and the optimization algorithm and full-wave computational electromagnetics modeller software are available commercially. Thus the tool need not gather dust somewhere, but could be accessible to others.

Preliminary portions of the work have been presented in two conference papers :

A.Aljanah and D.A.McNamara, "The shape synthesis of unit elements for transmitarray antennas", *IEEE AP-S Int. Symp. Digest*, San Diego, USA, July 2017.

A.Aljanah and D.A.McNamara, "Shape synthesis of 3-layer transmitarray elements", *IEEE Int. Antennas & Propagat. Symp. Digest*, Boston, USA, July 2018.

There remain some issues/cases whose investigation in the future would prove useful:

- In an attempt to place the transmitarray element shape synthesis research of this thesis in the context of antenna shape synthesis generally we, at the end of Section 2.7, listed five scenarios where such element synthesis might be beneficial. These could immediately be included here as future work that would exercise the abilities of the shaping controller developed. In addition, the potential of using different spacer thickness in permitting the shape synthesis of transmitarray elements with unusual requirements would be useful[103].

- The shape synthesis process is sufficiently flexible that it should now be possible to shape synthesize sets of elements that, when used in a transmitarray, can be used to simultaneously perform lensing and conversion from linear-to-circular polarization. This would simply require new objective functions to be defined.

- Indeed, the shaping controller could be used to shape synthesize the elements (now all identical) for multi-layer circular polarizers, polarization rotators and frequency-selective surfaces (FSS)[104]. As suggested in Section 3.6.2, these could use a filling factor of 100%.

- A really broadband transmitarray (or indeed reflectarray[105]) element would not be one that keeps its transmission phase constant with respect to frequency. The reason is that the incident feed field phase on the input side of each element will change with frequency, and thus the element transmission phases (or reflection phases in the reflectarray case) would also need to change with frequency to compensate for this. It should be possible to shape synthesize elements with a specified frequency dependence by incorporating several frequency points in the objective function.

Many may think that the shape synthesis approach is too computer-time-consuming to be of wide interest. However, such work should always be forward-looking, which in this case means that within a few years the computational resources available could make the developed technique mainstream. We could use it to craft the performance we want of our elements.

---

[103] Although the use of expression (4.2-2) would to be possible, it could straightforwardly be replaced by an optimization sub-problem involving the full T-circuits (and hence fewer than 6 variables) that could use a gradient algorithm that is extremely rapid and uses rough results from (4.2-1) as a "warm start".

[104] As noted in Section 2.7, FSS devices have been shape synthesized by at least two other authors, but only single-layer ones. As far as we are aware, polarizers have not yet been shape-synthesized.

[105] To which the shaping controller could be applied with a change in the objective function.

REFERENCES

[ABDE 14] A. H. Abdelrahman, A. Z. Elsherbeni, and F. Yang, “High-gain and broadband transmitarray antenna using triple-layer spiral dipole elements”, *IEEE Antennas and Wireless Propagation Letters*, vol. 13, pp. 1288-1291, July 2014.

[ABDE 15] A. H. Abdelrahman, P. Nayeri, A. Z. Elsherbeni, and F. Yang, “Bandwidth improvement methods of transmitarray,” *IEEE Transactions on Antennas and Propagation*, vol. 63, no. 7, pp. 2946–2854, April 2015.

[ABDE 17] A. H. Abdelrahman, F. Yang, A. Z. Elsherbeni, and P. Nayeri, *Analysis and Design of Transmitarray Antennas* (Morgan & Claypool Publ., 2017).

[ALAK 17] A.Alakhras and D.A.McNamara, “The shape optimisation of closely-spaced electrically-small antennas”, *IEEE AP-S Int. Symp. Digest*, San Diego, USA, July 2017.

[ALAK 18] A.Alakhras and D.A.McNamara, “Further observations on the shape synthesis of closely-spaced antennas using sub-structure characteristic modes”, *IEEE Int. Antennas & Propagat. Symp. Digest*, Boston, USA, July 2018.

[ALMA 11] E. Almajali, D. A. McNamara, J. Shaker, M. R. Chaharmir, “Observations on the performance of reflectarrays with reduced inter-element spacings”, IEEE AP-S Int. Symp. Digest, pp.369-372, USA, July 2011.

[ALMA 14] E. Almajali, D. A. McNamara, N. Gagnon, and A. Petosa, “Remarks on the feasibility of full-wave analyses of printed lens/transmitarray antennas”, *IEEE Antennas and Propagation International Symposium*, Memphis, USA, pp. 1268-1269, 6-11 July 2014.

[ALRO 20] H.Alroughani and D.A.McNamara, “The shape synthesis of dielectric resonator antennas”, Accepted for publication in the *IEEE Trans. Antennas Propagation,* 2020.

[ALTS 02] E. Altshuler, "Electrically small self-resonant wire antennas optimized using a genetic algorithm," *IEEE Transactions on Antennas and Propagation*, vol. 50, no. 3, pp. 297-300, 2002.

[AN 14] W.An, S.Xu, and F. Yang, “A two-layer transmitarray antenna”, *IEEE Antennas and Propagation International Symposium)*, Memphis, USA, pp. 864-865, 6-11 July 2014.

[AOKI 11] Y. Aoki, H. Deguchi, and M. Tsuji, “Reflectarray with arbitrarily-shaped conductive elements optimized by genetic algorithm”, *IEEE Antennas and Propagation International Symposium*, Spokane, Washington, USA, July 2011.

[BALA 05] C. A. Balanis, *Antenna Theory* (Wiley, 2005).

[BALA 08] C. A. Balanis, *Modern Antenna Handbook* (Wiley, 2008).

[BAGH 17] M.O.Bagheri, H.R.Hassani and B.Rahmati, “Dual-band, dual-polarised metallic slot transmitarray antenna”, IET Micriowaves, Antennas & Propagation, Vol.11, No.3, pp.402-409, 2017.

[BAND 69] J.W.Bandler, “Optimization methods for computer-aided design”, *IEEE Transactions Microwave Theory and Techniques, vol.17, no.8, August 1969.*

[BAND 88] J. W. Bandler, and S. H. Chen, “Circuit optimization: the state of the art”, *IEEE Transactions on Microwave Theory and Techniques,* vol. 36, no. 2, pp. 424-443, February 1988.

[BHAT 06] A.K.Bhattacharyya, *Phased Array Antennas* (Wiley, 2006).

[BOCC 11] L. Boccia, I. Russo, G. Amendola, and G. Di Massa, “Preliminary results on tunable frequency selective surface for beam-steering transmitarray applications”, *Proceedings of the 5th European Conference on Antennas and Propagation (EuCAP 2011),* Rome, Italy, pp.1002-1005, 11-15 April 2011.

[CAMP 98] M.A.Campo, F.J. del Rey, J.L.Besada and L. de Haro, “SABOR : Description of the methods applied for a fast analysis of horn and reflector antennas”, IEEE Antennas Propagat. Magazine, vol.40, no.4, pp.95-108, Aug.1998.

[CHOO 05] H. Choo and H. Ling, "Design of electrically small wire antennas using a Pareto genetic algorithm," *IEEE Transactions on Antennas and Propagation,* vol. 53, no. 3, pp. 1038-1046, 2005.

[CRUZ 18] C. C. Cruz, C. A. Fernandes, S. A. Matos, and J. R. Costa, “Synthesis of shaped-beam radiation patterns at millimeter-waves using transmitarrays”, *IEEE Transactions on Antennas and Propagation*, vol. 66, no. 8, pp. 4017-4024, August 2018.

[DUSS 18] L. Dussopt, “Transmitarray antennas”, Chapter 6 in: A. Boriskin and R. Souleau (Edits.), *Aperture Antennas for Millimeter and Sub-Millimeter Wave Applications* (Springer, 2018).

[EBRA 14] A. Ebrahimi, W. Withayachumnankul, S. Al-Sarawi, and D. Abbott, “Design of dual-band frequency selective surface dual-band unit cells designs with miniaturized elements”, *IEEE Proceedings International Workshop on Antenna Technology (iWAT),* Sydney, NSW, Australia, pp.206-209, March 2014.

[ERFA 19] E. Erfani, S. Safavi-Naeini and S. Tatu, “Design and analysis of a millimetre-wave high gain antenna”, IET Micriowaves, Antennas & Propagation, Vol.13, No.10, pp.1586-1592, August 2019.

[EREN 11] Erentok and O. Sigmund, "Topology optimization of sub-wavelength antennas," *IEEE Transactions on Antennas and Propagation*, vol. 59, no. 1, pp. 58-69, 2011.

[ETHI 12] J. Ethier and D. McNamara, "A sub-structure characteristic mode concept for antenna shape synthesis," *Electronics Letters*, vol.48, no.9, 2012.

[ETHI 14a] J. Ethier and D. McNamara, "Antenna shape synthesis without prior specification of the feedpoint locations," *IEEE Transactions Antennas Propagation*, vol.62, no.10, pp.4919-4934, 2014.

[ETHI 14b] J. Ethier, D. A. McNamara, J. Shaker, and R. Chaharmir, "Reflectarray synthesis with similarity-shaped fragmented sub-wavelength elements", *IEEE Transactions on Antennas and Propagation*, vol. 62, no. 9, pp. 4498-4509, September 2014.

[FEKO] *FEKO*, Altair Inc. (www.altair.com).

[GAGN 13] N.Gagnon, A.Petosa & D.A.McNamara, "Research and Development on Phase Shifting Surfaces (PSSs)", *IEEE Antennas & Propagation Magazine*, Vol.55, No.2, pp.29-48, April 2013.

[GOSA 14] G. Gosal, D. A. McNamara, and M. C. E. Yagoub, "The use of inverse neural networks in transmitarray antenna design", *IEEE Antennas and Propagation International Symposium*, Memphis, USA, pp.1272-1273, July 2014.

[GOUD 17] S. Goudos, "Antenna design using binary differential evolution," *IEEE Antennas and Propagation Magazine*, pp.74-93, Feb.2017.

[GRIF 06] L. Griffiths and C. Chung, "Broadband and multiband antenna design using the genetic algorithm to create amorphous shapes using ellipses", *IEEE Transactions Antennas and Propagation*, Vol.54, No.10, pp.2776 – 2782, 2006.

[HASS 14] E. Hassan and M. Bergren,"Topology optimization of metallic antennas", *IEEE Transactions on Antennas and Propagation*, vol.62, no.5, pp.2488-2500, May 2014.

[HFSS] HFSS, www.ansys.com

[HSU 18] C-H. Hsu, L-T. Hwang, T-S. Horng, S-H. Wang, F-S. Chang, and C. N. Dorny, "Transmitarray design with enhanced aperture efficiency using small frequency selective surface cells and discrete Jones matrix analysis", *IEEE Transactions on Antennas and Propagation*, vol. 66, no. 8, pp. 3983-3994, August 2018.

[HUAN 07] J. Huang, *Reflectarray Antennas*, Chapter 35 in: J. L. Volakis (Edit.), *Antenna Engineering Handbook* (Wiley, 2007).

[HUAN 08] J. Huang and J. A. Encinar, *Reflectarray Antennas* (Wiley, 2008).

[JAKO 00] U. Jakobus, “Comparison of different techniques for the treatment of lossy dielectric/magnetic bodies within the method of moments formulation”, AEÜ Int. J. Electron. Commun., Vol.54, No.1, 2000.

[JAZI 16] M. N. Jazi, M. R. Chaharmir, J. Shaker, and A. R. Sebak, “Broadband transmitarray antenna design using polarization-insensitive frequency selective surfaces”, *IEEE Transactions on Antennas and Propagation*, vol. 64, no. 1, pp. 99-108, January 2016.

[JOHN 90] W. A. Johnson, D. R. Wilton, and R. M. Sharpe, “Modeling scattering from and radiation by arbitrarily shaped objects with the electric field integral equation”, *Electromagnetics Journal*, vol. 10, no. 1-2, pp. 41-63, 1990.

[JOHN 99a] J. M. Johnson and Y. Rahmat-Samii, “Genetic algorithms and method of moments (GA/MOM) for the design of integrated antennas”, *IEEE Transactions on Antennas and Propagation*, vol. 47, no. 10, pp. 1606-1614, October 1999.

[JOHN 99b] J. M. Johnson and Y. Rahmat-Samii, “Evolutionary designs of integrated antennas using genetic algorithms and method of moments (GA/MOM)”, Chapter 9 in: Y. Rahmat-Samii and E. Michielssen (Edits.), *Electromagnetic Optimization by Genetic Algorithms* (Wiley, 1999).

[JOYA 12] M. Joyal and J. Laurin, “Analysis and design of thin circular polarizers based on meander lines”, *IEEE Transactions on Antennas and Propagation*, vol. 60, no. 6, pp. 3007-3011, June 2012.

[KRIS 16] G. Kristensson, *Scattering of Electromagnetic Waves by Obstacles* (SciTech Publ., 2016).

[LEVI 89] E. Levine, G. Malamud, S. Shtrikman, and D. Treves, “A study of microstrip array antennas with the feed network”, *IEEE Transactions on Antennas and Propagation*, vol. 37, no. 4, pp. 426-433, 1989.

[LIU 15] G.Liu, H.Wang, J.Jiang, F.Xue and M.Yi, “A high-efficiency transmitarray antenna using double split ring slot elements”, *IEEE Antennas and Wireless Propagation Letters*, vol.14, pp.1415-1418, 2015.

[LIND 99] D.Linden and E.Altshuler, "Design of wire antennas using genetic algorithms", Chapter 8 in : Y. Rahmat-Samii and E. Michielssen (Edits.), *Electromagnetic Optimization by Genetic Algorithms* (Wiley, 1999).

[LORE 18] S.Loredo, G.Leon, O.F.Robledo and E.G.Plaza, “Phase-only algorithm for transmitarrays and dielectric lenses”, *ACES Journal*, Vol.33, No.3, pp.259-264, March 2018.

[LUO 14] J. Luo, F. Yang and S. Xu, “E-shaped element design for linearly polarized transmitarray antennas”, *IEEE Antennas and Propagation International Symposium (ISAP 2014)*, Taiwan, pp. 269-270, 2-5 December 2014.

[MAIL 17] R. J. Mailloux, *Phased Array Antenna Handbook* (Artech House, 2017)

[MATLAB] MATLAB, Mathworks Inc. (www.mathworks.com)

[MATO 17] S. A. Matos, E. B. Lima, J. S. Silva, J. R. Costa, C. A. Fernandes, N. J. G. Fonseca, and J. R. Mosig, “High gain dual-band beam-steering transmitarray for SATCOM terminals at Ka-band”, *IEEE Transactions on Antennas and Propagation*, vol. 65, no. 7, pp. 3528-3539, July 2017.

[MIRH 15] S.Mirhadi and M.Soleimani, "Ultra wideband antenna design using discrete Green's functions in conjunction with binary particle swarm optimisation," *IET Microwaves, Antennas & Propagation,* vol. 10, no.2, pp.184-192, 2016.

[MOLE 18] S.Molesky, Z.Lin, A.Y.Piggott, W.Jin, J.Vuckovic and A.W.Rodriguez, “Inverse design in nanophotonics”, *Nature Photonics*, Vol.12, pp.659-670, Nov.2018.

[NEMA15] H. Nematollahi, J. J. Laurin, J. E. Page, and J. A. Encinar, “Design of broadband transmitarray unit cells with comparative study of different numbers of layers”, *IEEE Transactions on Antennas and Propagation*, vol. 63, no. 4, pp. 1473-1481, April 2015.

[NEMA17] H. Nematollahi, J. J. Laurin, m.Barba and J. A. Encinar, “Realization of focused beam and shaped beam based on broadband unit cells”, *IEEE Transactions on Antennas and Propagation*, vol.65, no.8, pp. 4368-4373, August 2017.

[OHIR 04] M. Ohira, H. Deguchi, M. Tsuji, and H. Shigesawa, “Multiband single-layer frequency selective surface designed by combination of genetic algorithm and geometry-refinement technique,” *IEEE Transactions on Antennas and Propagation*, vol. 52, no. 11, pp. 2925-2931, November 2004.

[PARI 14] C.Parini, S.Gregson, J.McCormick & D.J.Janse van Rensburg, *Principles, Theory and Practice of Modern Antenna Range Measurements* (IET Electromagnetic Wave Series, 2014)

[PETE 97] A. Peterson, S. Ray, and R. Mittra, *Computational Methods for Electromagnetics* (IEEE Press, 1997).

[POZA12] D. M. Pozar, *Microwave Engineering* (Wiley, 2012).

[RAHM 07] Y. Rahmat-Samii, *Reflector Antennas,* Chapter 15 in: J. L. Volakis (Edit.), *Antenna Engineering Handbook* (McGraw-Hill, 2007), 4th Edition.

[RAHM 12] Y. Rahmat-Samii and H. Rajagopalan, "Nature-inspired optimization techniques in communication antenna designs," *Proceedings of the IEEE*, vol. 100, no. 7, pp. 2132-2144, 2012.

[RAHM 15] B. Rahmati and H. R. Hassani, “Low-profile slot transmitarray antenna”, *IEEE Transactions on Antennas and Propagation*, vol. 63, no. 1, pp. 174-181, January 2015.

[RAO 13] S. Rao, L. Shafai, and S. K. Sharma (Edits.), *Handbook of Reflector Antennas and Feed Systems*, Vol. I, II, and III (Artech House, 2013).

[ROTZ 14] G.I.N.Rozvany and T.Lewinski (Edits.), *Topology Optimization in Structural and Continuum Mechanics* (Springer, 2014).

[RYAN 10] C. G. M. Ryan, M. R. Chaharmir, J. Shaker, J. R. Bray, Y. M. M. Antar, and A. Ittipiboon, “A wideband transmitarray using dual-resonant double square rings”, *IEEE Transactions on Antennas and Propagation*, vol. 58, no. 5, pp. 1486-1493, May 2010.

[SALU 18] M. Salucci, F.Robol, N.Anselmi, M.A.Hannan, P.Rocca, G.Olivieri, M.Donelli and A.Massa, "S-Band spline-shaped aperture-stacked patch antenna for air traffic control applications," *IEEE Transactions on Antennas and Propagation*, vol. 66, no. 8, pp. 4292-4297, 2018.

[SAZO 82] D. M. Sazanov, A. N. Gridin, and B. A. Mishustin, *Microwave Circuits* (Mir Publ., 1982), pp.74-75.

[SCHE 52] S. A. Schelkunoff, *Antennas : Theory and Practice* (Wiley, 1952), p.537.

[SHAK 13] J. Shaker, M .R. Chaharmir, and J. Ethier, *Reflectarray Antennas: Analysis, Design, Fabrication, and Measurement* (Artech House, 2013).

[SHAL 95] A. D. Shatrow, A. D. Chuprin, and A. N. Sivov, “Constructing the phase converters consisting of arbitrary number of translucent surfaces”, *IEEE Transactions on Antennas and Propagation*, vol.43, no.1, pp.109–113, Jan.1995.

[STUT 08] W.Stutzman and S.Licul, “Synthesis Methods for Antennas” in C.A.Balanis (Edit.), *Modern Antenna Handbook* (Wiley, 2008) pp.631.

[STUT 13] W. L. Stutzman and G. A. Thiele, *Antenna Theory and Design*, (Wiley, 2013).

[THOR 05] B.Thors and H.Holter, "Broadband fragmented aperture phased array element design using genetic algorithms", *IEEE Transactions Antennas propagate* vol. 53, pp. 3280-3287, 2005.

[TIAN 17] C. Tian, Y-C. Jiao, and G. Zhao, “Circularly polarized transmitarray antenna using low-profile dual-linearly polarized elements”, *IEEE Antennas and Wireless Propagation Letters*, vol. 16, pp. 465–468, July 2017.

[TOIV 10] J. Toivanen, R. Mäkinen, J.Rahola, S.Järvenpää and P.Ylä-Oijala, “Gradient-based shape optimization of ultra-wideband antennas parameterized using splines,” *IET Microwaves, Antennas & Propagation*, vol. 4, pp. 1406-1414, 2010.

[TULO 19] S.H. S.H.R.Tuloti, P.Rezaei and F.T.Hamedani, “Unit cell with flexible transmission phase slope for ultra-wideband transmitarray antennas”, IET Microwaves, Antennas & Propagation, Vol.13, No.10, pp.1522-1528, Aug.2019

[VOLA 07] J. L. Volakis (Edit.), *Antenna Engineering Handbook* (McGraw-Hill, 2007).

[VOLA 12] J. L. Volakis and K. Sertel, *Integral Equation Methods for Electromagnetics* (SciTech Publ., 2012).

[WU 17] R. Y. Wu, Y. B. Li, W. Wei, C. B. Shi, and T. J. Cui, “High-gain dual-band transmitarray”, *IEEE Transactions on Antennas and Propagation*, Vol.65, No.7, pp.3481-3488, May 2017.

[YAMA 09] T. Yamamoto and T. Tsukagoshi, "Efficient antenna miniaturization technique by cut off of chromosome-length in genetic algorithm," *Asia Pacific Microwave Conference*, Singapore, pp. 1837-1840, 2009.

[YANG 19] B. Yang and J. Adams, "A shape-first, feed-next design approach for compact planar MIMO antennas," *Progress In Electromagnetics Research*, Vol. 77, 157–165, 2019.

[YU 16] J. Yu, L. Chen, J. Yang, and X. Shi, “Design of transmitarray using split diagonal cross elements with limited phase range”, *IEEE Antennas and Wireless Propagation Letters*, vol. 15, pp. 1514–1517, July 2016.

[ZAIN 13] S. H. Zainud-Deen, S. M. Gaber, H. A. Malhat, and K. H. Awadalla, “Single feed dual-polarization dual-band transmitarray for satellite applications”, *30th National Radio Science Conference (NRSC 2013)*, Cairo, Egypt, April 2013.

[ZAIN 14] S. H. Zainud-Deen, S. M. Gaber, H. A. Malhat, and K. H. Awadalla, “Single feed dual-polarization dual band transmitarray for satellite applications”, *AECS Journal*, vol. 29, no. 2, pp. 149-156, February 2014.

APPENDIX A: Genetic Algorithm in the MATLAB Optimization Toolbox

The genetic algorithm optimization function is a built-in function in the MATLAB optimization toolbox. It allows the user to adjust the algorithm parameters so as to fine-tune the GA to a particular application. The parameter options are shown in Table A-1 below, so that they can be referred to in the text if needed.

Table A-1 : Parameter options available for MATLAB genetic algorithm software.

Option Name	Value/Type	Description/ Note
Population Type	Bit String	Every bit in the chromosome signifies a block in the structure: 1 signifies block presence and 0 absence.
Population Size	100	The number of individuals.
Initial Population	Specified	Initial geometry from a previous optimization run was used in the final optimization.
Scaling Function	Proportional	"The scaling function converts raw fitness scores returned by the fitness function to values in a range that is suitable for the selection function. Proportional makes the expectation proportional to the raw fitness score".
Selection Factor	Tournament	"Selects each parent by choosing individuals at random" the default number (4) was selected.
Reproduction	Elite count	Five elite individual with best fitness scores survive to the next generation.
Mutation function	Uniform	"Mutation functions make small random changes in the individuals in the population, which provide genetic diversity and enable the genetic algorithm to search a broader space.". Uniform was selected since it does not make a difference since 0 and 1 are used here
Mutation Rate	0.01	The default value was used.
Crossover	Scattered	This combines two parents to produce a new individual for the subsequent generation. A random binary is created. If the random vector has "1" then it take a gene from the first parent and if "0" it takes it from the second parent.
Migration	Both	Both is the migration of the nth subpopulation migrates into both the (n–1)th and the (n+1)th subpopulation. This intends to move individual between subpopulations.
Migration Fraction	0.2	The default value was used.
Generation	10	Number of specified generations.
Stall Generation	2	"If the average change in the fitness function value over Stall generations is less than Function tolerance, the algorithm stops".
Function Tolerance	10^{-6}	The default value was used.

APPENDIX B : Pyramidal Feed Horn Details

Table B-1 : Feed horn dimensions

Quantity	Value
a	10.7 mm
b	4.3 mm
L	30.80 mm
W	33.74 mm
H	24.30 mm
Phase Centre δ at 18 GHz	7.57 mm
Phase Centre δ at 24 GHz	14.5 mm

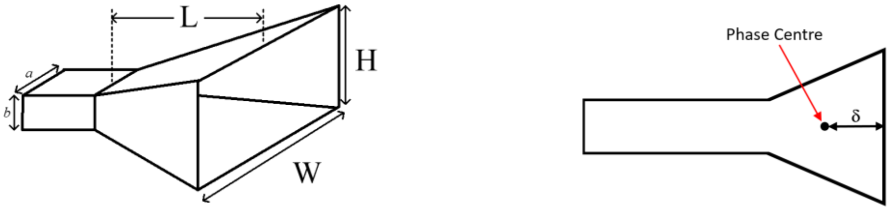

Fig.B-1 : Feed horn geometry

The locations of the feed phase centre at the lower (18 GHz) and upper (24 GHz) frequencies were estimated using the method described in [CAMP 98]; the average value of that computed for the E-, H- and D-planes of the feed is used as suggested in that reference.

APPENDIX C : Rohacell Material Properties

Data on the spacer material ROHACELL® HF is shown in Table C-1. It was accessed from www.rohacell.com in 2019.

Table C-1 : Electromagnetic Properties of Spacer Foam[106]

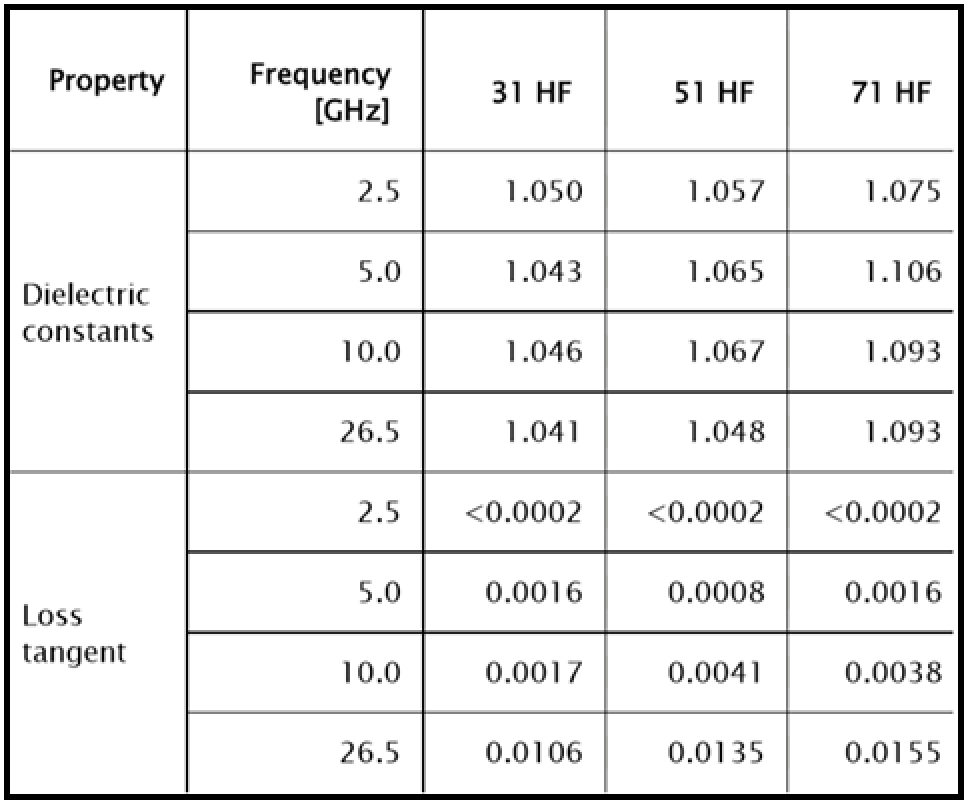

Property	Frequency [GHz]	31 HF	51 HF	71 HF
Dielectric constants	2.5	1.050	1.057	1.075
	5.0	1.043	1.065	1.106
	10.0	1.046	1.067	1.093
	26.5	1.041	1.048	1.093
Loss tangent	2.5	<0.0002	<0.0002	<0.0002
	5.0	0.0016	0.0008	0.0016
	10.0	0.0017	0.0041	0.0038
	26.5	0.0106	0.0135	0.0155

---

[106] Extracted from www.rohacell.com in 2019.

APPENDIX D : Printed Layers of the Fabricated Transmitarray

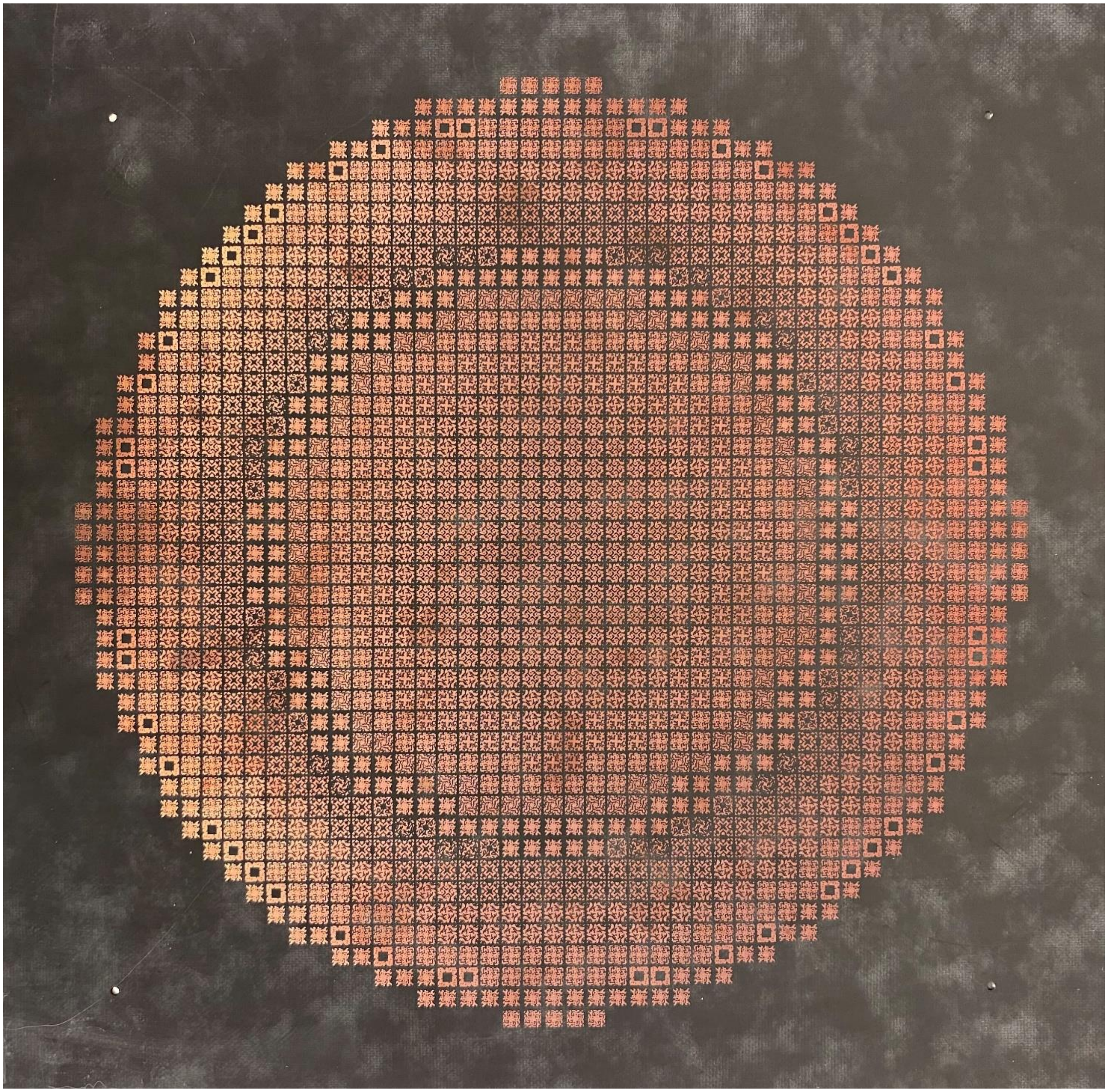

Fig.D-1 : Printed front layer of the fabricated 3-layer dual-band transmitarray.

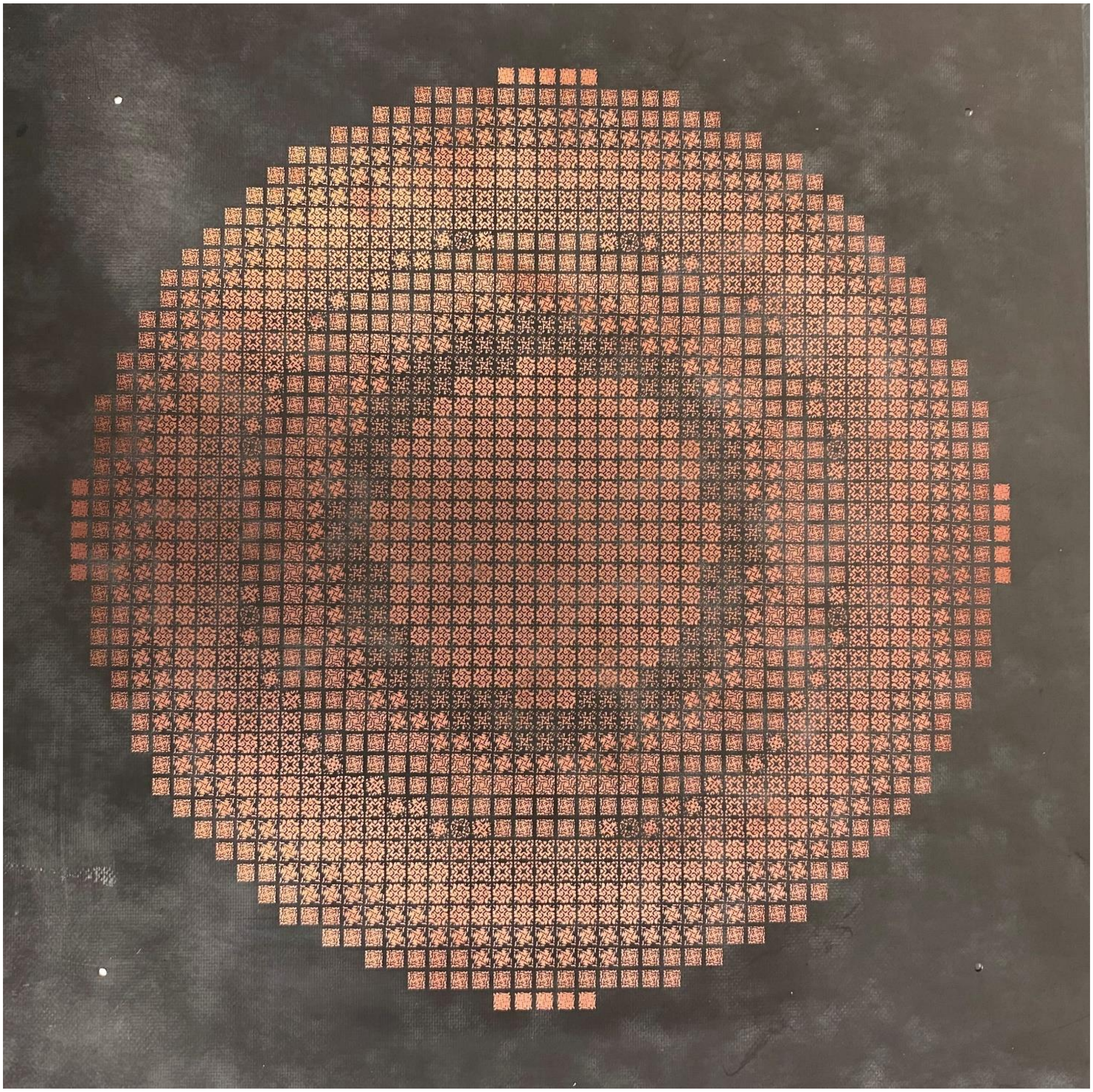

Fig.D-2 : Printed middle layer of the fabricated 3-layer dual-band transmitarray.

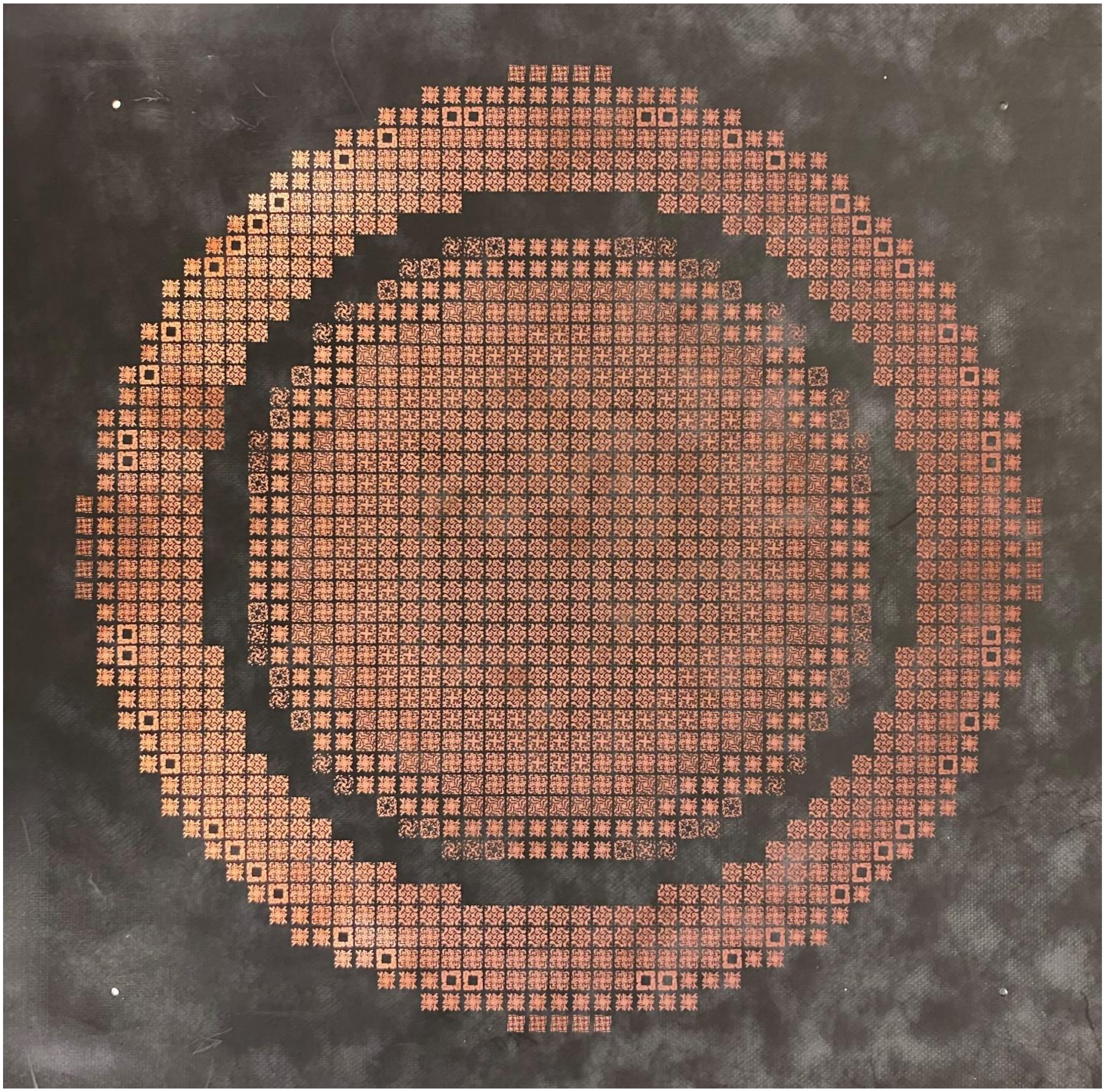

Fig.D-3 : Printed back layer of the fabricated 3-layer dual-band transmitarray.

APPENDIX E : Technical Aspects of *HFSS* Full-Wave 3D Model of Complete Transmitarray of 3-Layer Elements

The complete geometry file (much the same as that used for the fabrication of the 3-layer transmitarray in Chapter 6) was transferred to HFSS and a model of a single quadrant of the transmitarray set up, and indicated in Fig.E-1. The complete transmitarray is formed from four such quadrants, but due to symmetry, unique unknowns are needed for a single quadrant only through use of appropriate symmetry boundaries. The pyramidal feed horn is also modelled in HFSS, as shown in Fig.E-2. The transmitarray and feed horn are each placed in separate radiation boxes, which are then appropriately linked. There were 4.83 million unique tetrahedra used in the transmitarray radiation box, had not quadrantal symmetry been possible this would have been four times this number

.

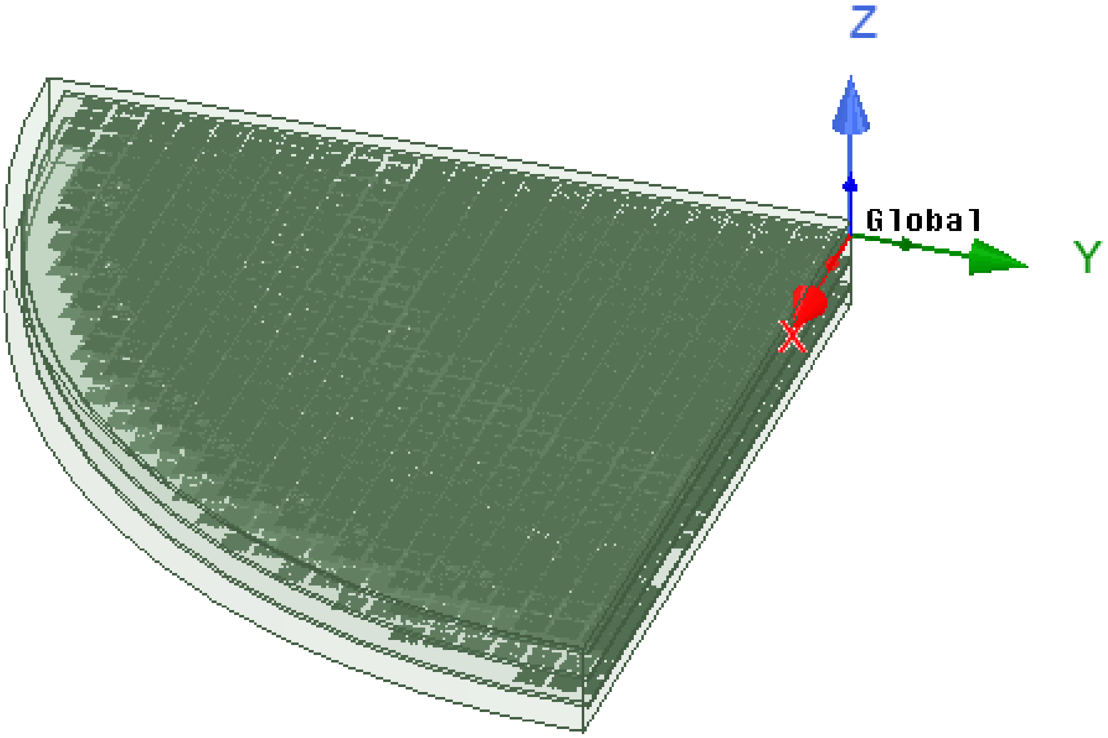

Fig.E-1 : One quadrant of the HFSS three-dimensional model of the complete transmitarray of 3-layer elements.

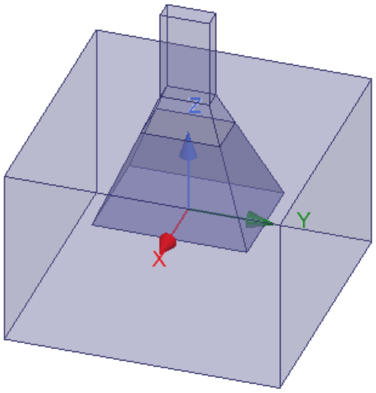

Fig.E-2 : HFSS three-dimensional model of the pyramidal feed horn.

APPENDIX F : Directivity Estimation Used in Section 6.4.6

If we have an antenna whose radiation intensity $U(\theta) = (1/2\eta_o)\left|E_{\text{co}}(\theta)\right|^2$ is independent of ϕ, we can use it to find the directivity as

$$D(\theta) = \frac{4\pi U(\theta)}{\int_0^{\pi}\int_{-\pi}^{\pi} U(\theta)\sin\theta d\theta d\phi} = \frac{4\left|E_{\text{co}}(\theta)\right|^2}{\int_{-\pi}^{\pi}\left|E_{\text{co}}(\theta)\right|^2 \sin\theta d\theta d\phi} \tag{F-1}$$

The integral in the denominator is easily evaluated numerically.

$$D(0^\circ) = \frac{4\left|E_{\text{co}}(0^\circ)\right|^2}{\int_{-\pi}^{\pi}\left|E_{\text{co}}(\theta)\right|^2 \sin\theta d\theta d\phi} \tag{F-2}$$